IVANE JAVAKHISHVILI TBILISI STATE UNIVERSITY

ILIA VEKUA INSTITUTE OF APPLIED MATHEMATICS

GEORGIAN ACADEMY OF NATURAL SCIENCES

TBILISI INTERNATIONAL CENTRE OF

MATHEMATICS AND INFORMATICS

L E C T U R E   N O T E S

of

T I C M I

Volume 16, 2015

W.H. Müller, E.N. Vilchevskaya, & A.B. Freidin

STRUCTURAL CHANGES IN MICRO-MATERIALS: PHENOMENOLOGY, THEORY, APPLICATIONS, AND SIMULATIONS

Tbilisi

LECTURE NOTES OF TICMI

Lecture Notes of TICMI publishes peer-reviewed texts of courses given at Advanced Courses and Workshops organized by TICMI (Tbilisi International Center of Mathematics and Informatics). The advanced courses cover the entire field of mathematics (especially of its applications to mechanics and natural sciences) and from informatics which are of interest to postgraduate and PhD students and young scientists.

Editor: G. Jaiani
        I. Vekua Institute of Applied Mathematics
        Tbilisi State University
        2, University St., Tbilisi 0186, Georgia
        Tel.: (+995 32) 218 90 98
        e.mail: george.jaiani@viam.sci.tsu.ge

Contents

Abstract. This paper is concerned with the description of the physics and the corresponding mathematical modeling of three related phenomena. They occur on the (sub-) microscale of materials used in today's microelectronic technology and have an impact on the manufacturing process as well as the reliability of the whole electronic structure.

The first example concerns the oxidation process of silicon. The formation of silicon oxide out of silicon is accompanied by mechanical deformation due to a change of volume during the reaction. The developing stresses and strains influence the diffusion kinetics of the process: They can even bring it to a standstill. Material scientists tend to model the mechanical part of the phenomenon by adding an artificial stress dependence to the diffusion and to the reaction constants. In this paper we will pursue a different approach based on a sharp interface model. Starting from first principles an expression for the velocity of the oxidation front will be derived. The front velocity is related to the local Eshelby tensor and contains *a priori* chemical as well as mechanical driving forces.

The second example deals with the aging of eutectic tin-lead solder. This is a two-phase material consisting of regions rich in tin and regions rich in lead because tin and lead mix only very slightly. Initially these regions are finely dispersed giving rise to a filigreed micro-structure, *i.e.*, an electrically and mechanically highly reliable solder joint has been generated. However, due to temperature and the presence of local mechanical stresses a solid → solid diffusion process sets in and the regions start coarsening. The micro-structure deteriorates and the solder joints eventually becomes electrically and mechanically unreliable. A phase-field model will be used to describe the process of spinodal decomposition.

The third and final example addresses the formation and the ripening of intermetallic phases in microelectronic solders or at the interface between the solder and the connecting pad. The formation of such phases is accompanied by a change in volume just like during the formation of silicon dioxide. In other words, this is another example of stress-assisted growth kinetics. However, other than silicon dioxide they show a highly ordered crystalline structure, *i.e.*, they are anisotropic which, in particular, influences their growth behavior. The paper will end with a discussion of potential models that could be used for a quantitative description.

Wolfgang H. Müller[*]
Technische Universität Berlin, Institut für Mechanik, LKM, Einsteinufer 5, 13591 Berlin, Germany

Elena N. Vilchevskaya[a,b] **and Alexander B. Freidin**[a,c]
[a]Institute for Problems in Mechanical Engineering of Russian Academy of Sciences, Bolshoy Pr., 61, V.O., St. Petersburg 199178, Russia
[b]St. Petersburg State Polytechnical University, Polytechnicheskaya Str., 29, St. Petersburg 195251, Russia
[c]St. Petersburg State University, Universitetsky Pr., 28, Peterhof, St. Petersburg 198504, Russia

[*] Corresponding author. Email: wolfgang.h.mueller@tu-berlin.de

1   Microstructural changes in modern electronic materials

The development of modern electronic and mechatronic products is dictated by the continuous quest toward further and further miniaturization. Consequently, the microstructure of the production materials is of paramount importance. Moreover, once a certain beneficial microstructure has been realized it is by no means guaranteed that it will continue to exist the way it was initially created. We face a dynamic situation during which the structure may change and, consequently, reliability issues due to aging of the materials will arise.

All of this is bad news for the manufacturers of products. However, it results in challenging tasks for material scientists, physicists, and mathematicians, all of whose skills are required for a better understanding and for the mathematical description of the underlying chemistry and physics.

In what follows we will focus on three phenomena which, as we shall see, are related in terms of microstructural change and the corresponding mathematical modeling. In each case we will first present the experimental evidence and try to explain the findings verbally. The latter will guide us during the setup of an appropriate mathematical model. We will then spend a considerable amount of time to make these models as quantitative as possible. In other words, it will be our goal to find data for the involved material parameters not by matching the experiments to the model but from independent sources unrelated to the phenomenon in question. Note that there is a fundamental difference between our approach and the commonly adopted materials science point-of-view. The latter is frequently *ad hoc*, in the sense that parameters are "adjusted" so that the model eventually leads to the required outcome. Of course, materials scientists attempt to motivate their adjustment of model parameters. However, their efforts are often heuristic, based exclusively on words and not on first principles in terms of physics combined with adequate mathematical techniques. Moreover, once an adjustment has been brought to perfect coincidence with the experimental findings in one situation it is by no means guaranteed that the same set of parameters can be used for another geometry. This, however, is a measure of the quality of a model in the sense of a true capture of the behavior of nature.

2 Silicon oxidation

2.1 The technical perspective

Following the nomenclature established in [28] we consider a binary reaction of the type:

$$n_- B_- + n_* B_* \rightleftharpoons n_+ B_+ \tag{2.1.1}$$

and apply it to the so-called *dry* oxidation process of silicon, *i.e.*,

$$\mathrm{Si} + \mathrm{O}_2 \rightleftharpoons \mathrm{SiO}_2. \tag{2.1.2}$$
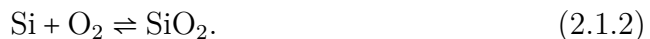
The symbols n_- , n_*, and n_+, which are known under the term *stoichiometric coefficients*, characterize the number of atoms or molecules of the reactants and of the products involved in the reaction. They are pure numbers without a unit, but they do have a sign [40]: Reactants, *i.e.*, the n's on the left hand side of the reaction balance, are counted negatively, whereas the products on the right hand side have positive values. The n's should also not be confused with the so-called *chemical amount* of a substance, which is also frequently used in chemical thermodynamics in context with reaction equations. Following the conventions of chemical engineers these "amounts" have a unit, namely $1\,\mathrm{mol}$ or $1\,\mathrm{kmol}$, depending on whether we count mass in g or in kg.
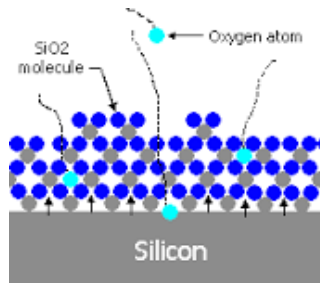
Figure 2.1: A schematic of dry silicon oxidation, see [69] for details.

In the case of dry oxidation of silicon we have $n_- \equiv n_{\mathrm{Si}} = -1$, $n_* \equiv n_{\mathrm{O}_2} = -1$, and $n_+ \equiv n_{\mathrm{SiO}_2} = +1$. Note that we do not write $n_* \equiv n_{\mathrm{O}} = -2$, because this is *not* the elementary reaction taking place at the atomic scale: An oxygen molecule diffuses from the outside to the silicon surface where it links with a silicon atom and forms one silicon dioxide "molecule." Then several such aggregates form an amorphous layer of silicon dioxide or silica which grows continuously: Fig. 2.1. Clearly the diffusion of the outside oxygen molecules to reach the *current* silicon surface will take more time the thicker the amorphous layer becomes. However, rumor has it that the oxygen molecules are not severely impeded by the presence of the growing layer of silicon dioxide and that after a very short time a stationary diffusion flow is established which, timewise, is governed by a simple isotropic diffusion constant. We will get back to this issue

later, where we shall also discuss as to whether the diffusion constant might be *anisotropic*, that it might be affected by mechanical stress and strain, and "how fast" it is in comparison with relaxation processes within the amorphous layer.
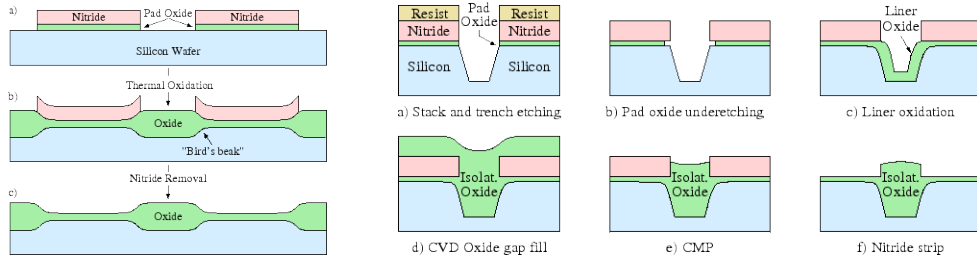
Figure 2.2: Schematics of the LOCOS and STI processes, see [38] for details.

For completeness note that there is an alternative process for creating silica, namely the so-called *wet* oxidation:

$$Si + 2H_2O \rightleftharpoons SiO_2 + H_2. \tag{2.1.3}$$

Clearly this does not fit into the reaction scheme of Eqn. (2.1.1), since two products result. Moreover, two water molecules have to interact with one silicon atom instead of just one oxygen molecule. We will not model wet oxidation in this paper. However, it should be mentioned at this point that either way a relatively high temperature is required for the chemical reactions to take place. Therefore they are also referred to as *thermal oxidation processes*. We will get back to the temperature issue later.

Wet and dry oxidation were initially used in the eighties for *electric isolation* of adjacent structures in microelectronic devices. In order to see that these processes are effective and truly reach this goal we only need to look at the electrical conductivities of SiO_2 and Si, which are $10^{-16}\,\Omega^{-1}cm^{-1}$ compared to $1.56 \times 10^{-3}\,\Omega^{-1}cm^{-1}$ [83], [94].

Presumably the first process of this kind on an industrial scale was LOCOS (LOCal Oxidation of Silicon, *cf.*, [95]). This acronym refers to a microfabrication scheme where silicon dioxide is formed in selected areas on a silicon wafer having the Si-SiO$_2$ interface at a lower point than the rest of the silicon surface (*cf.*, Fig. 2.2). LOCOS is typically performed at temperatures between 800 and 1200 °C. However, it turned out that if the isolation windows became narrower than 0.7 µm oxide growth became progressively inhibited and would result in oxide layers as much as 80 percent thinner than comparable layers grown in wide windows greater than 2 µm. "This is the so-called 'oxide thinning effect'. [. . .] Thinner-than-desired field oxide layers may allow widely different breakdown and isolation characteristics between neighboring devices, and hence seriously degrade device performance." [46] The requirement for further miniaturization outdated LOCOS and was superseded by Shallow Trench Isolation

(a) Schematic of nanowire fabrication   (b) Nanosize tip
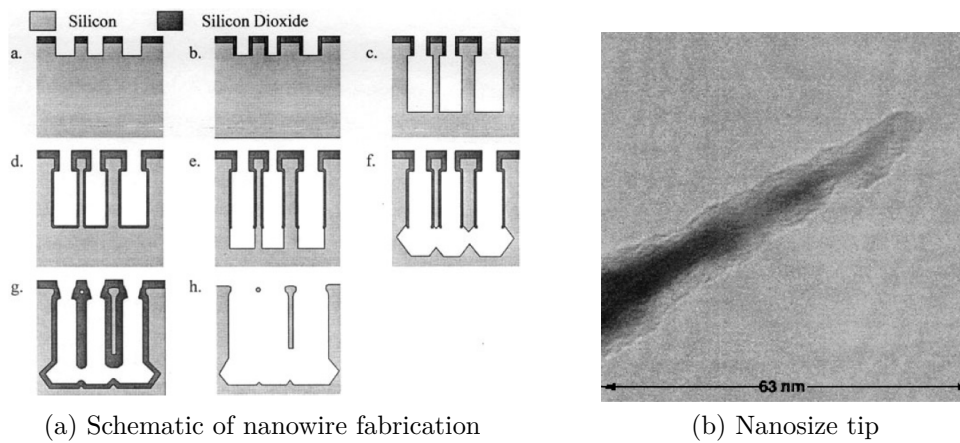
Figure 2.3: Silicon nanostructures. For details of (a) see [74], for (b) see [75].

(STI). STI is used on CMOS (Complementary Metal-Oxide-Semiconductor) process technology nodes of 250 nanometers and smaller. The range of applied temperatures is similar to that of LOCOS. "This process basically involves shallow trenching of the surface areas which are to be oxidized so as to obtain, as closely as possible, a planar surface after oxide growth. A very difficulty experienced in such steeped structures is that the oxide thickness on the edges are in the corners of trench can be much less than on flat surface. This is quite similar to thinning problems encountered in LOCOS structures." [46]

More recently silicon oxidation has been used to manufacture extremely small silicon structures on the nanoscale. Two examples are shown in Fig. 2.3: The manufacturing steps of silicon wires ranging from 200 to 20 nm in diameter [70] and a real nanosize silicon tip [75]. The oxidation process of such nanosilicon structures is typically performed at 850 °C (*cf.*, [33]) or 950 °C (*cf.*, [71]), *i.e.*, at temperatures similar to those used for LOCOS and STI. Interestingly the nanosize silicon beams buckle without external loads being applied. We shall see now that this behavior has the same cause as the insufficient oxide layer thickness described in context with LOCOS and STI.

2.2 Quantifying the volume expansion

In order to understand and interpret these facts we must first realize that the reaction described by Eqn. (2.1.2) is accompanied by a change in volume and, consequently, by generating eigenstrains and eigenstresses. The latter are sometimes also referred to as residual stresses in the engineering literature. To be specific, according to Kao in 1988 *et al.* [42], pg. 29, the unit cell of silicon is $20\,\text{Å}^3$, whereas that of silicon dioxide is $45\,\text{Å}^3$. Note that in [42] it is not explained where these numbers come from. If such a large increase in volume is correct, the resulting eigenstrains will be enormous. Thus, before we engage

in a discussion which kind of strain measure should be used for quantification, the validity of the data provided in [42] should be carefully checked.

A difference of $V_k = 25 \, \text{Å}^3$[1] between the two unit cell volumes is mentioned by Sutardja and Oldham in 1989 [87], pg. 2415. The agreement with Kao *et al.* [42] is not surprising, since they use that paper as a reference. However, it is argued by them that a more proper value for the difference should be $12.5 \, \text{Å}^3$ which, supposedly, is related to the difference between the distances of an Si-O (not SiO_2) and a Si-Si bond. Then it is said in [87] that "... The actual value of V_k used is obtained through numerical experiments, and the theoretical value of $12.5 \, \text{Å}^3$ is used as a test for the validity of the model." We strongly oppose to such a notion: A model should never be fitted to experiments, because then it is not a valid representation of reality. We therefore turn to the most detailed data survey presented in Mohr *et al.* [51], pg. 681 to find that the unit cell volume of Si is indeed $12.0588349 \times 10^{-3} \, \text{m}^3/\text{kmol}$, hence, $V_{\text{Si}} = \frac{12.0588349 \times 10^{-6} \, \text{m}^3/\text{kmol}}{N_{\text{Avo}}} \approx 20 \, \text{Å}^3$.

Finding a reliable value for the molecular volume of SiO_2 is more tedious. Valuable guides are, first, the Wikipedia article on silicon dioxide, [97] and, second, the discussion on ResearchGate, [77]. From both we realize that the silicon dioxide of our microelectronics application is not "quartz" but rather the amorphous variant of silicon dioxide. Moreover, note that Si has a mass density of $2329 \, \text{kg/m}^3$ (at room temperature, [75]) and, as mentioned in the previous references, quartz, or more precisely Si_3O_6, has a mass density of $2648 \, \text{kg/m}^3$, whereas the mass density of amorphous SiO_2 is only about $2200 \, \text{kg/m}^3$. The mass density of liquid SiO_2 is even less, namely approximately $2020 \, \text{kg/m}^3$. The molar masses of silicon and silicon dioxide are easily obtained from Mendeleev's table of elements, namely, $M_{\text{Si}} = 28.084 \, \text{kg/kmol}$ and $M_{SiO_2} = 60.082 \, \frac{\text{kg}}{\text{kmol}}$, respectively. In this paper we will use $N_{\text{Avo}} = 6.02214129 \times 10^{26} \, 1/\text{kmol}$ for Avogadro's number.[2] In combination with the mass densities and Avogadro's number we now obtain for the unit cell volumes:

$$V_{\text{Si}} = \frac{M_{\text{Si}}}{\rho_{\text{Si}} N_{\text{Avo}}} \approx 20.0 \, \text{Å}^3 \; , \qquad V_{SiO_2} = \frac{M_{SiO_2}}{\rho_{SiO_2} N_{\text{Avo}}} \approx 45.3 \, \text{Å}^3 . \qquad (2.2.1)$$

This, at last, gives us more confidence in the numbers for the volume changes presented by Kao *et al.* [42]. If we omit Avogadro's number in the last equation we obtain the so-called molar volumes:

$$v_{\text{Si}} = \frac{M_{\text{Si}}}{\rho_{\text{Si}}} \approx 0.012 \, \frac{\text{m}^3}{\text{kmol}} \; , \qquad v_{SiO_2} = \frac{M_{SiO_2}}{\rho_{SiO_2}} \approx 0.027 \, \frac{\text{m}^3}{\text{kmol}} . \qquad (2.2.2)$$

This confirms the statement in Rao and Hughes [72] according to which the "molar volume of silicon dioxide is 2.2 times that of silicon." The numbers also

---

[1]The index k refers to the surface reaction rate parameter k from [87], for which the difference in volume is used in an Arrhenius ansatz.

[2]Note that molar masses have an SI-unit, namely g/mol or kg/kmol, [96]. Moreover, for the sake of clarity, we should use particles/kmol as units of the Avogadro number. However, "particles" is no official SI-unit.

agree with the following data that was provided in Freidin *et al.* [28] without reference: $\rho_{\mathrm{Si}}/M_{\mathrm{Si}} = 82.9\,{}^{\mathrm{kmol}}\!/_{\mathrm{m^3}}$ and $\rho_{\mathrm{SiO_2}}/M_{\mathrm{SiO_2}} = 36.6\,{}^{\mathrm{kmol}}\!/_{\mathrm{m^3}}$. In combination with the molar masses this, in turn, leads to density values of $\rho_{\mathrm{Si}} = 2328\,{}^{\mathrm{kg}}\!/_{\mathrm{m^3}}$ and $\rho_{\mathrm{SiO_2}} = 2199\,{}^{\mathrm{kg}}\!/_{\mathrm{m^3}}$, respectively, which essentially agrees with the data in the wikis on silicon, [98] and [97]. By using Avogadro's constant we can convert this data also into unit cell volumes, $V_{\mathrm{Si}} = 20.0\,\text{Å}^3$ and $V_{\mathrm{SiO_2}} = 45\,\text{Å}^3$, respectively. This clearly indicates that the data of Kao *et al.* [42] were initially used in Freidin *et al.* [28] and then transformed accordingly. In other words, one went in circles as far as the unit cell data for amorphous silicon dioxide is concerned.

In summary, we may say that, first, the molar masses of Si and $\mathrm{SiO_2}$ are reliable. Second, the unit cell of silicon has been accurately examined by crystallographic methods using X-ray techniques by Mohr *et al.* [51]. Third, the silica resulting from the oxidation process has been identified as the amorphous form. Fourth, the mass density of amorphous silica has been determined experimentally with sufficient accuracy either by weighing or by back scattering of alpha particles (*cf.*, [76]). Hence we conclude that the unit cell volumes for silicon and silicon dioxide presented by Kao *et al.* [42] are realistic. We are now in a position to use this data to calculate eigenstrains.

2.3   Modeling the residual strains and stresses

Obviously, the change in volume during silicon oxidation is considerable and, consequently, the eigenstrains and eigenstresses will also be very large, at least in the beginning. It is for this reason, that it is adequate to use strain measures of *nonlinear* continuum mechanics. Fig. 2.4, which is an adapted form of a cartoon from Freidin *et al.* [28], illustrates the situation: Originally stress-free silicon (depicted in cyan) is penetrated by oxygen from the left up to the dashed line (the reaction front). If the corresponding region were free it would change its volume (and maybe also its shape) to the stress-free configuration shown in red on the bottom. We characterize the corresponding deformation by the deformation gradient $\boldsymbol{F}^{\mathrm{ch}} \equiv \boldsymbol{F}^{\mathrm{ox}}$ and are inclined to write according to seemingly standard nonlinear continuum mechanics procedures (see, *e.g.*, [35], pg. 79 or [60], pg. 73):

$$\rho_{0,\mathrm{SiO_2}} = \frac{\rho_{0,\mathrm{Si}}}{\det \boldsymbol{F}^{\mathrm{ox}}}, \tag{2.3.1}$$

where the subscripts 0 refer to the mass densities of silicon dioxide and silicon, both in a *undeformed* state. However, this formula does *not* apply, because it holds only if the mass within the material volume is conserved. This, however, is *not* the case here: Oxygen enters the volume element, causes the chemical reaction and leads to an increase in mass. Hence, an alternative relation must hold. In fact, it can take various forms as we shall see now. We start from the following purely kinematic relation between the unit cell volumes (*cf.*, [60], pg.

64) and find successively:

$$V_{\mathrm{SiO_2}} = \det \boldsymbol{F}^{\mathrm{ox}} V_{\mathrm{Si}} \quad \Rightarrow \quad \det \boldsymbol{F}^{\mathrm{ox}} = \frac{\frac{M_{\mathrm{SiO_2}}}{N_{\mathrm{Avo}}} \frac{V_{\mathrm{SiO_2}}}{m_{\mathrm{SiO_2}}}}{\frac{M_{\mathrm{Si}}}{N_{\mathrm{Avo}}} \frac{V_{\mathrm{Si}}}{m_{\mathrm{Si}}}} \equiv \frac{M_{\mathrm{SiO_2}} \rho_{0,\mathrm{Si}}}{M_{\mathrm{Si}} \rho_{0,\mathrm{SiO_2}}} \equiv \frac{v_{\mathrm{SiO_2}}}{v_{\mathrm{Si}}}, \qquad (2.3.2)$$

because the mass in one silicon or silicon dioxide unit cell is given by $m_{\mathrm{Si}} = \frac{M_{\mathrm{Si}}}{N_{\mathrm{Avo}}}$ and $m_{\mathrm{SiO_2}} = \frac{M_{\mathrm{SiO_2}}}{N_{\mathrm{Avo}}}$, respectively.
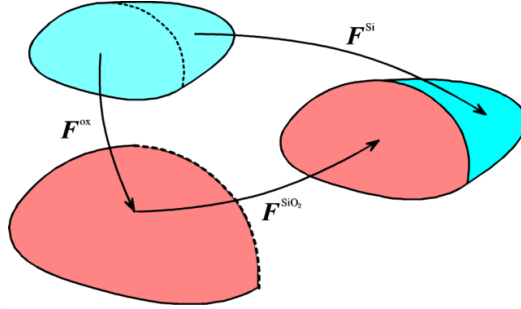
Figure 2.4: A schematic of the deformation during silicon oxidation.

On first glance it seems reasonable to assume that amorphous silica is isotropic and that it expands isotropically when it is created. Hence the deformation gradient is proportional to the unit tensor, $\mathbf{1}$, and we may conclude that:

$$\boldsymbol{F}^{\mathrm{ox}} = F^{\mathrm{ox}} \, \mathbf{1} \quad \Rightarrow \quad F^{\mathrm{ox}} = \left(\frac{v_{\mathrm{SiO_2}}}{v_{\mathrm{Si}}} \right)^{1/3}. \qquad (2.3.3)$$

An appropriate finite strain measure is the Green-Lagrangian strain tensor, $\boldsymbol{E} \equiv \frac{1}{2} \left(\boldsymbol{F}^{\mathrm{T}} \boldsymbol{F} - \mathbf{1} \right)$. From its definition we find[2]:

$$\boldsymbol{E}^{\mathrm{ch}} \equiv \boldsymbol{E}^{\mathrm{ox}} = \frac{1}{2} \left[\left(\frac{v_{\mathrm{SiO_2}}}{v_{\mathrm{Si}}} \right)^{2/3} - 1 \right] \mathbf{1} \approx 0.36 \, \mathbf{1}. \qquad (2.3.4)$$

36% is an extremely large strain. However, before we discuss how this extreme situation is dealt with in the literature, a comment regarding the *isotropy* of the deformation gradient $\boldsymbol{F}^{\mathrm{ox}}$ or, more suggestively speaking, on the "volumetric swelling" during thermal oxidation, is in order. This assumption seems to be generally accepted in the silicon industry. However, it seems noteworthy that most recently *anisotropic* swelling during lithiation of Si nanowires has been observed [48] or be discussed in context with Li-batteries [43]. The reason for this "is attributed to the interfacial processes of accommodating large volumetric strains at the lithiation reaction front that depend sensitively on the crystallographic orientation." [48] Note that modeling such an effect would

---

[2]The letters "ch" are used in [28] to characterize the chemical reaction, *i.e.*, the oxidation, why we use "ox" as a mnemonic.

not necessitate abandoning an isotropic dependence analogously to the one shown in Eqn. (2.3.4). Rather it will require taking the crystal orientation of the silicon during the joining procedure into account. The latter is shown in Fig. 2.4 on the very right indicated by the deformation gradients $\boldsymbol{F}^{\text{Si}}$ and $\boldsymbol{F}^{\text{SiO}_2}$. When modeling silicon oxidation we have to proceed as in the case of lithiation: The anisotropic elastic material properties of the to-be-oxidized wafer should enter the analysis. However, for simplicity we will ignore this for now and treat the silicon as an isotropic linear elastic material with effective elastic properties.

Clearly, after joining the connected materials will react to the large amount of strain predicted by Eqn. (2.3.4) and try to accommodate it somehow. There are various ways. The simplest, from a materials theory point-of-view, is time-dependent stress relaxation due to visco-elastic behavior. In fact, silicon dioxide is prone for such behavior if we only think of it as vitreous, *i.e.*, being in a glassy state. After all, "glasses" are nothing else but silica with certain additives. We know that they are capable of viscoelastic flow, even at low temperatures.[2]

Consequently, viscoelastic models are also used in many publications on thermal oxidation of silicon. Most surprisingly, 1988 Kao *et al.* used a *genuine fluid mechanics model* of the Newton-Navier-Stokes type in order to capture the effects of viscosity in their 1988 paper [42]. Their idea was picked up one year later by Satardja and Oldham [87], who changed their modeling to a one-dimensional dashpot-spring model for solids of the Maxwell type. A more detailed, truly multi-axial viscoelastic stress-strain analysis was performed by Senez *et al.* in 1994 [81]. More recently Lin [46] refers on pg. 8 of his 1999 work [46] to the transformation strain as "viscoplastic," probably erroneously, because on pg. 9 he cites the work of Satardja and Oldham and Senez *et al.*, which is clearly based on viscoelasticity. In any case he characterizes silicon as non-viscous, linear elastic.

The recent dissertation of Pezyna from 2005 [70] is more precise as far as terminology is concerned. First of all the importance of SiO_2's susceptibility to viscous flow is acknowledged (pg. 14): "However, at elevated temperatures, silica and silicate glasses are not purely elastic solids and can deform in a viscoelastic manner [...]" Then an interesting statement follows: "Consequently, the intrinsic strain is partly accommodated by viscous deformation, allowing the volume increase to be manifested chiefly as an increase in thickness. The remaining elastic strain, which will be referred to as the growth strain, ε_g, gives rise to the observed growth stress."

We interpret his words as follows: Initially, the silica expands essentially freely in perpendicular direction to the constraining silicon. As mentioned explicitly by Pyzyna[70] on pg. 57 silicon deforms elastically and definitely *not* viscoelastically or viscoplastically. Note that the main expansion in thickness

---

[2]visible, for example, in the thickening at the bottom of old church windows

direction is not an indication for an anisotropy of the eigenstrain, *i.e.*, a non-spherical form of $\boldsymbol{F}^{\mathrm{ch}} \equiv \boldsymbol{F}^{\mathrm{ox}}$. The silicon simply provides an elastic constraint, so that the main part of deformation due to purely volumetric expansion of silica goes where there is no constraint, namely perpendicularly to the reaction front. Clearly, along the interface the stretch will initially be more than allowed by linear elasticity, simply due to the need of the forming silica for very large expansion. However, the associated stresses will relax as time goes on and the stretch will eventually be reduced to the amount allowed by Hooke's law.

The situation can be understood in terms of the well-known experiments performed on a viscoelastic strip with Young's modulus E. In the first experiment the strip is suddenly subjected to a dead load, σ_0, which leads to instantaneous stretching and subsequent relaxation to the amount allotted by Hooke's law:

$$\epsilon_{\mathrm{ini}} = \frac{\tau_\sigma}{\tau_\epsilon} \frac{\sigma_0}{E} \quad \rightarrow \quad \epsilon_{\mathrm{H}} = \frac{\sigma_0}{E}. \tag{2.3.5}$$

In a second experiment the beam is suddenly elongated by a fixed amount in axial direction and then clamped, so that a strain ϵ_0 results. The response is instantaneous in terms of a tensile stress which will then relax from its initial value to that dictated by Hooke's law (*cf.*, [56], pg. 370):

$$\sigma_{\mathrm{ini}} = \frac{\tau_\epsilon}{\tau_\sigma} E\epsilon_0 \quad \rightarrow \quad \sigma_{\mathrm{H}} = E\epsilon_0. \tag{2.3.6}$$

The relaxation is governed by two time parameters, first, the so-called bulk relaxation time, dealing with relaxation under pure compression, $\tau_\epsilon = \eta_\epsilon / k$, where η_ϵ and k denote the bulk viscosity and the bulk modulus, respectively. The second time parameter is characteristic for shear loading, $\tau_\sigma = \eta_\sigma / G$, η_σ and G denoting shear viscosity and shear modulus, respectively. According to Freidin *et al.* [28] we have $E = 60\,\mathrm{GPa}$, Poisson's ratio $\nu = 0.17$, hence $k = \frac{E}{3(1-2\nu)} \approx 30.3\,\mathrm{GPa}$ and $G = \frac{E}{2(1+\nu)} \approx 25.6\,\mathrm{GPa}$. Similar numbers and approximately the same trend between them are shown by Dingwell and Webb [18], who report $k = 43\,\mathrm{GPa}$ and $G = 33\,\mathrm{GPa}$. Surprisingly the trend is reversed in Rao *et al.* [73], who use $k = 12.158\,\mathrm{GPa}$ and $G = 40.921\,\mathrm{GPa}$. The correctness of the number for the modulus of compressibility when compared to the shear modulus is hard to believe. Moreover, equations from Dingwell and Webb [18] lead us to conclude that both viscosities are equal. Consequently, due to lack of data, we choose $\eta_\sigma = \eta_\epsilon \approx 2 \times 10^4\,\mathrm{GPa\,s}$ (at $1000\,^\circ\mathrm{C}$, [81]), which gives $\tau_\sigma / \tau_\epsilon = G/k \approx 0.84$, $\tau_\sigma \approx 780\,\mathrm{s}$, and $\tau_\epsilon \approx 660\,\mathrm{s}$. A single relaxation time is presented in [73], namely $\tau_{\mathrm{SiO_2}} = 132.49\,\mathrm{s}$. In order to be able to compare it to the times required for the diffusion process, recall the time parameter from the definition of the Fourier number in context with the diffusion (or the heat conduction) equation (*e.g.*, [12], Chapter 4):

$$\tau_{\mathrm{diff}} = \frac{l^2}{D}, \tag{2.3.7}$$

where l is a characteristic length parameter and D the diffusion constant. Finding a reliable number for the diffusion coefficient of oxygen in silica is difficult, because the literature is inconclusive. Lin [46], pg. 11 reports $D = 1.83 \times 10^{-14} \, \frac{\mathrm{m}^2}{\mathrm{s}}$, allegedly based on data from the paper of Deal and Grove [17], who use a constant B that is related to D but in a complicated manner. Moreover, B is temperature dependent. Thus, it remains unclear how his value was obtained and under which circumstances it is valid. Rao *et al.*, pg. 374 [73] use in their simulations a value which is four (!) orders of magnitude larger, namely $D = 1.3786 \times 10^{-10} \, \frac{\mathrm{m}^2}{\mathrm{s}}$. They do not explain where this number comes from. A typical maximum layer thickness of silica is $l = 2 \, \mu\mathrm{m}$ (*cf.*, [29]). Hence we find $\tau_{\mathrm{diff}} = 2.9 \times 10^{-2} \ldots 218 \, \mathrm{s}$.

In comparison with τ_σ and τ_ϵ we must conclude that diffusion will either proceed much faster than the relaxation of stresses and strains due to viscoelastic effects, or will be of the same order of magnitude. Hence, if we want to assess *stress-induced diffusion* it is, in principle, necessary to solve the coupled chemo-mechanical problem in combination with three-dimensional viscoelastic constitutive equations. This will make the problem explicitly time-dependent and impossible to solve analytically, even for the simple geometry of a planar layered structure. On the other hand, we also want to investigate the features of our stress-assisted diffusion model. They can be explored easily if an analytical solution for the stresses and strains is available. This, however, is only possible if we restrict ourselves to linear elasticity, *i.e.*, to Hooke's law:

$$\boldsymbol{\sigma} = \lambda \, \mathsf{Tr}\left(\boldsymbol{\epsilon} - \boldsymbol{\epsilon}^{\mathrm{ch}}\right) \mathbf{1} + 2\mu \left(\boldsymbol{\epsilon} - \boldsymbol{\epsilon}^{\mathrm{ch}}\right), \tag{2.3.8}$$

where $\boldsymbol{\sigma}$ is the Cauchy stress tensor and $\boldsymbol{\epsilon}$ refers to the *linear* strain tensor which is related to the displacement vector $\boldsymbol{u}$ as follows:

$$\boldsymbol{\epsilon} = \tfrac{1}{2}\left(\nabla \boldsymbol{u} + \nabla \boldsymbol{u}^\top\right). \tag{2.3.9}$$

Obviously the reaction strain $\boldsymbol{\epsilon}^{\mathrm{ch}}$ must be known numerically before we can proceed with the stress-strain analysis and, what is more, it should be compatible with the assumption of small strains, *i.e.*, it should assume a value in the percent range, at most. As in the case of large deformations, *cf.*, Eqns. (2.3.3) and (2.3.4), the linear transformation strain is isotropic, hence:

$$\boldsymbol{\sigma} = \lambda \, \mathsf{Tr}\,\boldsymbol{\epsilon} \, \mathbf{1} + 2\mu \, \boldsymbol{\epsilon} - 3k\epsilon^{\mathrm{ch}}\mathbf{1}, \tag{2.3.10}$$

with the bulk modulus being $k = \tfrac{1}{3}\left(3\lambda + 2\mu\right)$. Freidin *et al.* [28] choose $\epsilon^{\mathrm{ch}} = 0.03$. Besides a reference to the necessity for small strains and the fact that this particular value allows them to show an effect of the eigenstesses on diffusion within their theoretical framework they do not provide any reason for their choice of this value. However, there is an alternative way for obtaining a number for ϵ^{ch} by using the following relation for small deformations from [60], pg. 232:

$$\epsilon^{\mathrm{ch}} = \frac{\rho_{0,\mathrm{Si}} - \rho_{0,\mathrm{SiO}_2}}{3\rho_{0,\mathrm{SiO}_2}}. \tag{2.3.11}$$

If we insert the data for the mass densities we obtain $\epsilon^{\text{ch}} \approx 0.02$. This is very close to the value from [28]. Note that Eqn. (2.3.11) is a consequence of Eqn. (2.3.4). To see that we assume, first, that the difference between the molecular volumes v_{SiO_2} and v_{Si} is small such that we obtain after a Taylor expansion:

$$\boldsymbol{E}^{\text{ch}} \approx \frac{v_{\text{SiO}_2} - v_{\text{Si}}}{3v_{\text{Si}}} \mathbf{1}. \tag{2.3.12}$$

Second, we assume that the molar masses are equal, observe Eqn. (2.2.2) and obtain:

$$\boldsymbol{E}^{\text{ch}} \approx \frac{\rho_{\text{Si}} - \rho_{\text{SiO}_2}}{3\rho_{\text{SiO}_2}} \mathbf{1} \equiv \epsilon^{\text{ch}} \mathbf{1}. \tag{2.3.13}$$

The agreement is not surprising since a relation analogous to Eqn. (2.3.11) was used in [60] in context with the description of the phase transformation in Zirconia. Then masses within the unit cells stay constant and the molar mass does not change. However, in the present case we have $M_{\text{Si}}{=}28.084\frac{\text{kg}}{\text{kmol}}$ and $M_{\text{SiO}_2}{=}60.082\frac{\text{kg}}{\text{kmol}}$, which are extremely different. We conclude that it is the additional mass flow of oxygen into the unit cell that prevents us from using simple relations as Eqn. (2.3.11) and, in the end, from using linear elasticity with no hesitation whatsoever.

2.4 Intuitive explanations and empirical quantification of the impediment encountered during silicon oxidation

It was mentioned in Subsection 2.1 that the growth of silicon oxide layers is impeded severely if the insulation windows used in the LOCOS process become very narrow and that the oxide thickness becomes thinner on the edges of the trenches produced in STI. On the other hand, it is well known in mechanics that corners and the closeness of substructures are excellent stress and strain amplifiers. Hence, in view of the huge eigenstrains inherent to silicon oxidation it seems only natural to suspect that the associated stresses and strains in the material might reach a level high enough to influence the course of reaction and diffusion dramatically.

Marcus and Sheng [49] were among the first to emphasize the importance of stress for silicon oxidation. Shortly after their paper it was directly demonstrated in 1987 by Huang *et al.* [39] that mechanical stress influences the rate of silicon oxidation. In two papers in the same and the following year Kao *et al.* [41] and [42] start modeling the stresses in cylindrical structures and attempt a coupling between the reaction rate and the radial stress component. One year later Sutarya and Oldham [87] become even more specific. Following the tradition of materials science they relate the impact of the normal stress,

σ_{nn}, and of *pressure, i.e.*, the trace of stress, $\mathsf{Tr}\,\sigma$, *empirically* to two constitutive quantities, first, the surface reaction rate parameter, k_{s}, and second, the diffusion coefficient, D in terms of an exponential Boltzmann ansatz, namely:

$$k = k_{s0}(T)\exp\left(\frac{\sigma_{nn}V_k}{kT}\right)\,,\ D = D_0(T)\exp\left(-\frac{pV_d}{kT}\right), \qquad (2.4.1)$$

where k_{s0} and D_0 are the temperature dependent reaction and diffusion coefficients for the stress-free (called "planar" in [87]) case, k is Boltzmann's constant, T absolute temperature, V_k and V_d are two fitting parameters, which have the dimension of a volume. The shear viscosity, η, is "adjusted" in a similar manner:

$$\eta = \eta_0(T)\frac{\sigma_s V_0/2kT}{\sinh\left(\sigma_s V_0/2kT\right)}, \qquad (2.4.2)$$

where η_0 denotes the shear viscosity the temperature dependent reaction and diffusion coefficients in the stress-free case, and V_0 is another fitting parameter, explicitly characterized as such in the paper.

That all of this is a completely heuristic approach, becomes obvious if we try to guess why the authors may have come up with such expressions: On can imagine that a normal stress acting compressively on the reaction front will keep the molecules away from each other and defer the progress of the reaction. It seems also logical to assume that diffusion in a solid under pressure will be procrastinated because the atoms will then be more densely "packed" and harder to bypass and, finally, viscous Newtonian flow is triggered by shear stress, so the viscosity might depend on it in a nonlinear manner.

Of course, the authors of [87] assume us to be "intelligent" readers with an intuitive gut feeling to anticipate all that. They scarcely motivate their approach by saying "The model states that the oxidizing species need to have enough energy to move the newly formed oxide against the normal force field σ_{nn}. The energy required in a unit reaction is the product of one reaction jump volume V and σ_{nn}. Assuming the Boltzman[n] statistics, the reaction probability varies (with energy) according to the factor $\exp\left(\sigma_{nn}V_k/kT\right)$." It is this concoction of atomistic arguments with field quantities which makes a true continuum scientist used to first principles shudder. However, later we shall use some of these relations and see if and how they alter predictions of a theory in which diffusion and mechanics are coupled but which initially uses stress-independent material coefficients. In other words the mechano-chemical coupling is achieved differently. The next section will explain how.

2.5   Driving forces at the reaction front

From the perspective of modern continuum theory silicon oxidation can be modeled in terms of a singular interface theory. Such a model is useful if the interface is relatively sharp, *i.e.*, the fields on the left and right hand side of the

jump in a discontinuous fashion and a high gradient in mass density (say, among other fields) results over a short distance, much smaller than the dimensions of the considered piece of matter. A first attempt in that direction from a mathematical point-of-view was presented in 1994 by Merz and Strecker [50]. They also touch upon an alternative way of modeling silicon oxidation, which could be phase-field theory. However, their primary focus is on mathematical formalities and less on a quantitative physical description.

A major breakthrough in terms of rational continuum theory was presented recently by Freidin *et al.* [25], [27], [28], [26]. In their papers the idea of the Eshelby stress tensor, $\boldsymbol{B}$, being the driving force behind silicon oxidation was brought to (qualitative) perfection. The specific Eshelby tensor or, more precisely, the specific Eshelby energy-momentum tensor (in SI-units of $J\,kg^{-1}$), is defined by (*cf.*, [32], pg. 4 and 25, [47]):

$$\boldsymbol{B} = f\boldsymbol{1} - \frac{1}{\rho_0}\boldsymbol{F}^\top \cdot \boldsymbol{P} \quad \Leftrightarrow \quad B_{AB} = f\,\delta_{AB} - \frac{1}{\rho_0}F_{Ai}P_{iB}, \qquad (2.5.1)$$

where $f = u - Ts$ denotes the specific free energy density in a material point (u and s being the specific internal energy and entropy densities), ρ_0 is the mass density of the reference configuration, $\boldsymbol{F}$ denotes the deformation gradient with its determinant, $J = \det\boldsymbol{F}$, and $\boldsymbol{P} = J\boldsymbol{\sigma} \cdot \boldsymbol{F}^{-\top} \Leftrightarrow P_{iA} = J\sigma_{ij}\left(F^{-1}\right)^\top_{jA} \equiv J\sigma_{ij}F^{-1}_{Aj}$ is the first (nonsymmetric) Piola-Kirchhoff stress tensor, and $\boldsymbol{\sigma}$ denotes the (symmetric) Cauchy stress tensor. Moreover, Eqn. (2.5.1) shows that $\boldsymbol{B}$ is completely based in the reference configuration (distinguished by a capital symbol and capital Latin indices in contrast to the current configuration which is characterized by small Latin indices for Cartesian coordinates).

However, silicon oxidation is only one of the more recent applications of the Eshelby tensor. Originally Eshelby used it for quantifying driving forces on defects, in particular on (linear) elastic inclusions, see [22], [23]. Shortly after, or one may say in parallel, the energy-momentum tensor became the playing ground of the fracture mechanics community, where it arose under the name J-integral, a term coined by Rice [78], [8]. However, it is fair to say that the mechanics community simply failed to see the thermodynamic character of the energy-momentum tensor. This was first acknowledged by Heidug and Lehner [37]. Other references in the same context are the papers by Truskinovsky [90], Liu [47], Gurtin [31], Cermelli and Gurtin [13], Müller [55], and and Buratti *et al.* [9].

In these papers it was pointed out that $\boldsymbol{B}$ can be considered as a tensorial generalization of the scalar chemical potential, μ, which is the driving force behind diffusion and reactions in gases and liquids. More precisely, in a reaction where i reactants go in and j products come out, so that in total $k = i + j$ substances are involved, one may define the corresponding *chemical affinity* in terms of the corresponding chemical potentials, μ_k, weighted by the

stoichiometric coefficients, n_k, and the molar masses, M_k:

$$A = -\sum_k n_k M_k \mu_k = +\sum_{\text{in},i} |n_i| M_i \mu_i - \sum_{\text{out},j} n_j M_j \mu_j. \qquad (2.5.2)$$

This notion is explained, for example, in the textbook on chemical thermodynamics by Prigogine and Defay [68], Chapter III, Section 3 ff. and Chapter IV. If the entropy principle is evaluated for chemical reactions between fluids and gases one finds that the so-called overall reaction rate, ω, a "speed," and the scalar affinity, A, are related by the so-called de Donder inequality and de Donder equation [67]:

$$D = A\omega \geq 0 \, , \ \omega = \vec{\omega} \left[1 - \exp\left(-\frac{A}{RT}\right) \right] \approx \vec{\omega} \frac{A}{RT}, \qquad (2.5.3)$$

where D is the dissipation and $\vec{\omega}$ the forward reaction rate. The latter is not a vector as the strange chemical engineering notation might lead us to suspect. The arrow is merely supposed to indicate a forward reaction. In fact, in equilibrium, for which Eqn. $(2.5.3)_2$ holds, we may write $\vec{\omega} = \overleftarrow{\omega}$, the latter being the backward reaction rate. In the terminology of TIP,[2] we may simply say that the de Donder results are nothing else but consequences following from exploitation of the entropy principle in combination with a linear flux-force concept. For mechanical engineers it seems worthwhile mentioning that the forward reaction rate can be interpreted as a volumetric flow of chemicals and, consequently, carries the units $\dim \vec{\omega} = \frac{\text{kmol}}{\text{m}^3} \frac{\text{m}}{\text{s}}$.

In the aforementioned papers by Freidin *et al.* it was pointed out that, first, in reactions involving solids the Eshelby tensors assume the role of the chemical potentials after double scalar multiplication with the normal vector, $\boldsymbol{N}$, corresponding to the reference configuration of a surface element of the reaction front:

$$\mu_k = \boldsymbol{N} \cdot \boldsymbol{M}_k \cdot \boldsymbol{N} \, , \ \ \boldsymbol{M}_k \coloneqq \boldsymbol{B}_k, \qquad (2.5.4)$$

where $\boldsymbol{M}_k$ is called the *chemical potential tensor* of species k. In fact, in the case of a gas or fluid we may write:

$$\boldsymbol{M} = \mu\boldsymbol{1}, \qquad (2.5.5)$$

Second, an analogue to the chemical affinity for solid reactions can be obtained as follows:

$$A_{NN} = -\sum_k n_k M_k \mu_k \equiv -\sum_k n_k M_k \boldsymbol{N} \cdot \boldsymbol{M}_k \cdot \boldsymbol{N}. \qquad (2.5.6)$$

In addition one can also define a chemical affinity tensor by:

$$\boldsymbol{A} = -\sum_k n_k M_k \boldsymbol{M}_k. \qquad (2.5.7)$$

---

[2]Thermodynamics of Irreversible Processes, see [56].

so that

$$A_{NN} = \boldsymbol{N} \cdot \boldsymbol{A} \cdot \boldsymbol{N}. \tag{2.5.8}$$

Third, evaluation of the entropy principle allows to show that the dissipation rate, D, is now given by:

$$D = A_{NN}\omega_N \geq 0, \tag{2.5.9}$$

where ω_N is the reaction rate at a surface element of the reaction front with the reference normal $\boldsymbol{N}$. The requirement for positive-definiteness of the dissipation rate is satisfied if we put:

$$\omega_N = \vec{\omega}\left[1 - \exp\left(-\frac{A_{NN}}{RT}\right)\right] \approx \vec{\omega}\frac{A_{NN}}{RT}, \tag{2.5.10}$$

where $R = 8.314\frac{\text{kJ}}{\text{kmol K}}$ denotes the ideal gas constant and T is absolute temperature.

ω_N is related to the normal propagation speed of the front. To make this explicit we will now specialize the equations to dry silicon oxidation according to Eqn. (2.3.2) and obtain from Eqns. (2.5.5) and (2.5.7):

$$\boldsymbol{A} = |n_-|\, M_-\boldsymbol{M}_- + |n_*|\, M_*\mu_*\boldsymbol{1} - n_+M_+\boldsymbol{M}_+ \equiv \tag{2.5.11}$$

$$-[\![n|\, M\boldsymbol{M}]\!] + |n_*|\, M_*\mu_*\boldsymbol{1},$$

where jump brackets, $[\![\cdot]\!]$, which are frequently used in context with singular interfaces, denote the difference of a quantity on the plus and on the minus side. This implies that all quantities involved are understood as "left" and "right" limit values and must be evaluated accordingly.

Before we start to detail this equation any further, it is only fair to point out that similar results have been presented in [47], [55], or [56], but not from a chemical engineering point-of-view and not in context with chemical reactions but for mass-conserved phase transformations. If we simplify their results we may write in analogy to Eqns. $(2.5.11)_2$ and Eqns. $(2.5.3)_1$ in terms of a mass flow across the singular interface:

$$\boldsymbol{N} \cdot [\![\boldsymbol{B}]\!] \cdot \boldsymbol{N}\rho W \geq 0, \tag{2.5.12}$$

where $W = \boldsymbol{V} \cdot \boldsymbol{N}$ is the velocity associated with the flow of mass, $\rho\boldsymbol{V}$, normal to the interface, w.r.t. the reference configuration. Hence within the framework of a linear theory we must put as in Eqns. $(2.5.10)_2$:

$$\rho W \sim \boldsymbol{N} \cdot [\![\boldsymbol{B}]\!] \cdot \boldsymbol{N}. \tag{2.5.13}$$

In view of this it is our next goal to rewrite Eqn. $(2.5.10)_2$ in terms of a normal velocity, which will allow us to study the growth and progression of an interface explicitly. However, in order to do that we must first introduce some kinematic relations pertinent to our reaction.

2.6 Mathematical treatment of silicon oxidation – The full picture

2.6.1 Relevant kinematic quantities

We will now go through the statements on kinematics made by Freidin *et al.* [25], [27], [28], [26] for a simple reason. For the sake of brevity the details in that paper had to be kept to a minimum and many things were left unsaid to be read between the lines. We also warn our readers to be ready to accept a notation which looks clumsy on first glance but which has proven to be necessary when studying chemical reactions of the kind specified in Eqn. (2.1.1).
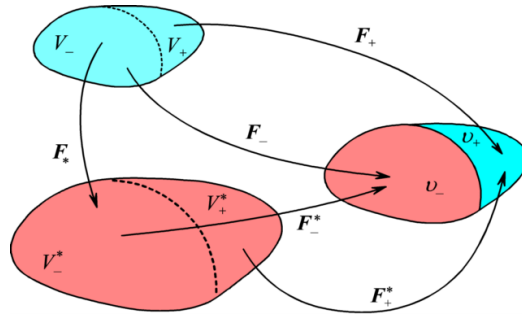

Figure 2.5: Kinematics of the solid-gas-solid reaction $n_- B_- + n_* B_* \rightleftharpoons n_+ B_+$.

Recall the general reaction shown in Eqn. (2.1.1) and consider the corresponding situation depicted in Fig. 2.5. In the configuration on the very right the gas "$*$" has penetrated the solid skeleton region v_+[2] up to the current interface, which is identifiable by a thick black line, γ. The region beyond that line, v_-, still contains original not reacted material. Due to the volume expansion both regions will deform and carry stresses and strains.

In order to characterize the deformation we consider two current linear segments, $\mathrm{d}\boldsymbol{x}_+ \in v_+$ and $\mathrm{d}\boldsymbol{x}_- \in v_-$, in both regions. We wish to link them to line segments in unstressed solid reference configurations. *Two* such configurations come to mind. The first one consists of a solid completely made of "$-$" material. It is shown on the upper left of the figure. The second one is a solid consisting exclusively of the product material, "$+$." It is shown on the lower left. Note that in both reference configurations we have indicated the images, Γ and Γ^*, of the current interface, γ, by black dotted lines. Clearly these are purely geometrical, unphysical objects. However, they allow us to identify four image volumes of $v_\pm$. These are denoted by $V_\pm$ and $V_\pm^*$, respectively. Again, they are purely geometrical objects. They are related to reference configurations, hence, the capital letters. Moreover, the upper index "$*$" is used to distinguish both sets from each other *and* to indicate that the second set is made of the reaction product due to the chemical reaction between the "$-$" material and the gaseous

---

[2]Note that we denote quantities of the current configuration by small letters.

agent "$*$." We are now in a position to link four linear line segments in the two reference configurations, $\mathrm{d}\boldsymbol{X}_\pm$ and $\mathrm{d}\boldsymbol{X}_\pm^*$, by means of deformation gradients, $\boldsymbol{F}$, as follows:

$$\mathrm{d}\boldsymbol{x}_\pm = \boldsymbol{F}_\pm \cdot \mathrm{d}\boldsymbol{X}_\pm \ , \ \ \mathrm{d}\boldsymbol{x}_\pm = \boldsymbol{F}_\pm^* \cdot \mathrm{d}\boldsymbol{X}_\pm^* \tag{2.6.1}$$

with $\mathrm{d}\boldsymbol{x}_\pm \in \upsilon_\pm$, $\mathrm{d}\boldsymbol{X}_\pm \in V_\pm$, and $\mathrm{d}\boldsymbol{X}_\pm^* \in V_\pm^*$. All of the mappings (*i.e.*, deformation gradients) used in these equations are shown in Fig. 2.5. From Eqns. (2.6.1) we get in the usual fashion Nanson formulae for the directed surface elements:

$$\mathrm{d}a_\pm \boldsymbol{n}_\pm = J_\pm \mathrm{d}A_\pm \ \boldsymbol{F}_\pm^{-\top} \cdot \boldsymbol{N}_\pm \ , \ \ \mathrm{d}a_\pm \boldsymbol{n}_\pm = J_\pm^* \mathrm{d}A_\pm^* \ \boldsymbol{F}_\pm^{*-\top} \cdot \boldsymbol{N}_\pm^* \tag{2.6.2}$$

and transformation relations for the volume elements:

$$\mathrm{d}\upsilon_\pm = J_\pm \mathrm{d}V_\pm \ , \ \ \mathrm{d}\upsilon_\pm = J_\pm^* \mathrm{d}V_\pm^*, \tag{2.6.3}$$

where J denote the determinants of the deformation gradients, *e.g.*, $J_-^* = \det \boldsymbol{F}_-^*$.

There is yet another mapping shown in the figure, namely $\boldsymbol{F}_*$. Note that it was not entitled $\boldsymbol{F}_\pm^*$, because it relates the stress-free reference configuration of the chemically unaffected to the fully affected one, independently of the regions $V_\pm$ and $V_\pm^*$. The symbol "$*$" was used to emphasize the relevance of the gaseous agent during the reaction.

Consequently, between the volume elements of the two stress free reference configurations the following relations hold:

$$\mathrm{d}V_\pm^* = J_* \mathrm{d}V_\pm, \ \ J_* = \det \boldsymbol{F}_*. \tag{2.6.4}$$

Moreover, as usual, multiplicative decomposition applies:

$$\boldsymbol{F}_\pm = \boldsymbol{F}_\pm^* \cdot \boldsymbol{F}_* \ \ \ \Rightarrow \ \ \ J_\pm = J_\pm^* J_*. \tag{2.6.5}$$

Note that Eqns. (2.6.4) and (2.6.5) are consistent with Eqns. (2.6.3) for we may write:

$$\mathrm{d}\upsilon_\pm = J_\pm \mathrm{d}V_\pm = J_\pm^* J_* \mathrm{d}V_\pm \equiv J_\pm^* \mathrm{d}V_\pm^*. \tag{2.6.6}$$

2.6.2   Mass densities

We now turn to the definition and calculation of several mass densities in the various configurations. This will be based on the conservation or addition of mass to the various volume elements involved. We start by saying that we consider the mass densities of the two stress free reference configurations, $V = V_+ \cup V_-$ and $V^* = V_+^* \cup V_-^*$, as given and we denote them by ρ_{0-} and ρ_{0+}^* [2],

---

[2]Note that in this case we depart from our convention that capital letters signal quantities in the reference configuration. The capital Greek letter rho looks like a P, which makes it difficult to recognize as a mass density. To make both ends meet we have decided to use an index 0 for indicating the reference configuration.

respectively. Moreover, we denote by dm_+ the mass of reaction product material "+" inside of the volume element dv_+ and (by definition) the mass inside of dV_+^{*}[3]. By dm_- we refer to the mass of the solid reactant component inside of dv_- and (by definition) inside of the volume elements dV_-[4]. Then we may write:

$$\rho_{0+}^{*} \equiv \frac{dm_+}{dV_+^{*}} = \frac{N_+ M_+}{N_{\text{Avo}} dV_+^{*}} \ , \ \ \rho_{0-} \equiv \frac{dm_-}{dV_-} = \frac{N_- M_-}{N_{\text{Avo}} dV_-}, \tag{2.6.7}$$

N_- and N_+ being the number of particles of "+" and "−" in the corresponding volume elements. The chemical reaction requires $\frac{N_+}{N_-} = \frac{n_+}{|n_-|}$ to hold. Then we find by mutual insertion:

$$\frac{\rho_{0-}}{\rho_{0+}^{*}} = \frac{|n_-| M_- dV_+^{*}}{n_+ M_+ dV_-} \equiv \frac{|n_-| M_-}{n_+ M_+} J^{*} \ \ \Rightarrow \ \ J_{*} = \frac{n_+ M_+ \rho_{0-}}{|n_-| M_- \rho_{0+}^{*}}. \tag{2.6.8}$$

The right hand side contains only known quantities and allows us to calculate the volumetric part of the deformation gradient $\boldsymbol{F}_{*}$. If we assume that the reaction occurs isotropically this is all we need to know. In this case we have:

$$\boldsymbol{F}_{*} = f_{*}\boldsymbol{1} \ \ \Rightarrow \ \ J_{*} = f_{*}^{3} \ \ \Rightarrow \ \ f_{*} = \left(\frac{n_+ M_+ \rho_{0-}}{|n_-| M_- \rho_{0+}^{*}}\right)^{1/3}. \tag{2.6.9}$$

As far as the *current* mass densities are concerned we may turn to Eqns.$(2.6.3)_1$ and write:

$$J_- = \frac{dv_-}{dV_-} = \frac{dv_- / dm_-}{dV_- / dm_-} = \frac{\rho_-}{\rho_{0-}} \ \ \Rightarrow \ \ \rho_- = J_- \rho_{0-}, \tag{2.6.10}$$

$$J_+ = \frac{dv_+}{dV_+} = \frac{dv_+ / dm_+}{dV_+ / dm_+} = \frac{\rho_+}{\rho_{0+}} \ \ \Rightarrow \ \ \rho_+ = J_+ \rho_{0+}.$$

Thus, as usual, both current densities can be calculated from the aforementioned reference densities once the deformations have been determined. Moreover, it is now straightforward to conceive two further reference densities, namely ρ_{0+}, *i.e.*, the mass density related to the product region of the reference configuration completely consisting of "−" material, and and ρ_{0-}^{*}, which is the mass density for the reactant region of the reference configuration completely made of "+" material. However, due to the way both reference configurations were constructed physics tells us that we must have $\rho_{0+} \equiv \rho_{0-}$ and $\rho_{0-}^{*} \equiv \rho_{0+}^{*}$. We now require the mass dm_- to be also present in dV_-^{*}. This is not self-evident, because after all dV_-^{*} belongs to the region V_-^{*}, which is completely made of "+" material. Since $dm_- = \rho_- dv_-$ we then find:

$$\rho_{0-}^{*} = \rho_- \frac{dv_-}{dV_-^{*}} = \rho_- \frac{dv_- / dm_-}{f_{*}^{3} dV_- / dm_-} \equiv \frac{\rho_{0-}}{f_{*}^{3}}, \tag{2.6.11}$$

---

[3]not inside of dV_-^{*}

[4]not inside of dV_+

because of Eqns. $(2.6.4)_1$ and $(2.6.9)_2$. Then because of the aforementioned equalities ρ_{0+} and ρ_{0-}^* we also immediately conclude that:

$$\rho_{0+}^* = \frac{\rho_{0-}}{f_*^3} \equiv \frac{\rho_{0+}}{f_*^3}. \tag{2.6.12}$$

The last set of mass densities to be introduced concerns the gaseous agent "$*$." In view of the previously established nomenclature its mass is given by $\mathrm{d}m_* = \rho_* \mathrm{d}\upsilon_+ = \rho_{0*}^* \mathrm{d}V_+^* = \rho_{0*} \mathrm{d}V_+$, where ρ_* is the current mass density of the gas, *i.e.*, a real and physics based quantity. Moreover, ρ_{0*}^* stands for the mass density of gas in the product region, V_+^*, of the reference configuration completely made of product material,"$+$." As such it is fictitious, *per se*. Finally, ρ_{0*} must be interpreted as the mass density of gas in the product region, V_+, of the reference configuration consisting exclusively of reactant material, "$-$." As such it is equally fictitious. Nevertheless, it is then possible to establish the following relations between them:

$$\rho_{0*} = \rho_{0*}^* \frac{\mathrm{d}V_+^*}{\mathrm{d}V_+} = \rho_{0*}^* J_* = f_*^3 \rho_{0*}^*, \tag{2.6.13}$$

where Eqn. $(2.6.4)_1$ has been used. Moreover,

$$\frac{\rho_*}{\rho_{0*}^*} = \frac{\mathrm{d}V_+^*}{\mathrm{d}\upsilon_+} = \frac{\mathrm{d}V_+^*/\mathrm{d}m_+}{\mathrm{d}\upsilon_+/\mathrm{d}m_+} = \frac{\rho_+}{\rho_{0+}^*}. \tag{2.6.14}$$

This relation shows that the gas densities in the reactant regions must match the corresponding densities of the solids in there. Later on we will also use gas concentration values. Concentrations can be obtained from the mass densities by dividing them by the molar masses. Hence we have:

$$c_0^* := \frac{\rho_{0*}^*}{M_*}, \quad c_0 := \frac{\rho_{0*}}{M_*} \equiv f_*^3 c_0^*, \tag{2.6.15}$$

the latter because of Eqn. $(2.6.13)$. c_0^* and $c_0{}^2$ should be interpreted as molar concentrations of the gas constituent in units of $\mathrm{kmol/m^3}$ related to the two regions V_- and V_-^* in the reference configurations made completely of "-" and of "+" material, respectively.

2.6.3 Stress tensors

Following the general definition of the first Piola stress tensor shown after Eqn. $(2.5.1)$ we may write down the following expressions for both regions of the two reference configurations:

$$\boldsymbol{P}_\pm = J_\pm \boldsymbol{\sigma}_\pm \cdot \boldsymbol{F}_\pm^{-\top}, \quad \boldsymbol{P}_\pm^* = J_\pm^* \boldsymbol{\sigma}_\pm \cdot \boldsymbol{F}_\pm^{*-\top}. \tag{2.6.16}$$

---

[2]Note that we do not write c_{0*}^* and c_{0*} because concentrations are only used in context with the gas constituent which makes a second index "$*$" unnecessary.

If we now use Eqn. (2.6.5) it is a matter of tensor algebra to show that $\boldsymbol{P}_\pm$ and $\boldsymbol{P}_\pm^*$ are related as follows:

$$\boldsymbol{P}_\pm = J_* \boldsymbol{P}_\pm^* \cdot \boldsymbol{F}_*^{-\top}. \tag{2.6.17}$$

Note that this relation does not make use of an isotropic form for $\boldsymbol{F}_\pm^{*-\top}$. However, if we make use of Eqn. $(2.6.9)_{1/2}$ we find that:

$$\boldsymbol{P}_\pm = f_*^2 \boldsymbol{P}_\pm^*. \tag{2.6.18}$$

If we now use this result and combine it with Eqn. $(2.6.5)_1$ and Eqn. (2.6.11) we find the following identity relevant for the tensors of chemical potentials:

$$\frac{1}{\rho_{0\pm}} \boldsymbol{F}_\pm^\top \cdot \boldsymbol{P}_\pm = \frac{1}{\rho_{0\pm}^*} \boldsymbol{F}_\pm^{*\top} \cdot \boldsymbol{P}_\pm^*. \tag{2.6.19}$$

Finally, based on the relations above the Nanson formulae Eqn. (2.6.2) allows us to prove the equality of the surface tractions of the current and the two reference configurations:

$$\boldsymbol{\sigma}_\pm \cdot \boldsymbol{n}_\pm \, \mathrm{d}a_\pm = \boldsymbol{P}_\pm \cdot \boldsymbol{N}_\pm \, \mathrm{d}A_\pm = \boldsymbol{P}_\pm^* \cdot \boldsymbol{N}_\pm^* \, \mathrm{d}A_\pm^*. \tag{2.6.20}$$

This shows very clearly that the concept of reference configurations is nothing but a mathematical convenience leaving the physics unchanged. In context with the last equation another remark is in order. The normals on the surfaces of the various involved regions, *i.e.*, $\partial v_\pm$, $\partial V_\pm$ and $\partial V_\pm^*$, point in outward direction. However, a part of these surfaces coincides with the interface, γ, Γ, or Γ^*. We define its normal, $\boldsymbol{n}$, $\boldsymbol{N}$, or $\boldsymbol{N}^*$ to point from the product to the reactant regions, "+" and "−", respectively. Hence, we may write $\boldsymbol{n} = -\boldsymbol{n}_- = \boldsymbol{n}_+$, $\boldsymbol{N} = -\boldsymbol{N}_- = \boldsymbol{N}_+$, and $\boldsymbol{N}^* = -\boldsymbol{N}_-^* = \boldsymbol{N}_+^*$. In particular, for an isotropic deformation according to Eqn. (2.6.9) we must have on the interface:

$$\boldsymbol{n} = \boldsymbol{N} = \boldsymbol{N}^* \quad \Rightarrow \quad \mathrm{d}A^* = f_*^2 \mathrm{d}A \tag{2.6.21}$$

the latter because of Eqns. (2.6.2) and (2.6.5).

2.6.4   Chemical affinities and their jumps − The general case

We now return to Section 2.5 and obtain the following explicit expressions for the two chemical potential tensors and the chemical potential involved in Eqn. (2.5.11):

$$\boldsymbol{M}_- = f_- \boldsymbol{1} - \frac{1}{\rho_{0-}} \boldsymbol{F}_-^\top \cdot \boldsymbol{P}_-, \; \boldsymbol{M}_+ = f_+ \boldsymbol{1} - \frac{1}{\rho_{0+}^*} \boldsymbol{F}_+^{*\top} \cdot \boldsymbol{P}_+^*, \; \mu_* = f_* + \frac{p_*}{\rho_*}. \tag{2.6.22}$$

If we make use of Eqns. (2.6.9), (2.6.12), and (2.6.19) the chemical affinity tensor (2.5.11) may be rewritten as follows:

$$\boldsymbol{A} = \frac{|n_-|\, M_-}{\rho_{0-}} \left[\left(w_{0-} - f_*^3 w_{0+}^* \right) \mathbf{1} + [\![\boldsymbol{F}^\top \cdot \boldsymbol{P}]\!] \right] + |n_*|\, M_* \mu_* \mathbf{1} \qquad (2.6.23)$$

where

$$w_{0-} \coloneqq \rho_{0-} f_- \,, \quad w_{0+} \coloneqq \rho_{0+}^* f_+ \qquad (2.6.24)$$

are the free energy densities (a.k.a. the stored energy densities) across the reaction front. This relation forms a basis for calculating the normal component A_{NN} to be used as the driving force in Eqn. (2.5.10). If we assume a perfect interface bond, *i.e.*, make use of kinematic compatibility conditions for a coherent interface in combination with the jump condition of the momentum balance the following expression can be derived (see [28] for details):[2]

$$A_{NN} = \frac{|n_-|\, M_-}{\rho_{0-}} \left(w_{0-} - f_*^3 w_{0+}^* + \boldsymbol{P}_- \cdot\!\!\cdot\, [\![\boldsymbol{F}]\!] + f_*^3 \frac{\rho_{0+}^*}{\rho_+} p_* \right) + |n_*|\, M_* \mu_*. \qquad (2.6.25)$$

2.6.5 Normal speed of the interface

We now return to Eqn. (2.5.10) and detail the normal speed, W_n, of an interface point. For this purpose we, first, note that it is customary to rewrite the forward reaction rate $\vec{\omega}$ as a product between the so-called kinetic constant, k, and the concentration, c. In other words, one separates $\vec{\omega}$ into its transport/flow properties, *i.e.*, k, and into the transported quantity, *i.e.*, the chemical mass involved, *i.e.*, c. However, because of the two reference configurations, the situation in our case is slightly convoluted and we must distinguish between:

$$\vec{\omega}_0 = k_0 c_0 \quad \text{and} \quad \vec{\omega}_0^* = k_0^* c_0^*. \qquad (2.6.26)$$

As far as the choice of indices is concerned the reader should observe the remarks in the footnote written in context with the definition of the various concentrations shown in Eqn. (2.6.15).

Now, if we observe the mass balances for singular interfaces with chemical production we may calculate two normal velocities associated with the virtual mappings, Γ and Γ^*, of the two reference configurations indicated by dashed lines in Fig. 2.5 (see [28] for details):

$$W^* = \frac{n_+ M_+}{\rho_{0+}^*} k_0^* c_0^* \left[1 - \exp\left(-\frac{A_{NN}}{RT} \right) \right] \approx \frac{n_+ M_+}{\rho_{0+}^*} k_0^* c_0^* \frac{A_{NN}}{RT}, \qquad (2.6.27)$$

$$W = \frac{|n_-|\, M_-}{\rho_{0-}} k_0 c_0 \left[1 - \exp\left(-\frac{A_{NN}}{RT} \right) \right] \approx \frac{|n_-|\, M_-}{\rho_{0-}} k_0 c_0 \frac{A_{NN}}{RT}.$$

Note that we have expressed W^* in terms of "+" and W in terms of "−" quantities as pertinent to the reference configurations, V^* and V, they serve.

---

[2]We denote by "$\cdot\!\!\cdot$" the outer double dot product, $\boldsymbol{A} \cdot\!\!\cdot\, \boldsymbol{B} \coloneqq A_{ij} B_{ij}$, and by ":" the inner double dot product, $\boldsymbol{A} : \boldsymbol{B} \coloneqq A_{ij} B_{ji}$.

2.6.6   Specialization to Hookean solids and ideal gases

Recall that the results so far hold for large deformations and for solids and gases of rather general constitutive form. We will now change this and specialize to linear Hookean solids and to ideal gases. Hence we may write:

$$w_{0-} \approx w_- = \eta_-(T) + \tfrac{1}{2}\boldsymbol{\epsilon}_-\!:\!\boldsymbol{\sigma}_-\,, \tag{2.6.28}$$

$$w_{0+} \approx w_+ = \eta_+(T) + \tfrac{1}{2}(\boldsymbol{\epsilon}_+ - \boldsymbol{\epsilon}^{\mathrm{ch}})\!:\!\boldsymbol{\sigma}_+,$$

where $\boldsymbol{\epsilon}^{\mathrm{ch}} = \epsilon^{\mathrm{ch}}\mathbf{1}$, $\epsilon^{\mathrm{ch}} = 0.03$ according to [28]. Moreover, $\eta_\pm(T)$ are the chemical parts of the free energy density of the "+" and of the "−" materials, respectively. More specifically, the Cauchy stresses, $\boldsymbol{\sigma}_\pm$, are related to the elastic strains via Hooke's law for isotropic materials:

$$\boldsymbol{\sigma}_+ = \boldsymbol{C}_+\!:\!(\boldsymbol{\epsilon}_+ - \boldsymbol{\epsilon}^{\mathrm{ch}}) \equiv \lambda_+\,\mathsf{Tr}\,\boldsymbol{\epsilon}_+\,\mathbf{1} + 2\mu_+\boldsymbol{\epsilon}_+ - 3k_+\epsilon^{\mathrm{ch}}\,\mathbf{1}, \tag{2.6.29}$$

$$\boldsymbol{\sigma}_- = \boldsymbol{C}_-\!:\!\boldsymbol{\epsilon}_- \equiv \lambda_-\,\mathsf{Tr}\,\boldsymbol{\epsilon}_-\,\mathbf{1} + 2\mu_-\boldsymbol{\epsilon}_-,$$

$C_\pm$ being the general stiffness tensors for anisotropic linear elastic media, $\lambda_\pm$ and $\mu_\pm$ referring to Lamé's constants, and $k_+ = \tfrac{1}{3}(3\lambda_+ + 2\mu_+)$ being the bulk modulus.

The molar chemical potential of a (single) ideal gas is given by:

$$M_*\mu_* \equiv M_*g_*(T,c) = \eta_*(T) + RT\ln\frac{c_0^*}{c_{0,\mathrm{ref}}^*} \equiv \eta_*(T) + RT\ln\frac{c_0}{c_{0,\mathrm{ref}}}, \tag{2.6.30}$$

where $g_*(T,c)$ is the specific Gibbs free energy in units of $^{\mathrm{kJ}}\!/_{\mathrm{kg}}$, $R = 8.314\frac{\mathrm{kJ}}{\mathrm{kmol\,K}}$ denotes the ideal gas constant, and $c_{0,\mathrm{ref}}^*$ and $c_{0,\mathrm{ref}}$ are reference concentrations pertinent to the two reference configurations, which have to be chosen suitably. One possible way (see [28]) is to identify them with the molar gas concentrations at the outer surface of the to-be-oxidized body. Moreover, since $g = u - Ts + ^p\!/_\rho$ (u, s, and p being the specific internal energy, entropy, and the (gas) pressure, respectively) we have for the molar chemical potential at the concentration $c_{0,\mathrm{ref}}^*$ [2] (see [60], pg. 141, 143, 316):

$$\eta_*(T) = \zeta RT + M_*u_{0,\mathrm{ref}}^* - M_*Ts_{0,\mathrm{ref}}^* - \zeta RT\ln\frac{T}{T_{0,\mathrm{ref}}^*} \equiv \tag{2.6.31}$$

$$(\zeta + 1)RT - \zeta RT\ln\frac{T}{T_{0,\mathrm{ref}}^*} - M_*Ts_{0,\mathrm{ref}}^*\,,\quad \zeta = \begin{cases} ^3\!/_2 & \text{monatomic} \\ ^5\!/_2 & \text{if biatomic} \\ 3 & \text{multiatomic} \end{cases} \text{gas.}$$

Note that in this equation we have chosen the symbol η even though it is not really a free energy density as in Eqns. (2.6.28).

---

[2]or at the concentration c_0; then, however, we must substitute the reference values for the specific internal energy, the entropy, and for the temperature by $u_{0,\mathrm{ref}}$, $s_{0,\mathrm{ref}}$, and $T_{0,\mathrm{ref}}$, respectively.

If we insert this into Eqn. (2.6.25) we arrive at the following expression for the normal component of the chemical potential tensor:

$$A_{NN} = \frac{|n_-| \, M_-}{\rho_{0-}} \left[\gamma(T) + \tfrac{1}{2}\boldsymbol{\epsilon}_- : \boldsymbol{\sigma}_- - \tfrac{1}{2} \left(\boldsymbol{\epsilon}_+ - \epsilon^{\text{ch}}\mathbf{1} \right) : \boldsymbol{\sigma}_+ + \sigma_- : [\![\boldsymbol{\epsilon}]\!] \right] + \qquad (2.6.32)$$

$$|n_*| \, RT \ln\frac{c_0}{c_{0,\text{ref}}},$$

where because of Eqn. (2.6.9)$_3$ we have defined:

$$\gamma(T) \coloneqq \eta_-(T) - f_*^3 \eta_+(T) + \frac{\rho_{0-}}{|n_-| \, M_-} |n_*| \eta_*. \qquad (2.6.33)$$

2.6.7 Equilibrium and diffusion

According to Eqns. (2.5.4), (2.5.8), and (2.5.11) the normal component of the chemical potential tensor assumes the following compact form:

$$A_{NN}\left(c_0^*\right) = |n_-| \, M_- \mu_- + |n_*| \, M_* \mu_*\left(c_0^*\right) - n_+ M_+ \mu_+. \qquad (2.6.34)$$

Note that we have explicitly indicated its dependence on gas concentration, which is exclusively given by the chemical potential of the gas constituent, $\mu_*\left(c_0^*\right)$. We may calculate the equilibrium concentration, $c_{0,\text{eq}}^*$, for a given state of stress by requiring:

$$A_{NN}\left(c_{0,\text{eq}}^*\right) \overset{!}{=} 0. \qquad (2.6.35)$$

If this condition is met the reaction front will stop moving, since equilibrium has been reached. However, independent of this relation, the concentrations, c, of the gas within the + region will develop according to a diffusion equation. The simplest one follows from a diffusion flux, $\boldsymbol{J}$, according to Fick's law:

$$\boldsymbol{J} = -D\nabla c, \qquad (2.6.36)$$

D being the diffusion constant. If we assume that D is truly a "constant" and if diffusion has reached a stationary state the governing equation is:

$$\frac{\partial c}{\partial t} + \nabla \cdot \boldsymbol{J} = 0 \quad \Rightarrow \quad \Delta c = 0, \qquad (2.6.37)$$

Note that Eqn. (2.6.36) is only the simplest form of a diffusion flux. In fact, the idea of the whole paper is that diffusion (and this includes the propagation of reaction fronts) is not only driven by spatial variations of concentration but also by mechanical stress. Hence, it seems natural to include stresses in a diffusion flux as well. In fact, we will do so later when we will discuss spinodal decomposition in tin-lead solders. However, in context with silicon oxidation we shall *not*, one reason for that being that the appropriate thermodynamics framework should be set up first.

The second order PDE (2.6.37) must still be complemented by two boundary conditions. We will get back to them shortly. In the meantime, note that we may write down Eqn. (2.6.34) twice, once for the equilibrium concentration, $c^*_{0,\mathrm{eq}}$, and once for the concentration c^*_{0,Γ^*} at the reaction front, Γ^* (say). If we subtract both results from each other, the terms containing stresses will cancel. Because of the equilibrium condition, Eqn. (2.6.35), we may then write:

$$A_{NN} = |n_*| M_* \left[\mu_* \left(c^*_{0,\Gamma^*} \right) - \mu_* \left(c^*_{0,\mathrm{eq}} \right) \right]. \qquad (2.6.38)$$

Now we argue that c^*_{0,Γ^*} and $c^*_{0,\mathrm{eq}}$ are not far apart, in other words the whole oxidation process is always close to equilibrium. This allows us to expand the first term in the parentheses of Eqn. (2.6.38) into a Taylor series around $c^*_{0,\mathrm{eq}}$ leading to:

$$A_{NN} = |n_*| M_* \left. \frac{\partial \mu_*}{\partial c} \right|_{c^*_{0,\mathrm{eq}}} \left(c^*_{0,\Gamma^*} - c^*_{0,\mathrm{eq}} \right). \qquad (2.6.39)$$

If we now use the explicit form of the chemical potential of an ideal gas shown in Eqn. (2.6.30) we arrive at:

$$\frac{A_{NN}}{RT} = |n_*| \frac{c^*_{0,\Gamma^*} - c^*_{0,\mathrm{eq}}}{c^*_{0,\mathrm{eq}}} \approx |n_*| \frac{c^*_{0,\Gamma^*} - c^*_{0,\mathrm{eq}}}{c^*_{0,\Gamma^*}}. \qquad (2.6.40)$$

This is a good form to be used for computing the interface speed according to Eqn. (2.6.27)$_1$, when evaluated for $c^*_0 \equiv c^*_{0,\Gamma^*}$:

$$W^* = \frac{n_+ M_+}{\rho^*_{0+}} k^*_0 |n_*| \left(c^*_{0,\Gamma^*} - c^*_{0,\mathrm{eq}} \right). \qquad (2.6.41)$$

Note that the same line of reasoning applies to the interface image Γ of the "−" reference configuration and Eqn. (2.6.27)$_2$ then becomes:

$$W = \frac{|n_-| M_-}{\rho_{0-}} k_0 |n_*| \left(c_{0,\Gamma} - c_{0,\mathrm{eq}} \right). \qquad (2.6.42)$$

Eqns. (2.6.40)-(2.6.42) deserve a discussion. For a progressing oxidation it is obviously necessary that $W^* > 0$ or $W > 0$. Moreover, in view of the dissipation inequality, Eqn. (2.5.9), it is then also required that $A_{NN} > 0$. Both is guaranteed if $c^*_{0,\Gamma^*} - c^*_{0,\mathrm{eq}} > 0 \Rightarrow c^*_{0,\Gamma^*} > c^*_{0,\mathrm{eq}}$ or $c_{0,\Gamma} - c_{0,\mathrm{eq}} > 0 \Rightarrow c_{0,\Gamma} > c_{0,\mathrm{eq}}$. If these inequalities are not fulfilled the oxidation will stagnate (for the case of equilibrium where equality between the interface and the equilibrium concentrations holds) or even locked (for the case when the interface concentration is smaller than the equilibrium concentration). Moreover, in view of Fick's law (2.6.36) it seems obvious that diffusion will only take place if there is a gradient between the concentrations c^*_{0,A^*_+} or c_{0,A_+} on the surfaces, A^*_+ or A_+, of the two reference configurations and the concentrations, c^*_{0,Γ^*} or

$c_{0,\Gamma}$, right at the interface, Γ^* or Γ. Hence the following chain of inequalities must hold in order to prevent interface locking:

$$c^*_{0,A^*_+} > c^*_{0,\Gamma^*} > c^*_{0,\text{eq}} \ , \quad c_{0,A_+} > c_{0,\Gamma} > c_{0,\text{eq}}. \tag{2.6.43}$$

After the appropriate nomenclature has been established we now turn to the two boundary conditions required for a unique solution of the diffusion equation Eqn. $(2.6.37)_2$. They read:

$$c^*_0\big|_{A^*_+} = c^*_{0,A^*_+} \ , \quad D\,\frac{\partial c^*}{\partial N^*}\bigg|_{\Gamma^*} = -n^2_* k^*_0\left(c^*_{0,\Gamma^*} - c^*_{0,\text{eq}}\right), \tag{2.6.44}$$

$$c_0\big|_{A_+} = c_{0,A_+} \ , \quad D\,\frac{\partial c}{\partial N}c\bigg|_{\Gamma} = -n^2_* k_0\left(c_{0,\Gamma} - c_{0,\text{eq}}\right).$$

The latter is a consequence of the mass balance at singular surfaces into which the expressions (2.6.41) or (2.6.42) for the approximate relation for the normal velocities have been inserted. However, they can also be interpreted intuitively: The more the concentration at the interface departs from the equilibrium concentration the greater the mass flux[2] normal to the interface will be. The negative sign makes sense in view of Eqn. (2.6.42).

2.7 Case study – A two-dimensional planar reaction front

2.7.1 Problem description

We consider the situation depicted in Fig. 2.6 (also see [30]: Two blocks of solids, "+" and "−," are separated by a planar reaction front, γ. Block "+" consists of a SiO_2 skeleton infiltrated by oxygen, "$*$," and block "−" is made of unreacted Si. Due to the reaction a change in volume occurs within "+," which already results in strains and stresses in both regions. In addition, it is possible to prescribe either displacements or stresses on the faces perpendicular to the reaction front. The objective is, first, to calculate the state of deformation and, second, to use this information to predict the temporal development of the reaction front, *i.e.*, to predict its height as a function of time, $h(t)$.

2.7.2 Solution of the elasticity problem for prescribed displacements

The solution we seek must fulfill several restraints on the various boundaries and along the interface. First, we require that the faces perpendicular to the

---

[2]Note that the normal derivative is calculated by $\partial c/\partial N = \nabla_{\boldsymbol{x}} \cdot \boldsymbol{N}$ and *vice versa* for the "+" reference configuration.
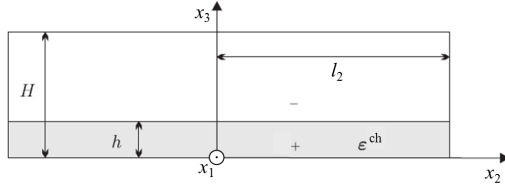
Figure 2.6: Geometry of the planar reaction front.

interface stay perpendicular, which means that only the following (prescribed) components of the displacement vector are different from zero:

$$u_1^{\pm}\left(x_1 = \pm l_1, \ x_2 \in (-l_2, l_2), \ x_3 \in \left\{ \begin{array}{l} (0, h) \text{ for } + \\ (h, H) \text{ for } - \end{array} \right. \right) \stackrel{!}{=} u_1^0, \qquad (2.7.1)$$

$$u_2^{\pm}\left(x_1 \in (-l_1, l_1), \ x_2 = \pm l_2, \ x_3 \in \left\{ \begin{array}{l} (0, h) \text{ for } + \\ (h, H) \text{ for } - \end{array} \right. \right) \stackrel{!}{=} u_2^0.$$

Second, the bottom and the top of the system are free of tractions, which means:

$$\sigma_{13/23/33}^{+}\left(x_1 \in (-l_1, l_1), \ x_2 \in (-l_2, l_2), \ x_3 = 0\right) = 0, \qquad (2.7.2)$$

and

$$\sigma_{13/23/33}^{-}\left(x_1 \in (-l_1, l_1), \ x_2 \in (-l_2, l_2), \ x_3 = H\right) = 0. \qquad (2.7.3)$$

Third, the traction vector must be continuous at the interface:

$$\sigma_{13/23/33}^{+}\left(x_1 \in (-l_1, l_1), \ x_2 \in (-l_2, l_2), \ x_3 = h\right) = \qquad (2.7.4)$$
$$\sigma_{13/23/33}^{-}\left(x_1 \in (-l_1, l_1), \ x_2 \in (-l_2, l_2), \ x_3 = h\right).$$

Fourth, coherency conditions apply at the interface:

$$\epsilon_{11/12/13/22/23}^{+}\left(x_1 \in (-l_1, l_1), \ x_2 \in (-l_2, l_2), \ x_3 = h\right) = \qquad (2.7.5)$$
$$\epsilon_{11/12/13/22/23}^{-}\left(x_1 \in (-l_1, l_1), \ x_2 \in (-l_2, l_2), \ x_3 = h\right).$$

Fifth, we require the following symmetry conditions for the displacements to hold:

$$u_1^{\pm}\left(x_1 = 0, x_2, x_3\right) = 0 \ , \ \ u_2^{\pm}\left(x_1, x_2 = 0, x_3\right) = 0 \qquad (2.7.6)$$

as well as prevention of rigid-body translation and continuity at the interface:

$$u_3^{+}\left(x_1, x_2, x_3 = 0\right) = 0, \ \ u_i^{+}\left(x_1, x_2, x_3 = h\right) = u_i^{-}\left(x_1, x_2, x_3 = h\right), \ \ i \in 1, 2, 3. \ \ (2.7.7)$$

If we now combine the equations of static equilibrium:

$$\frac{\partial \sigma_{ji}^{+}}{\partial x_j} = 0 \qquad (2.7.8)$$

with Hooke's law from Eqns. (2.6.29) we arrive at the Lamé-Navier equations:

$$(\lambda^\pm + \mu^\pm) \frac{\partial^2 u_k^\pm}{\partial x_i \partial x_k} + \mu_\pm \frac{\partial^2 u_i^\pm}{\partial x_k \partial x_k} = 0. \tag{2.7.9}$$

We now attempt to solve them by the following semiinverse *ansatz*:

$$u_1^\pm = u_1^\pm(x_1) \ , \ \ u_2^\pm = u_2^\pm(x_2) \ , \ \ u_3^\pm = u_3^\pm(x_3) \tag{2.7.10}$$

and find:

$$u_1^\pm = A_1^\pm x_1 + B_1^\pm \ , \ \ u_2^\pm = A_2^\pm x_2 + B_2^\pm \ , \ \ u_3^\pm = A_3^\pm x_3 + B_3^\pm. \tag{2.7.11}$$

Thus, twelve constants need to be determined. From the displacement conditions Eqns. (2.7.6) (2.7.7) we conclude that:

$$B_1^\pm = 0 \ , \ \ B_2^\pm = 0 \ , \ \ B_3^+ = 0 \ , \ \ B_3^- = \left(A_3^+ - A_3^-\right) h. \tag{2.7.12}$$

Moreover, Eqns. (2.7.1) (2.7.2) yield:

$$A_1^\pm = \frac{u_1^0}{l_1} =: \epsilon_{11}^0 \ , \ \ A_2^\pm = \frac{u_2^0}{l_2} =: \epsilon_{22}^0. \tag{2.7.13}$$

We now observe Hooke's law, Eqns. (2.6.29). Then the normal stress components in Eqns. (2.7.3) lead to:

$$A_3^+ = -\frac{\lambda_+}{\lambda_+ + 2\mu_+} \left(\epsilon_{11}^0 + \epsilon_{22}^0\right) + \frac{3k_+}{\lambda_+ + 2\mu_+} \epsilon^{\text{ch}} \ , \ \ A_3^- = -\frac{\lambda_-}{\lambda_- + 2\mu_-} \left(\epsilon_{11}^0 + \epsilon_{22}^0\right), \tag{2.7.14}$$

whereas the shear components in that equation are identically satisfied. By observing the results obtained so far, it turns out that all of the continuity conditions for the stresses at the interface, Eqns. (2.7.4), are also identically satisfied. The same holds for the coherency conditions, Eqns. (2.7.5). Finally by inserting Eqns. (2.7.14) into Eqns. (2.7.12)$_3$ we find:

$$B_3^- = -\left(\frac{\lambda_+}{\lambda_+ + 2\mu_+} + \frac{\lambda_-}{\lambda_- + 2\mu_-}\right)\left(\epsilon_{11}^0 + \epsilon_{22}^0\right) h + \frac{3k_+}{\lambda_+ + 2\mu_+} \epsilon^{\text{ch}} h. \tag{2.7.15}$$

In summary we obtain the following final results, (a) for the displacements:

$$u_1^\pm = \epsilon_{11}^0 x_1, \ u_2^\pm = \epsilon_{22}^0 x_2, \ u_3^+ = \left[-\frac{\lambda_+}{\lambda_+ + 2\mu_+} \left(\epsilon_{11}^0 + \epsilon_{22}^0\right) + \frac{3k_+}{\lambda_+ + 2\mu_+} \epsilon^{\text{ch}}\right] x_3, \tag{2.7.16}$$

$$u_3^- = -\left[\frac{\lambda_+}{\lambda_+ + 2\mu_+} - \frac{\lambda_-}{\lambda_- + 2\mu_-} \left(1 - \frac{x_3}{h}\right)\right]\left(\epsilon_{11}^0 + \epsilon_{22}^0\right) h + \frac{3k_+}{\lambda_+ + 2\mu_+} \epsilon^{\text{ch}} h \ ,$$

(b) for the strains:

$$\epsilon_{11}^\pm = \epsilon_{11}^0 \ , \ \ \epsilon_{22}^\pm = \epsilon_{22}^0 \ , \ \ \epsilon_{33}^+ = -\frac{\lambda_+}{\lambda_+ + 2\mu_+} \left(\epsilon_{11}^0 + \epsilon_{22}^0\right) + \frac{3k_+}{\lambda_+ + 2\mu_+} \epsilon^{\text{ch}} \ , \tag{2.7.17}$$

$$\epsilon_{33}^- = -\frac{\lambda_-}{\lambda_- + 2\mu_-}\left(\epsilon_{11}^0 + \epsilon_{22}^0\right) \;, \;\; \epsilon_{12}^\pm = \epsilon_{13}^\pm = \epsilon_{23}^\pm = 0 \;,$$

and (c) for the stresses:

$$\sigma_{11}^+ = \frac{2\lambda_+\mu_+}{\lambda_+ + 2\mu_+}\left(\epsilon_{11}^0 + \epsilon_{22}^0\right) + 2\mu_+\epsilon_{11}^0 - \frac{3k_+2\mu_+}{\lambda_+ + 2\mu_+}\epsilon^{\mathrm{ch}} \;, \tag{2.7.18}$$

$$\sigma_{22}^+ = \frac{2\lambda_+\mu_+}{\lambda_+ + 2\mu_+}\left(\epsilon_{11}^0 + \epsilon_{22}^0\right) + 2\mu_+\epsilon_{22}^0 - \frac{3k_+2\mu_+}{\lambda_+ + 2\mu_+}\epsilon^{\mathrm{ch}} \;,$$

$$\sigma_{11}^- = \frac{2\lambda_-\mu_-}{\lambda_- + 2\mu_-}\left(\epsilon_{11}^0 + \epsilon_{22}^0\right) + 2\mu_-\epsilon_{11}^0 \;, \;\; \sigma_{22}^- = \frac{2\lambda_-\mu_-}{\lambda_- + 2\mu_-}\left(\epsilon_{11}^0 + \epsilon_{22}^0\right) + 2\mu_-\epsilon_{22}^0 \;,$$

$$\sigma_{33}^\pm = \sigma_{12}^\pm = \sigma_{13}^\pm = \sigma_{23}^\pm = 0 \;,$$

Note that if we specialize these results to the two-dimensional case, *e.g.*, by putting $\epsilon_{22}^0 = 0$, we almost arrive at the results presented in [28], pg. 65. The agreement is perfect if we take the transition from 3D to 2D into account and substitute $3k \to 2(\lambda + \mu)$.

2.7.3 Solution of the elasticity problem for prescribed stresses

We now replace the prescribed displacements of Eqn. (2.7.1) by prescribed normal stresses:

$$\sigma_{11}^\pm\left(x_1 = \pm l_1, \; x_2 \in (-l_2, l_2), \; x_3 \in \left\{\begin{array}{l} (0, h) \text{ for } + \\ (h, H) \text{ for } - \end{array}\right. \right) \stackrel{!}{=} \sigma_{11}^0, \tag{2.7.19}$$

$$\sigma_{22}^\pm\left(x_1 \in (-l_1, l_1), \; x_2 = \pm l_2, \; x_3 \in \left\{\begin{array}{l} (0, h) \text{ for } + \\ (h, H) \text{ for } - \end{array}\right. \right) \stackrel{!}{=} \sigma_{22}^0.$$

Following [28], pg. 67 we choose the following semiinverse *ansatz* for the strains:

$$\epsilon_{11}^\pm = A_1^\pm x_3 + B_1^\pm \;, \;\; \epsilon_{22}^\pm = A_2^\pm x_3 + B_2^\pm, \tag{2.7.20}$$

where $A_{1/2}^\pm$ and $B_{1/2}^\pm$ are constants. This means that the displacements read:

$$u_1^\pm = A_1^\pm x_3 x_1 + B_1^\pm x_3 + C_1^\pm(x_2, x_3) \;, \;\; u_2^\pm = A_2^\pm x_3 x_2 + B_2^\pm x_2 + C_2^\pm(x_1, x_3), \tag{2.7.21}$$

where $C_1^\pm(x_2, x_3)$ and $C_2^\pm(x_1, x_3)$ are functions of the indicated coordinates. However, due to the symmetry conditions(2.7.6) we find that they have to vanish identically, so that:

$$u_1^\pm = A_1^\pm x_3 x_1 + B_1^\pm x_3 \;, \;\; u_2^\pm = A_2^\pm x_3 x_2 + B_2^\pm x_2. \tag{2.7.22}$$

Motivated by the fact that the top and bottom surfaces of the block are free of tractions we now require in addition to the boundary conditions established in the previous section that:

$$\sigma_{13}^\pm \stackrel{!}{=} 0 \;, \;\; \sigma_{23}^\pm \stackrel{!}{=} 0. \tag{2.7.23}$$

In combination with Hooke's law (2.6.29) and the results (2.7.22) this leads to:

$$u_3^\pm = -\tfrac{1}{2} A_1^\pm x_1^2 + C_3^\pm(x_2, x_3) \quad \Rightarrow \quad \epsilon_{33}^\pm = \frac{\partial C_3^\pm(x_2, x_3)}{\partial x_3}, \tag{2.7.24}$$

$$u_3^\pm = -\tfrac{1}{2} A_2^\pm x_2^2 + D_3^\pm(x_1, x_3) \quad \Rightarrow \quad \epsilon_{33}^\pm = \frac{\partial D_3^\pm(x_1, x_3)}{\partial x_3},$$

where $C_3^\pm(x_2, x_3)$ and $D_3^\pm(x_1, x_3)$ are functions of the indicated coordinates. Differentiation of $u_3^\pm$ w.r.t. x_2 and x_1 yields:

$$C_3^\pm(x_2, x_3) = -\tfrac{1}{2} A_1^\pm x_2^2 + f^\pm(x_3) \,, \quad D_3^\pm(x_1, x_3) = -\tfrac{1}{2} A_1^\pm x_1^2 + g^\pm(x_3), \tag{2.7.25}$$

where $f^\pm(x_3)$ and $g^\pm(x_3)$ are functions of the indicated coordinate. However, after insertion into Eqn. (2.7.1) we must conclude that $f^\pm(x_3) \equiv g^\pm(x_3)$ and so:

$$u_3^\pm = -\tfrac{1}{2} A_1^\pm x_1^2 - \tfrac{1}{2} A_2^\pm x_2^2 + f^\pm(x_3), \tag{2.7.26}$$

We now turn to the continuity conditions Eqn. $(2.7.7)_2$ to find for $i = 3$:

$$f_3^+(h) = f_3^-(h) \,, \quad A_1^+ = A_1^- =: A_1 \,, \quad A_2^+ = A_2^- =: A_2, \tag{2.7.27}$$

whereas $i = 1$ and $i = 2$ yield:

$$B_1^+ = B_1^- =: B_1 \,, \quad B_2^+ = B_2^- =: B_2, \tag{2.7.28}$$

Thus, as an intermediate result, we note for the displacements:

$$u_1 := u_1^+ \equiv u_1^- = A_1 x_3 x_1 + B_1 x_1 \,, \quad u_2 := u_2^+ \equiv u_2^- = A_2 x_3 x_2 + B_2 x_2, \tag{2.7.29}$$

$$u_3^\pm = -\tfrac{1}{2} A_1 x_1^2 - \tfrac{1}{2} A_2 x_2^2 + f^\pm(x_3),$$

and hence for the strains:

$$\epsilon_{11} := \epsilon_{11}^+ \equiv \epsilon_{11}^- = A_1 x_3 + B_1 \,, \quad \epsilon_{22} := \epsilon_{22} \equiv \epsilon_{22} = A_2 x_3 + B_2, \tag{2.7.30}$$

$$\epsilon_{33}^\pm = -\frac{\mathrm{d} f^\pm}{\mathrm{d} x_3} \,, \quad \epsilon_{12} := \epsilon_{12}^+ \equiv \epsilon_{12}^- = 0 \,, \quad \epsilon_{13} := \epsilon_{13}^+ \equiv \epsilon_{13}^- = 0 \,, \quad \epsilon_{23} := \epsilon_{23}^+ \equiv \epsilon_{23}^- = 0.$$

Again, motivated by the fact that the top and bottom surfaces of the block are free of tractions we now require that the corresponding normal stresses vanish throughout:

$$\sigma_{33}^+ \overset{!}{=} 0 \,, \quad \sigma_{33}^- \overset{!}{=} 0. \tag{2.7.31}$$

By using Hooke's law (2.6.29) and the previous results we find for the missing strain components:

$$\epsilon_{33}^+ \equiv \frac{\mathrm{d} f^+}{\mathrm{d} x_3} = -\frac{\nu_+}{1 - \nu_+} \left[(A_1 + A_2) x_3 + B_1 + B_2 \right] + \frac{1 + \nu_+}{1 - \nu_+} \epsilon^{\mathrm{ch}}, \tag{2.7.32}$$

$$\epsilon_{33}^- \equiv \frac{\mathrm{d} f^-}{\mathrm{d} x_3} = -\frac{\nu_-}{1 - \nu_-} \left[(A_1 + A_2) x_3 + B_1 + B_2 \right],$$

and for the normal stresses:

$$\sigma_{11}^+ \equiv \frac{E_+}{1-\nu_+^2}\left[(A_1 + \nu_+ A_2)\,x_3 + B_1 + \nu_+ B_2\right] - \frac{E_+}{1-\nu_+}\epsilon^{\text{ch}},$$

$$\sigma_{11}^- \equiv \frac{E_-}{1-\nu_-^2}\left[(A_1 + \nu_- A_2)\,x_3 + B_1 + \nu_- B_2\right], \tag{2.7.33}$$

$$\sigma_{22}^+ \equiv \frac{E_+}{1-\nu_+^2}\left[(\nu_+ A_1 + A_2)\,x_3 + \nu_+ B_1 + B_2\right] - \frac{E_+}{1-\nu_+}\epsilon^{\text{ch}},$$

$$\sigma_{22}^- \equiv \frac{E_-}{1-\nu_-^2}\left[(\nu_- A_1 + A_2)\,x_3 + \nu_- B_1 + B_2\right].$$

Note that because of Hooke's law and Eqn. $(2.7.30)_{4-6}$ we have:

$$\sigma_{12}^\pm = 0\,,\quad \sigma_{13}^\pm = 0\,,\quad \sigma_{23}^\pm = 0. \tag{2.7.34}$$

Hence it is now fully guaranteed that the top and the bottom of the block are free of tractions.

Inspection of Eqns. $(2.7.30)_1$ and $(2.7.33)$ shows that four constants remain to be determined, $A_{1,2}$ and $B_{1,2}$, respectively. They can be obtained from the equations for equilibrium of forces:

$$\int_{x_3=0}^{H} \sigma_{11}^0 \mathrm{d}x_3 = \int_{x_3=0}^{h} \sigma_{11}^+\big|_{x_1=l_1} \mathrm{d}x_3 + \int_{x_3=h}^{H} \sigma_{11}^-\big|_{x_1=l_1} \mathrm{d}x_3, \tag{2.7.35}$$

$$\int_{x_3=0}^{H} \sigma_{22}^0 \mathrm{d}x_3 = \int_{x_3=0}^{h} \sigma_{22}^+\big|_{x_2=l_2} \mathrm{d}x_3 + \int_{x_3=h}^{H} \sigma_{22}^+\big|_{x_2=l_2} \mathrm{d}x_3,$$

and equilibrium of moments (w.r.t. $\boldsymbol{x} = \boldsymbol{0}$):

$$\int_{x_3=0}^{H} x_3\sigma_{11}^0 \mathrm{d}x_3 = \int_{x_3=0}^{h} x_3\sigma_{11}^+\big|_{x_1=l_1} \mathrm{d}x_3 + \int_{x_3=h}^{H} x_3\sigma_{11}^-\big|_{x_1=l_1} \mathrm{d}x_3, \tag{2.7.36}$$

$$\int_{x_3=0}^{H} x_3\sigma_{22}^0 \mathrm{d}x_3 = \int_{x_3=0}^{h} x_3\sigma_{22}^+\big|_{x_2=l_2} \mathrm{d}x_3 + \int_{x_3=h}^{H} x_3\sigma_{22}^+\big|_{x_2=l_2} \mathrm{d}x_3.$$

It is advisable to integrate these relations and then rewrite them in dimensionless form:

$$\tfrac{1}{2}\left(\bar{A}_1 + \nu_+ \bar{A}_2\right)\xi^2 + \left(B_1 + \nu_+ B_2\right)\xi - (1 + \nu_+)\,\epsilon^{\text{ch}}\xi +$$

$$\alpha\left[\tfrac{1}{2}\left(\bar{A}_1 + \nu_- \bar{A}_2\right)\left(1 - \xi^2\right) + \left(B_1 + \nu_- B_2\right)\left(1 - \xi\right)\right] = \bar{\sigma}_{11}^0,$$

$$\tfrac{2}{3}\left(\bar{A}_1 + \nu_+ \bar{A}_2\right)\xi^3 + \left(B_1 + \nu_+ B_2\right)\xi^2 - (1 + \nu_+)\,\epsilon^{\text{ch}}\xi^2 + \tag{2.7.37}$$

$$\alpha\left[\tfrac{2}{3}\left(\bar{A}_1 + \nu_- \bar{A}_2\right)\left(1 - \xi^3\right) + \left(B_1 + \nu_- B_2\right)\left(1 - \xi^2\right)\right] = \bar{\sigma}_{11}^0,$$

$$\tfrac{1}{2}\left(\nu_+ \bar{A}_1 + \bar{A}_2\right)\xi^2 + \left(\nu_+ B_1 + B_2\right)\xi - (1 + \nu_+)\,\epsilon^{\text{ch}}\xi +$$

$$\alpha \left[\tfrac{1}{2} \left(\nu_- \bar{A}_1 + \bar{A}_2 \right) \left(1 - \xi^2 \right) + \left(\nu_- B_1 + B_2 \right) \left(1 - \xi \right) \right] = \bar{\sigma}_{22}^0,$$

$$\tfrac{2}{3} \left(\nu_+ \bar{A}_1 + \bar{A}_2 \right) \xi^3 + \left(\nu_+ B_1 + B_2 \right) \xi^2 - \left(1 + \nu_+ \right) \epsilon^{\mathrm{ch}} \xi^2 +$$

$$\alpha \left[\tfrac{2}{3} \left(\nu_- \bar{A}_1 + \bar{A}_2 \right) \left(1 - \xi^3 \right) + \left(\nu_- B_1 + B_2 \right) \left(1 - \xi^2 \right) \right] = \bar{\sigma}_{22}^0,$$

where:

$$\bar{\sigma}_{11/22}^0 = \frac{\sigma_{11/22}^0}{E_+ / 1 - \nu_+^2} \ , \quad \xi = \frac{h}{H} \ , \quad \bar{A}_{1/2} = A_{1/2} H \ , \quad \alpha = \frac{E_-}{E_+} \frac{1 - \nu_+^2}{1 - \nu_-^2}. \tag{2.7.38}$$

2.7.4 Solution of the diffusion problem

We assume that the concentration of the gas component is only a function of x_3 and that stationary conditions have been reached. Then Fick's first and second law, Eqns. (2.7.36) and (2.7.37) degenerate to:

$$\frac{\partial^2 c}{\partial x_3^2} = 0 \quad \Rightarrow \quad c = A x_3 + B, \tag{2.7.39}$$

The two constants of integration, A and B, can be determined from the boundary conditions shown in Eqns. (2.6.44). We rewrite them slightly, because in our current small strain investigation it is not necessary to distinguish between the current and reference configurations:

$$c(x_3 = 0) = c_0 \ , \quad D \left. \frac{\mathrm{d}c}{\mathrm{d}x_3} \right|_{x_3 = h} = -n_*^2 k_0 \left(c(h) - c_{\mathrm{eq}} \right). \tag{2.7.40}$$

Hence we find that:

$$c(x_3) = \frac{n_*^2 k_0 \left(c_{\mathrm{eq}} - c_0 \right)}{D + n_*^2 k_0 h} \frac{x_3}{h} + c_0. \tag{2.7.41}$$

and obtain for the concentration at the interface:

$$c(h) = \frac{c_0 + c_{\mathrm{eq}} \kappa \, \xi}{1 + \kappa \, \xi} \ , \quad \kappa = \frac{n_*^2 k_0 H}{D} \ , \quad \xi = \frac{h}{H}. \tag{2.7.42}$$

If we insert this result into Eqn. (2.7.42) we obtain for the interface velocity:

$$W \equiv H \frac{\mathrm{d}\xi}{\mathrm{d}t} = \frac{|n_-| M_-}{\rho_{0-}} \frac{k_0 |n_*| c_0}{1 + \kappa \xi} \left(1 - \frac{c_{\mathrm{eq}}}{c_0} \right). \tag{2.7.43}$$

We define a dimensionless time by:

$$\bar{t} := \frac{|n_-| M_-}{H \rho_{0-}} k_0 |n_*| c_0 t \tag{2.7.44}$$

and integrate the differential equation (2.7.43):

$$\xi + \kappa \frac{\xi^2}{2} = \left(1 - \frac{c_{\text{eq}}}{c_0}\right)\bar{t} \quad \Rightarrow \quad \xi = -\frac{1}{\kappa} + \frac{1}{\kappa}\sqrt{1 + 2\kappa\left(1 - \frac{c_{\text{eq}}}{c_0}\right)\bar{t}}, \qquad (2.7.45)$$

if the initial conditions $\xi = 0$ for $\bar{t} = 0$ are used, unphysical relations for ξ are ignored, and, most importantly, c_{eq}/c_0 does not depend on ξ. As we shall see, the latter is the case if we prescribe displacements. If stresses are applied on the boundaries, a numerical solution is required, since in that case c_{eq}/c_0 depends on the height ξ of the reaction front in a complicated manner. This is the famous parabolic growth law often encountered in context with diffusion-controlled growth processes and, in particular, for the case of silicon oxidation (see [17] or [42]). Note that Kao *et al.* [42] criticize using such a relationship in context with silicon oxidation. However, their idea is to relate the departure from the parabolic law to a geometric effect, and they demonstrate it by studying cylindrical structures. We could have done this as well, but there is another effect that brings in nonlinearity in ξ: The concentration c_{eq} depends on it as well, because it is governed by the equilibrium relation (2.6.36) into which the stresses enter (*cf*, Eqns. (2.6.32) and (2.6.32)), and the stresses are complex functions of ξ, at least if we prescribe external stresses (*cf.*, Eqn. (2.6.37)).

Nevertheless, if we turn to the case of prescribed displacements, there is an effect of the stresses on the equilibrium concentration as well, although it is independent on ξ. However, the advantage of this case is that the relation for equilibrium concentration, c_{eq}, can be written down in a relatively concise form. We start from Eqn. (2.6.32), observe Eqn. (2.6.35), and insert Eqns. (2.7.17) and (2.7.18) to find:

$$\frac{\gamma(T)}{\gamma_*} + \frac{1}{2}\left[\left(\frac{E_-}{E_+}\frac{1-\nu_+}{1-\nu_-^2} - \frac{1}{1+\nu_+}\right)\frac{\epsilon_{11}^0{}^2 + \epsilon_{22}^0{}^2}{\epsilon^{\text{ch}\,2}} + 2\left(\frac{E_-}{E_+}\frac{\nu_- (1-\nu_+)}{1-\nu_-^2} - \frac{\nu_+}{1+\nu_+}\right)\frac{\epsilon_{11}^0 \epsilon_{22}^0}{\epsilon^{\text{ch}\,2}} + \right.$$

$$\left. 2\frac{\epsilon_{11}^0 + \epsilon_{22}^0}{\epsilon^{\text{ch}}} - 2\right] = -\frac{|n_*|}{|n_-|}\frac{RT\rho_{0-}}{M_-\gamma_*}\ln\frac{c_{\text{eq}}}{c_0} \;,\;\; \gamma_* = \frac{E_+}{1-\nu_+}\epsilon^{\text{ch}\,2}. \qquad (2.7.46)$$

Also recall that for a moving interface we must have (*cf.*, Eqn. (2.6.43)):

$$c_0 > c(h) > c_{\text{eq}}. \qquad (2.7.47)$$

2.7.5 Materials data

Following [28] the data compiled in Table 2.1 has been used for numerical analysis. Moreover, we also choose $\epsilon^{\text{ch}} = 0.03$ and assume that at $x_3 = 0$ the oxygen concentration is always at the saturated level, *i.e.*, $c_0 = 8.6 \times 10^{-5}\frac{\text{kmol}}{\text{m}^3}$ for dry oxidation at $T = 1000°$C (*cf.*, Deal and Grove [17], pg. 3776[2]). Temperature

---

[2]Actually, Deal and Grove provide the saturation level in units of particle density, $c_0 = 5.2 \times 10^{16}\frac{1}{\text{cm}^3}$. Avogadro's constant has to be used to convert it into molar units.

dependent values for the diffusion and for the reaction constants, D_0 and k_0, respectively, were also based on the paper by Dell and Grove. However, that paper does not provide information on diffusion and reaction coefficients directly. A conversion is required based on the following formulae:

$$D_0(T) = \frac{N_1}{2c_0}B \ , \quad k_0(T) = \frac{2D_0}{A}. \tag{2.7.48}$$

For dry oxidation the temperature dependent "constants" A and B can be found in Deal and Grove's paper on pg. 3775. Moreover, $N_1 = 2.25 \times 10^{22} \mathrm{cm}^{-3}$, pg. 3775, *ibid.* The result is shown in Fig. 2.7. The curves are spline interpolations between the data analyzed by Deal and Grove.

Table 2.1: Material parameters used during numerical analysis.

Parameter	Constituent $B_- \equiv \mathrm{Si}$	Constituent $B_+ \equiv \mathrm{SiO}_2$
Young's modulus, $E[\mathrm{GPa}]$	163	60
Poisson's ratio, $\nu[-]$	0.23	0.17
mass densities, $\rho_0\left[\frac{\mathrm{kg}}{\mathrm{m}^3}\right]$	2328	2199
molar masses, $M\left[\frac{\mathrm{kg}}{\mathrm{kmol}}\right]$	28.084	60.082
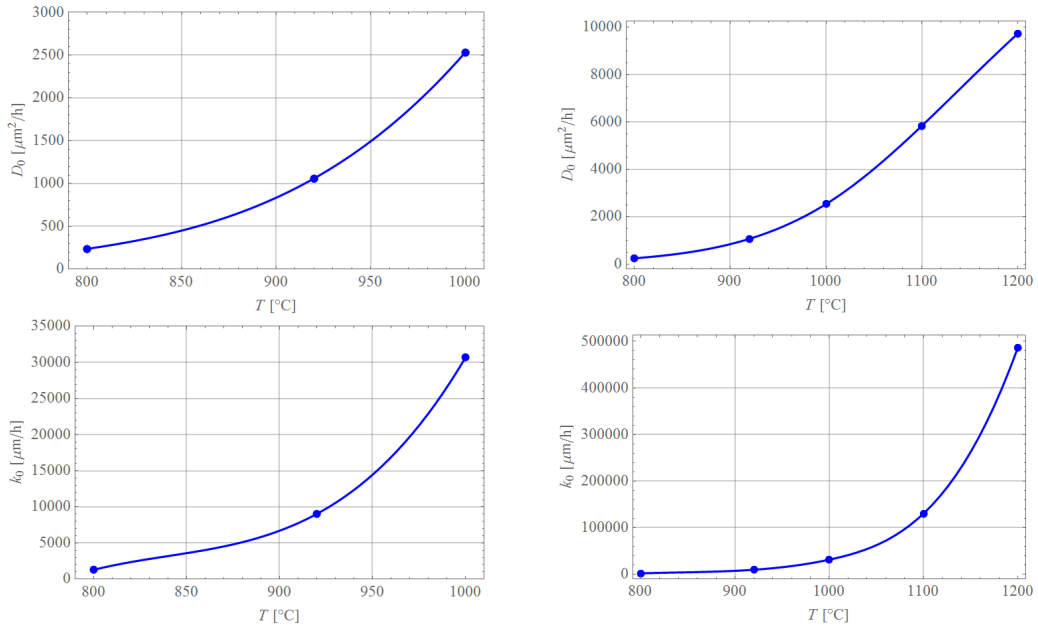
Figure 2.7: Diffusion and reaction constants predicted acc. to Deal and Grove [17].

At this point various remarks are in order. First, the plots were generated by using the same value for c_0 even though, in principle, it should vary with

temperature. However, Deal and Grove conclude on pg. 3776 that "similar values of $C^*[\equiv c_0]$ would be obtained at any other temperature within the experimental range. Such a conclusion is substantiated by Moulson and Roberts, who found an essentially constant solubility of water in fused silica between 900° and 1200°C." Second, other sources quote totally different values for the diffusion and the reaction constant. For example Lin [46] states on pg. 11 of his thesis that $D_0 = 66\frac{\mu m^2}{h}$ and $k_0 = 90\frac{\mu m}{h}$, while referring to Deal and Grove. This would correspond to a temperature below $T = 800$°C, which is not realistic for oxidation on an industrial scale. Moreover, Rao *et al.* [72] use $D_0 = 496296\frac{\mu m^2}{h}$ and $k_0 = -283507\frac{\mu m}{h}$ on pg. 374 of their simulations without providing a reference. In any case, they seem to operate at temperatures higher than $T = 1200$°C. The minus sign in the reaction constant remains unexplained.
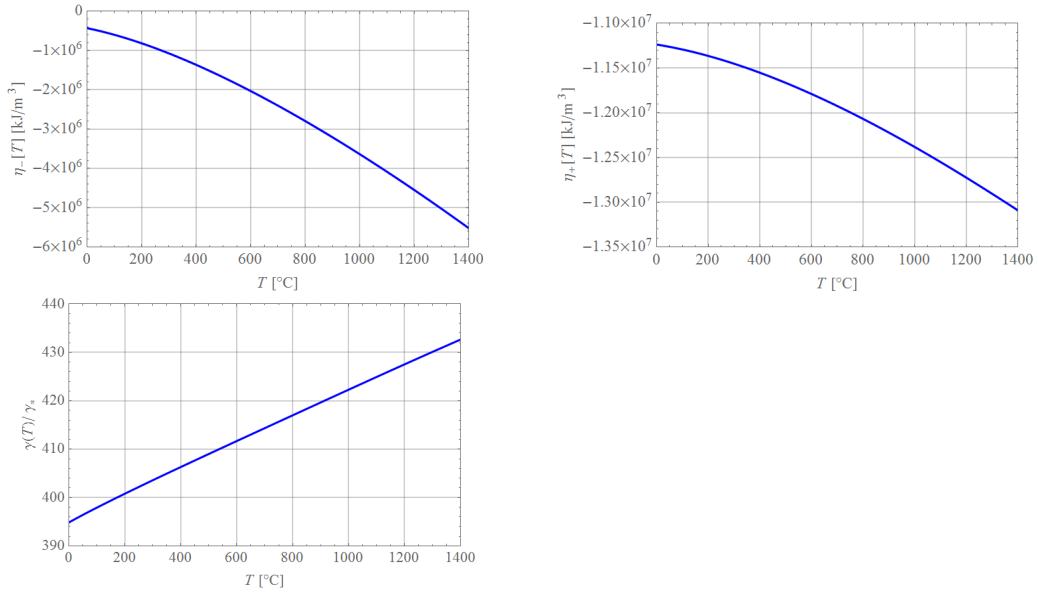
Figure 2.8: Gibbs free energy densities of Si (+) and $SiO_2(-)$ and normalized energy parameter $\gamma(T)/\gamma_*$.

If we wish to determine the equilibrium concentration under stress according to Eqn. (2.7.46) it is necessary to specify the value of $\gamma(T)/\gamma_*$. In this context one option is to treat the quantity $\gamma(T)$ as an "energy parameter," which can be chosen arbitrarily but suitably, in order to study the features of the proposed model. This was the way pursued by Freidin *et al.* in [28]. Another possibility is to calculate it according to Eqn. (2.6.33) from the free energy densities of the constituents, $\eta_-(T)$ and $\eta_+(T)$, respectively. The latter are compiled in data banks (*cf.*, [89]) as functions of temperature. The results of this procedure are shown in Fig. 2.8. Note that when evaluating the gas contribution to $\gamma(T)$ according to Eqn. (2.6.31) it was assumed that $T^*_{0,\text{ref}} = 1000$°C and $s^*_{0,\text{ref}} = 0$. It seems noteworthy that the calculated values for $\gamma(T)/\gamma_*$ are two order of magnitudes higher than those assumed in [28], the main reason being our

choice for ϵ^{ch}. It is curious to note that if we change this number to the true transformation strain, *i.e.*, $0.03 \to 0.38$, this would require us to multiply the values shown in Fig. 2.8$_3$ by the factor 0.006 and we would recover the order of magnitude of $\gamma^{(T)}/\gamma_*$ used in [28]. However, in what follows, we will now follow the other route and treat $\gamma^{(T)}/\gamma_*$ as a suitably chosen "energy parameter."

2.7.6 Results for prescribed displacements

In Fig. 2.9 the relation between equilibrium concentration, c_{eq}/c_0, energy parameter, γ/γ_*, and externally applied strains, ϵ_{11}^0 and ϵ_{22}^0, according to Eqn. (2.7.46) is investigated.
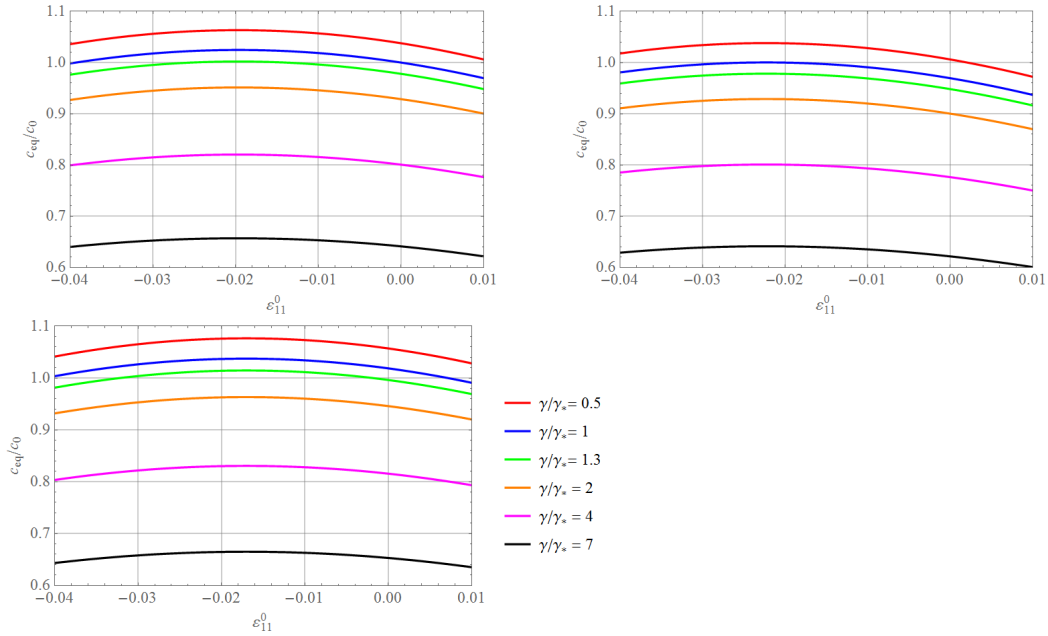
Figure 2.9: Equilibrium concentrations for various values of energy parameter γ/γ_* and

of externally applied strains (see text).

For the first picture it was assumed that $\epsilon_{22}^0 = 0$. Thus it corresponds directly to (and qualitatively agrees with) the result shown for the planar case in [28]. The two following graphs investigate pull $\epsilon_{22}^0 = 0.01$ and push $\epsilon_{22}^0 = -0.01$ in 2-direction. For all pictures a temperature of $T = 1000°C$ was chosen. The following remarks can be made:

- Small energy parameters may lead to $\frac{c_{\mathrm{eq}}}{c_0} > 1$, *i.e.*, according to Eqn. (2.7.46) the reaction may come to a standstill.
- The higher the energy the smaller c_{eq}/c_0; in view of the more realistic data for γ/γ_* shown in Fig. 2.8$_3$ there is a good chance for keeping the oxidation running.
- The applied strain that corresponds to the maximum of the equilibrium

concentration can be calculated from Eqn. (2.7.46) as a function of the other applied strain and of the eigenstrain:

$$\epsilon_{11}^0\big|_{c_{\text{eq}}^{\max}} = -\frac{\left(\frac{E_-}{E_+}\frac{\nu_-(1-\nu_+)}{1-\nu_-^2} - \frac{\nu_+}{1+\nu_+}\right)\epsilon_{22}^0 + \epsilon^{\text{ch}}}{\frac{E_-}{E_+}\frac{1-\nu_+}{1-\nu_-^2} - \frac{1}{1+\nu_+}}. \tag{2.7.49}$$

- If one puts the second strain equal to zero, essentially the old result from [28] is recovered: The applied strain leading to a maximum is always compressive. However, note that the first term in the denominator might affect this result for certain values of Young's moduli and Poisson's ratios.
- For given values of ϵ_{11}^0 a pull in the second direction, $\epsilon_{22}^0 > 0$, leads to overall lower values of equilibrium concentration, whereas a push has the opposite effect, *i.e.*, it impedes silicon oxidation.

We now turn to a study of the equation that describes the growth of the silicone oxide layer, Eqn. (2.7.45): Fig. 2.10 (for $\kappa = 50$). The legend refers to strain values ϵ_{11}^0 corresponding to the previous study [28], namely:

- 1 : no strain energy, *i.e.*, neither external nor eigenstrains,
- 2 : $\epsilon_{11}^0 = 0$,
- 3 : $\epsilon_{11}^0 = 0.01$,
- 4 : $\epsilon_{11}^0 = \epsilon_{11}^0\big|_{c_{\text{eq}}^{\max}}$,
- 5 : $\epsilon_{11}^0 = 1.8\,\epsilon_{11}^0\big|_{c_{\text{eq}}^{\max}}$,
- 6 : $\epsilon_{11}^0 = 2.5\,\epsilon_{11}^0\big|_{c_{\text{eq}}^{\max}}$.

The first picture holds for $\epsilon_{22}^0 = 0$ and the second and third for $\epsilon_{22}^0 = \pm 0.01$. The following conclusions can be drawn:

- Without external strains oxidation is fastest.
- The presence of eigenstrains only (blue lines) can decrease the oxidation level by a considerable percentage.
- In general, pulling increases and pushing decreases the progress of oxidation.

2.7.7 Results for prescribed stresses

Fig. 2.11 shows equilibrium concentration $^c\text{eq}/c_0$, as a function of oxidation height, ξ, for various applied stresses ($\gamma/\gamma_* = 0.95$). The first picture covers the case $\sigma_{22}^0 = 0$ and the second and third for $\sigma_{22}^0 = \pm 0.01$.

The following remarks can be made:

- In contrast to the prescription of displacements the equilibrium concentration depends on the height of the oxidation layer, *i.e.*, the progress of the oxidation. Moreover, this dependence is non-monotoneous.
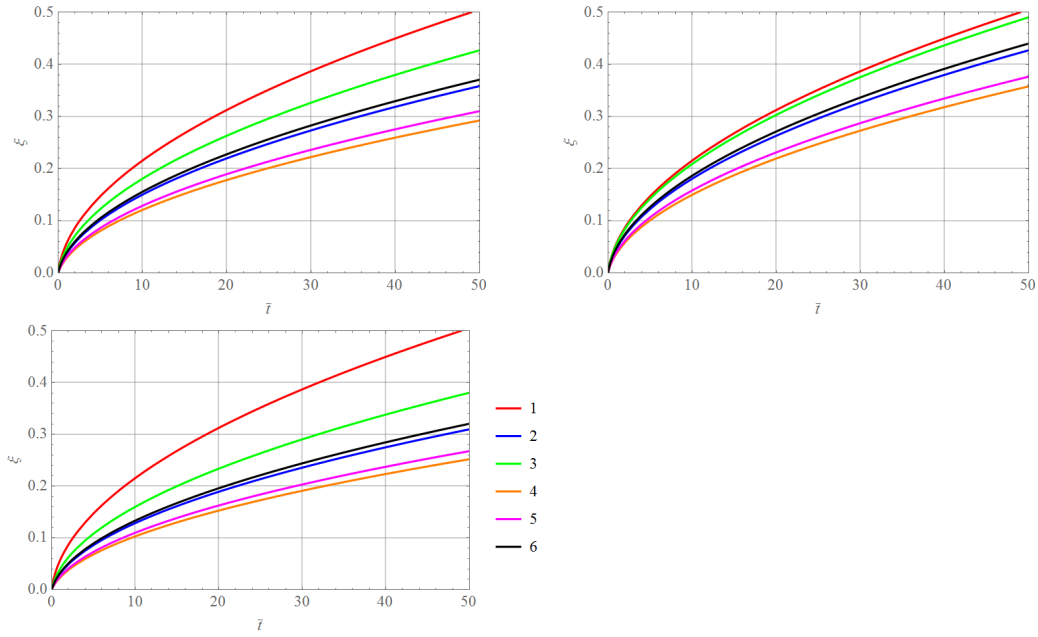
Figure 2.10: Growth of SiO_2 layer for various values of externally applied strains (see text).
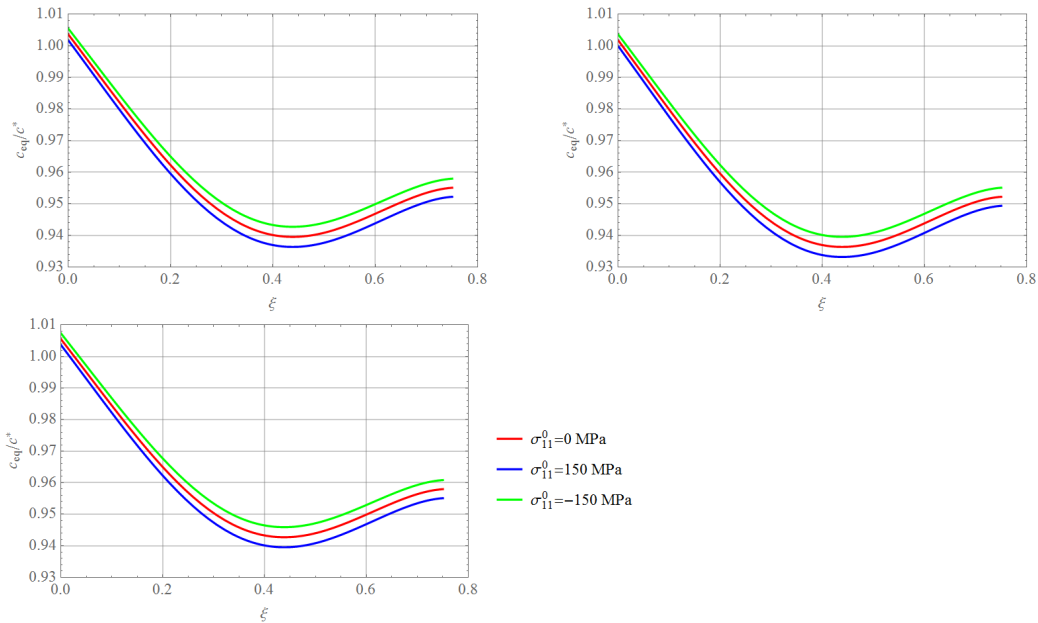

Figure 2.11: Equilibrium concentrations for various applied stresses(see text).

- For given values of σ_{11}^0 a pull in the second direction, $\sigma_{22}^0 > 0$, leads to overall lower values of equilibrium concentration, whereas a push has the opposite effect, *i.e.*, it impedes silicon oxidation. The situation is analogous to the prescription of displacements.

- For very small values of ξ the equilibrium concentration can be greater than 1, which means the reaction will be blocked until a critical height ξ_{cr} has been reached. Positively speaking, one may say that under certain loading conditions a protective layer forms.

The latter effect is explored in more detail in Fig. 2.12. The first picture holds for $\sigma_{22}^0 = 0$, whereas the next two cover the cases $\sigma_{22}^0 = \pm0.005$. In general, pulling will reduce the critical height, *i.e.*, it stimulates oxidation (as pointed out before), and *vice versa*.

Finally, Fig. 2.13 shows the analogue to Fig. 2.10 but for stress loading. As before the first picture is for $\sigma_{22}^0 = 0$ and the other two for $\sigma_{22}^0 \pm 0$. Once more we must conclude that increasing tensile stresses lead to an increase in growth of the oxide layer. Note that a compressive stress in 2-direction (third picture) will lead to a nonlinear decrease of the growth due to the tensile stresses applied in 1-direction.
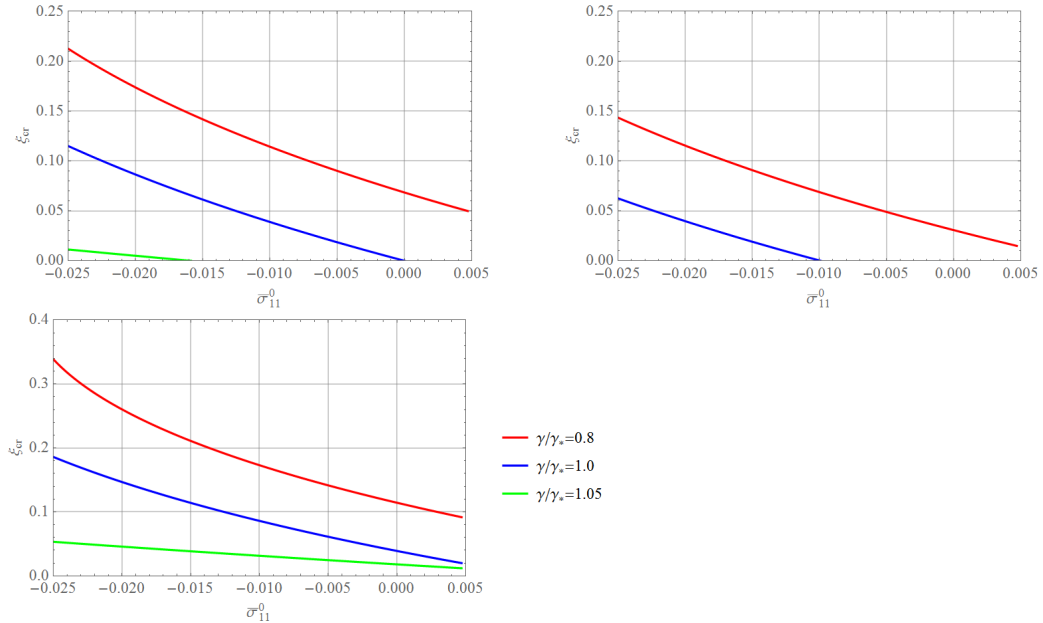

Figure 2.12: Critical height, ξ_{cr}, for further growth as a function of applied stress for different

energy parameter, γ/γ_*.

3 Spinodal decomposition

3.1 Phenomenology

In what follows we will consider binary eutectic solders, which contain almost equal amounts of both atomic species. Two examples come to mind, eutectic
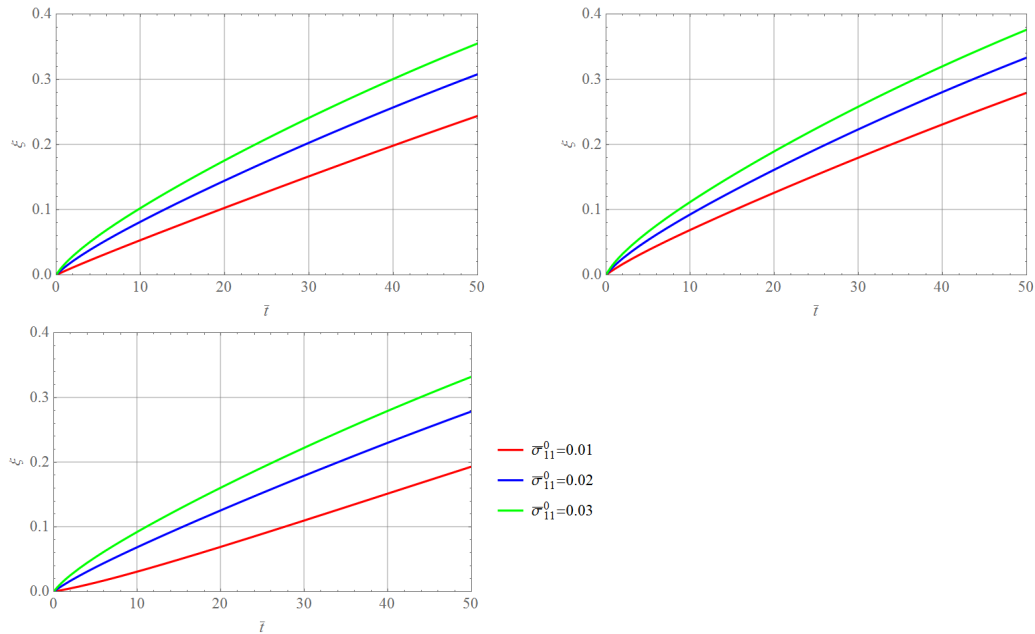
Figure 2.13: Growth of SiO_2 layer for various values of externally applied stresses (see text).

tin (Sn)-lead (Pb) solder SnPb37, where the figure indicates the (approximate) mass percentage of lead, and Silver (Ag)-copper (Cu) solder AgCu29, with (approximately) 29 mass percent of copper. What is important to know is that both species, *i.e.*, tin and lead or silver and copper, do *not* mix arbitrarily when they are in solid form, because their atomic structure is "too different." In both cases only a small amount of solubility is observed. This solubility depends on temperature and it can be read off from the left and right border lines in the phase diagrams shown in Fig. 3.1 once a temperature below the solidification temperature of the eutectic composition (the straight horizontal line) has been reached .

As a result the so-called eutectic microstructure appears. It consists of regions rich in the dominant component, *i.e.*, in our case tin and silver, and regions rich in the minority species, *i.e.*, lead and copper. The latter is known as the α-phase and the former as the β-phase, respectively. In a nutshell: If we ignore the slight solubility completely, we may say that the eutectic mix of tin and lead or silver and copper, which was very intimate in the liquid state, spontaneously separates after solidification. As an analogy consider oil that was originally finely dispersed in water by a mixer. And just like the oil droplets in water will start to coagulate and finally form one big oil droplet initially small α and β phase regions will merge to form bigger ones, the only difference being that the first process occurs in the liquid and the second one in the solid state.

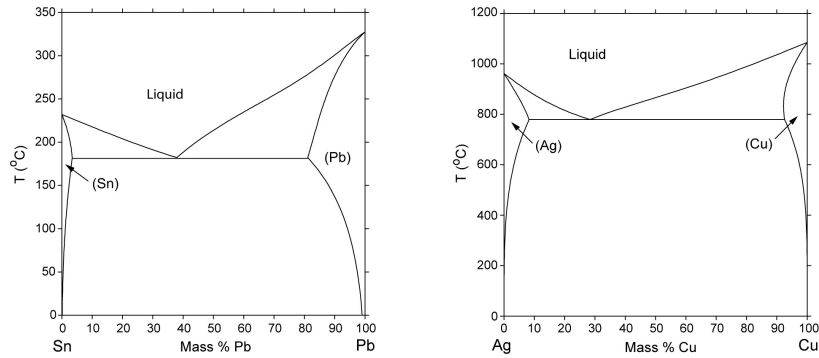Consequently, the resulting eutectic microstructure is heterogeneous. This

Figure 3.1: Phase diagrams of the binary alloys SnPb and AgCu [64], [63].

effect is known under the name *spinodal decomposition.* For the case of SnPb the situation is shown in the two series of micrographs depicted in Fig. 3.2. The first sequence shows the effect of room temperature aging after (a) 2 hours, (b) 17 days, and (c) 63 days after solidification whereas the second row depicts the situation (a) immediately after solidification, (b) after 3 hours at 125°C and (c) 300 hours at 125°C. We must conclude that the originally finely dispersed heterogeneous microstructure "coarsens" and that the coarsening effect is more pronounced at higher temperatures.
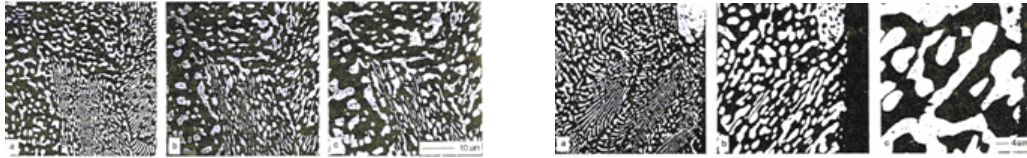

Figure 3.2: Spinodal decomposition and coarsening in eutectic SnPb solder (see text), [34].

A similar observation is made for eutectic AgCu: Fig. 3.3. However, note that AgCu is a high-temperature solder. Hence, compared to SnPb, pronounced coarsening will happen at much higher temperatures. In fact, the sequence of pictures shown in the figure refers to the state immediately after solidification and 2h, 20 h, and 40 h of aging at at a temperature of ca. 700°C, respectively. The influence of temperature can be assessed by means of the so-called homologous temperature, T_{hom}, which is a dimensionless number, given by the ratio of the (absolute) applied temperature, T, to the (absolute) melting temperature, T_{m} of the alloy:

$$T_{\mathrm{hom}} = \frac{T}{T_{\mathrm{m}}}. \tag{3.1.1}$$

The closer the homologous temperature gets to one, the more pronounced the coarsening effect will be. In fact, the melting temperature of eutectic SnPb is 183°C and the one of eutectic AgCu 779.1°C. Thus aging temperatures

of 125°C and 700°C, respectively, should, as observed, lead to a remarkable progress in coarsening.
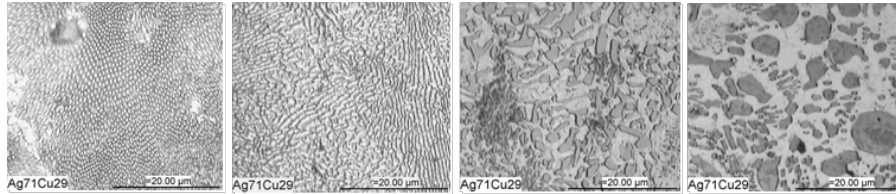

Figure 3.3: Spinodal decomposition and coarsening in eutectic AgCu solder (see text).

In the same context it is worth mentioning that coarsening is the consequence of diffusion of migrating species in a solid. However, this should not be confused with classical Fickean diffusion. The latter starts with a heterogeneous mix and finally leads to total homogenization. In the present case nature attempts to minimize the surface energy so that, suggestively speaking, in the end only two regions, one "blob" of α-phase surrounded by a "sea" of β-phase would remain.
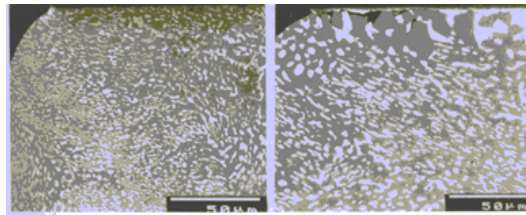

Figure 3.4: Accelerated spinodal decomposition and coarsening in a eutectic SnPb solder ball (see text).

Moreover, it is important to note that the spinodal decomposition and the subsequent coarsening process are not only accelerated by temperature (as, in general, diffusion always is) but also by mechanical stress. This is illustrated in Fig. 3.4, which shows a cross-section of a solder ball made of eutectic SnPb. The picture on the left shows the initial structure which is rather fine grained. The one on the right depicts the microstructure after several thousand temperature cycles. Coarsening is clearly visible, and what is more, it is particularly pronounced and intensified in the corners, which serve as mechanical stress concentrators.

In what follows we shall attempt to model spinodal decomposition as well as the subsequent coarsening process. We will take the influence of both temperature and mechanical stress into account. To do this several points must be addressed. First, it will be necessary to set up the diffusion equations correctly. Note again, that this is not the usual kind of Fickean diffusion where homogenization of an initially heterogeneous structure is finally reached. On the contrary: Here two distinct substructures will prevail, one which shows a

47

concentration rich of lead or copper (the so-called α phase) and one that is rich of tin or silver (the β phase).

Finally in this section the following remark is in order. At the beginning when we started to explain the phenomenology we made a point that the binary eutectic mix should consist of roughly equal amounts of both species. There are other binary eutectic (solder) systems, for example SnAg3.5, where this is not so. Here the 3.5 mass percent of silver will form an intermetallic compound, Ag_3Sn, which precipitates within the tin matrix. We will get back to this in the last chapter of our paper.

3.2 Mathematical treatment of spinodal decomposition

3.2.1 Setting the stage

We consider a body, $\mathscr{B}$, which consists of a binary alloy, *i.e.*, it consists of two chemical species, A and B, at a eutectic composition (see the phase diagram shown in Fig. 3.1). This body is divided into box-like so-called Representative Volume Elements (RVEs), which are characterized by material coordinates $\boldsymbol{x} = x_i\boldsymbol{e}_i$ in three-dimensional space, where $\boldsymbol{e}_i$ is a Cartesian unit base and Einstein's summation convention applies. Due to the fact that the RVE is a rectangular box, it is most useful to use Cartesian coordinates, and we will continue to do so in what follows.

It is assumed that the size of the RVE is large enough so that it is statistically representative of the microstructure developing within. It would take a thorough experimental examination of what the actual size really is, because a eutectic alloy, such as SnPb37 or AgCu29, is usually multigrained and not one single crystal after solidification. The developing eutectic microstructure exists within each of the differently oriented, anisotropic grains and there are certainly interactions between them. Let it suffice to say that in our model grain boundaries are not included at all and that our main objective is to see the two phase regions coalesce and coarsen over time. Clearly we want to be as quantitative as possible and, therefore, we shall look at specific values of diffusion constants. However, we ignore that diffusion might be faster along grain boundaries than within the bulk since we do not model such boundaries. Our RVE will have *two* crystal symmetries, though, one for the α and one for the β-phase, which can be arbitrarily oriented from each other, as far as the main crystallographic axes are concerned.

Within the RVE there are regions of two different phases, the α-phase, which is rich in the minority species of the alloy, and the β-phase, which is rich in the dominant sort of atoms. Both regions are assigned elastic anisotropic properties. In the case of SnPb37 the α-phase has cubic material symmetry and the β-phase has tetragonal symmetry (*i.e.*, the symmetry of their dominant elements, lead and tin, respectively). In the case of AgCu29 both phases are

cubic. From the mathematical point of view, the final objective of the model is to determine the strain fields, $\boldsymbol{\epsilon}(\boldsymbol{x}, t)$, and the field of the concentration of the dominant species, $c(\boldsymbol{x}, t) \equiv c_{\mathrm{A}}(\boldsymbol{x}, t)$, for all material points, $\boldsymbol{x} \in B$, and at all times, t. In this paper we will assume that the temperature distribution, $T(t)$, within the body B is homogeneous and a known ("given") function of time. Moreover, note that for a binary mixture only one concentration field needs to be determined since, due to mass conservation, the following identity holds:

$$c_{\mathrm{A}}(\boldsymbol{x}, t) + c_{\mathrm{B}}(\boldsymbol{x}, t) = 1. \tag{3.2.1}$$

Here a remark is in order: In contrast to the previous section (see, in particular, Eqn. (2.6.15)) these concentrations are dimensionless. They were defined by using only the corresponding mass densities, *i.e.*, $c_{\mathrm{A/B}} := \rho_{\mathrm{A/B}}/(\rho_{\mathrm{A}} + \rho_{\mathrm{B}})$.

3.2.2 The mechanical part of the model - Basic relations

It is assumed that in the present case mechanical equilibrium is much faster to achieve than thermodynamical (or chemical) equilibrium. Consequently, the mechanical part of the problem or, in other words, the solution for the strain fields is based on the equation for static equilibrium of forces, *i.e.*,

$$\frac{\partial \sigma_{ji}}{\partial x_j} = 0, \tag{3.2.2}$$

in combination with linear kinematic conditions and Hooke's law:

$$\epsilon_{ij} = \left(\frac{\partial u_i}{\partial x_j} + \frac{\partial u_j}{\partial x_i} \right), \;\; \sigma_{ij} = C_{ijkl} \left(\epsilon_{kl} - \epsilon_{kl}^* \right), \tag{3.2.3}$$

$\boldsymbol{\sigma}$ being Cauchy stress, $\boldsymbol{\epsilon}$ linear strain, $\boldsymbol{u}$ the displacement vector, $\boldsymbol{C}$ the stiffness tensor, and $\boldsymbol{\epsilon}^*$ the eigenstrains, all in Cartesian coordinates. In the simulations we assume that the α and β regions are coherent. However, there is some evidence speaking against this assumption, because the lattice constants of the α and β-phases are very different for both eutectic solders, SnPb37 and AgCu29. There is no damage or plastic deformation observes, so that coherency is questionable. However, we present eigenstrains resulting from different thermal expansion of the two phases and put:

$$\boldsymbol{\epsilon}^* = \boldsymbol{\alpha} \left(T - T_{\mathrm{R}} \right) , \;\; \boldsymbol{\alpha}(\boldsymbol{x}, t) = \theta(\boldsymbol{x}, t)\boldsymbol{\alpha}^{\alpha} + \left[1 - \theta(\boldsymbol{x}, t) \right] \boldsymbol{\alpha}^{\beta}, \tag{3.2.4}$$

where T_{R} is the reference temperature of the stress-free state which, in the present case, will be chosen as the solidus temperature of the eutectic solder. The symbols $\boldsymbol{\alpha}^{\alpha/\beta}$ refer to the tensors of thermal expansion coefficients of the α-phase and of the β-phase, respectively. To a first-order approximation the elements of these matrices are given by the thermal expansion coefficients of pure lead and tin. The symbol $\theta(\boldsymbol{x}, t)$ refers to the *phase field* which links

the α and β-regions continuously with each other. It is essentially a Heaviside function with physical significance, since we define it as:

$$\theta(\boldsymbol{x}, t) := \frac{c_\beta - c(\boldsymbol{x}, t)}{c_\beta - c_\alpha}. \qquad (3.2.5)$$

It is easily verified that $\theta(\boldsymbol{x}, t) = 1$ if $\boldsymbol{x} \in \alpha$, *i.e.*, within a fully developed α-phase, and $\theta(\boldsymbol{x}, t) = 0$ *vice versa*. Note that the phase field is used in the same manner in order to characterize the spatial dependence of other material parameters, such as the local stiffness, $\boldsymbol{C}$, the coefficients of surface tensions, $\boldsymbol{a}$, or the mobility coefficients, $\boldsymbol{M}$, which we will encounter later.

Initially, a suitable function of position will be assumed for $c(\boldsymbol{x}, t)$. For example, this could be an essentially homogeneous field with nuclei in form of small localized B-rich regions. By virtue of Eqn. (3.2.4), this results in an initial condition for the eigenstrains $\boldsymbol{\epsilon}^\star$. Of course, any micrograph could serve as an initial condition as well. We would then predict how this microstructure changes when we switch to another temperature or when an external stress is applied. In any case the calculation of current stresses and strains is based on Eqn. (3.2.2) and (3.2.3). In the next subsections we will discuss how this can be achieved efficiently for the initial time as well as during the subsequent time steps.

3.2.3 The mechanical part of the model - Numerical approach

Spectral methods or, more specifically, Discrete Fourier Transforms (DFT) have been used in a promising way to solve stress/strain problems for heterogeneous solids (*e.g.*, [11], [86], [52], [53], [21], [57], [58], [59], [61]). In what follows we will illustrate and evaluate the procedure for 2D. Specifically we will consider the case that strains ϵ_{11}^0, ϵ_{22}^0, $\epsilon_{12}^0 = \epsilon_{21}^0$ are applied to the periphery of the RVE as indicated in Fig. 3.5.
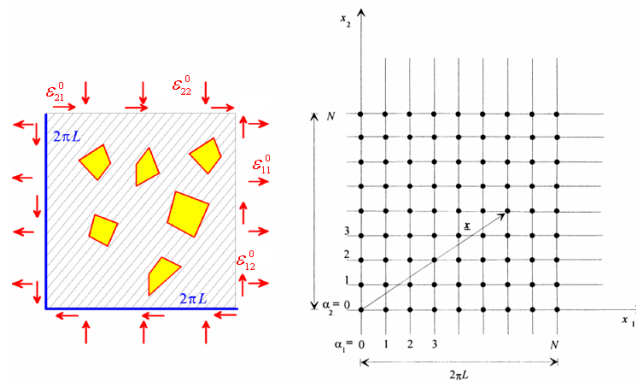

Figure 3.5: Square 2D-RVE and its dicretization (see text).

Hence we may write:

$$\int\limits_{x_2=0}^{2\pi L} \epsilon_{11}\mathrm{d}x_2 + \int\limits_{x_2=0}^{2\pi L} \epsilon_{12}\mathrm{d}x_2 = \left(\epsilon_{11}^0 + \epsilon_{12}^0\right)2\pi L \ , \qquad (3.2.6)$$

$$\int\limits_{x_1=0}^{2\pi L} \epsilon_{21}\mathrm{d}x_1 + \int\limits_{x_1=0}^{2\pi L} \epsilon_{22}\mathrm{d}x_1 = \left(\epsilon_{12}^0 + \epsilon_{22}^0\right)2\pi L \ .$$

where the strains under the integral on the left hand sides are the solution to the Boundary Value Problem (BVP) of Eqns. (3.2.2), (3.2.3) evaluated at x_1 and $x_2 = 0$ or $2\pi L$, respectively. In fact, as we shall see now, we will require these strains to be periodical across an array of RVEs extended across the two-dimensional plane. On a single RVE we define the following N equidistant grid points separated by the distance h:

$$\boldsymbol{x} = h\boldsymbol{\alpha}, \ \boldsymbol{\alpha} = (\alpha_1, ..., \alpha_d) \ , \ \alpha_j \in (0, 1, ..., N-1) \ , \ h = \frac{2\pi L}{N}. \qquad (3.2.7)$$

Depending on the dimension of the RVE the indices j and d run from 1 up to a maximum of 3. For 2D we have $j \in (1, 2)$, $d = 2$. All field variables, $f(\boldsymbol{x}, t)$, will be calculated on the grid points, in real, $f(\boldsymbol{\alpha}, t)$, and in discrete Fourier space, $\hat{f}(\boldsymbol{s}, t)$, respectively. For this purpose it is necessary to define the Discrete Fourier Transform (DFT) and its inverse as follows:

$$\hat{f}(\boldsymbol{s}) = \frac{1}{N^{d/2}} \sum_{\alpha_1=0}^{N-1} ... \sum_{\alpha_d=0}^{N-1} f(\boldsymbol{\alpha})\exp\left(\mathrm{i}2\pi\frac{\boldsymbol{s}\cdot\boldsymbol{\alpha}}{N}\right) \equiv Y\left[f(\boldsymbol{\alpha})\right] \ , \qquad (3.2.8)$$

$$f(\boldsymbol{\alpha}) = \frac{1}{N^{d/2}} \sum_{s_1=0}^{N-1} ... \sum_{s_d=0}^{N-1} \hat{f}(\boldsymbol{s})\exp\left(-\mathrm{i}2\pi\frac{\boldsymbol{s}\cdot\boldsymbol{\alpha}}{N}\right) \equiv Y^{-1}\left[\hat{f}(\boldsymbol{s})\right] \ .$$

Periodicity conditions can be formulated as follows:

$$f(\boldsymbol{\alpha} + \boldsymbol{N}\boldsymbol{r}) = f(\boldsymbol{\alpha}) \ , \ \ \boldsymbol{r} = (r_1, ..., r_d) \ , \ \ r_j \in \mathbb{Z}. \qquad (3.2.9)$$

DFT is very useful in context with the spatial derivatives of Eqns. (3.2.2), (3.2.3). The following relation hold for first derivatives:

$$Y\left(\frac{\partial f(\boldsymbol{\alpha})}{\partial x_j}\right) = \xi_j(s_j)Y\left(f(\boldsymbol{\alpha})\right) + O(h^2) \ , \ \ \xi_j(s_j) = -\frac{\mathrm{i}}{h}\sin\left(\frac{h}{l}s_j\right). \qquad (3.2.10)$$

and these for second derivatives:

$$Y\left(\frac{\partial^2 f(\boldsymbol{\alpha})}{\partial x_j^2}\right) = \xi_{\underline{jj}}(s_j)Y\left(f(\boldsymbol{\alpha})\right) + O(h^2), \ \ \xi_{\underline{jj}}(s_j) = \frac{2}{h^2}\left[\cos\left(\frac{h}{l}s_j\right) - 1\right], \qquad (3.2.11)$$

$$Y\left(\frac{\partial^2 f(\boldsymbol{\alpha})}{\partial x_i \partial x_j}\right) = \xi_{ij}(s_i, s_j)Y\left(f(\boldsymbol{\alpha})\right) + O(h^2) \ , \ \ \xi_{ij}(s_i, s_j) = -\frac{1}{h^2}\sin\left(\frac{h}{l}s_i\right)\sin\left(\frac{h}{l}s_j\right).$$

DFT will now be applied to Eqns. (3.2.2), (3.2.3), *i.e.*, to static, linear-elastic problems with small deformations. To this end we make use of the Equivalent Inclusion Technique (EIT) which goes back to Eshelby [62]. This method circumvents the problem of the spatial dependence of the stiffness matrix by introducing an auxiliary strain field $\epsilon_{kl}^{\text{aux}}$ ([53], [58]) and an auxiliary *constant* stiffness matrix, C_{ijkl}^{aux}, as follows:

$$\sigma_{ij}(\boldsymbol{\alpha},t) = C_{ijkl}(\boldsymbol{\alpha},t)\left[\epsilon_{kl}(\boldsymbol{\alpha},t) - \epsilon_{kl}^*(\boldsymbol{\alpha},t)\right] = \qquad (3.2.12)$$

$$C_{ijkl}^{\text{aux}}\left[\epsilon_{kl}(\boldsymbol{\alpha},t) - \epsilon_{kl}^*(\boldsymbol{\alpha},t) - \epsilon_{kl}^{\text{aux}}(\boldsymbol{\alpha},t)\right].$$

After insertion into the equations we obtain:

$$C_{ijkl}^{\text{aux}}\frac{\partial^2 u_k}{\partial x_j \partial x_l} = C_{ijkl}^{\text{aux}}\frac{\partial}{\partial x_j}\left(\epsilon_{kl}^{\text{aux}} + \epsilon_{kl}^*\right) \qquad (3.2.13)$$

Periodicity of all fields is assumed and by virtue of the differentiation theorems (3.2.10), (3.2.11) this system of PDEs is mapped onto a system of linear equations in Fourier spac:

$$C_{ijkl}^{\text{aux}}\xi_{jl}\hat{u}_k = C_{ijkl}^{\text{aux}}\xi_j\left(\hat{\epsilon}_{kl}^{\text{aux}} + \hat{\epsilon}_{kl}^*\right) \qquad (3.2.14)$$

Note, in this context, that the constancy of C_{ijkl}^{aux} was important or otherwise it would not have been possible to map a partial differential equation onto a system of linear equations, which can be solved explicitly in discrete Fourier space. If we apply inverse DFT the following solution for the strain tensor is obtained:

$$\epsilon_{kl}(\boldsymbol{\alpha},t) = Y^{-1}\left[\hat{A}_{ijkl}^{\text{aux}}\hat{\epsilon}_{kl}^{\text{aux}}\right](\boldsymbol{\alpha},t) + Y^{-1}\left[\hat{A}_{ijkl}^{\text{aux}}\hat{\epsilon}_{kl}^*\right](\boldsymbol{\alpha},t) + \epsilon_{kl}^0, \qquad (3.2.15)$$

with:

$$\hat{A}_{ijkl}^{\text{aux}} = \begin{cases} 0 & \text{for } \boldsymbol{s} = \boldsymbol{0} \\ \frac{1}{2D}\left(\xi_i N_{js} + \xi_j N_{is}\right)C_{srkl}^{\text{aux}}\xi_r & \text{for } \boldsymbol{s} \neq \boldsymbol{0} \end{cases}. \qquad (3.2.16)$$

and D and N_{ij} are the determinant and the discriminant of the following matrix:

$$M_{ik} = C_{ijkl}^{\text{aux}}\xi_{jl} \quad \Rightarrow \quad M_{ik}^{-1} = \frac{N_{ik}}{D}. \qquad (3.2.17)$$

These are known functions of the stiffness C_{ijkl}^{aux} (which will soon be chosen suitably), and of the Fourier transforms of the difference quotients (3.2.11). Depending on the degree of anisotropy they can have a very complicated form. However, for cubic materials and 2D they can be written down in a somewhat concise form, namely:

$$D = -\mu(\lambda + 2\mu + \mu')(\xi_{kk})^2 - (\lambda + 2\mu + \mu')^2\xi_{11}\xi_{22} + (\lambda + \mu)\xi_{12}^2, \qquad (3.2.18)$$

$$N_{ij} = -(\lambda + 2\mu + \mu')\xi_{kk}\delta_{ij} + (\lambda + \mu)\xi_{ij} + \mu'\delta_{ijkl}\xi_{kl},$$

where δ_{ij} and δ_{ijkl} are Kronecker symbols and λ, μ, and μ' are Lamé's constants.

The term ϵ_{kl}^0 in Eqn. (3.2.15) deserves a comment. On the one hand side it is the applied strain, on the other hand it is also the average strain as we shall see now. First we define the average strain by:

$$\bar{\epsilon}_{ij} \coloneqq \frac{1}{N^d} \sum_{\alpha_1=0}^{N-1} ... \sum_{\alpha_d=0}^{N-1} \epsilon_{kl}(\boldsymbol{\alpha}). \tag{3.2.19}$$

Then we note that according to the definition of DFT in Eqn. (3.2.8) we have:

$$\hat{\epsilon}_{ij}(\mathbf{0}) = \frac{1}{N^{d/2}} \sum_{\alpha_1=0}^{N-1} ... \sum_{\alpha_d=0}^{N-1} \epsilon_{kl}(\boldsymbol{\alpha}). \tag{3.2.20}$$

By comparison we find:

$$\bar{\epsilon}_{ij} = \frac{1}{N^{d/2}} \hat{\epsilon}_{ij}(\mathbf{0}). \tag{3.2.21}$$

Now the solution (3.2.15) requires:

$$\hat{\epsilon}_{kl}(\mathbf{0}) = \hat{A}_{ijkl}^{\mathrm{aux}}(\mathbf{0}) \hat{\epsilon}_{kl}^{\mathrm{aux}}(\mathbf{0}) \hat{A}_{ijkl}^{\mathrm{aux}}(\mathbf{0}) \hat{\epsilon}_{kl}^*(\mathbf{0}) + \hat{\epsilon}_{kl}^0(\mathbf{0}) \equiv N^{d/2} \epsilon_{kl}^0, \tag{3.2.22}$$

because of Eqn. (3.2.21):

$$\bar{\epsilon}_{ij} = \epsilon_{kl}^0, \tag{3.2.23}$$

in words, the average strains are given by the applied strains. We will now turn to the problem of how to determine the auxiliary strain field, $\boldsymbol{\epsilon}^{\mathrm{aux}}$. For this purpose we insert the solution from Eqn. (3.2.15) into (3.2.12) and find:

$$C_{ijkl}^{\mathrm{aux}} \left(Y^{-1} \left[\hat{A}_{klop}^{\mathrm{aux}} \hat{\epsilon}_{op}^{\mathrm{aux}} \right] + Y^{-1} \left[\hat{A}_{klop}^{\mathrm{aux}} \hat{\epsilon}_{op}^* \right] + \epsilon_{kl}^0 - \epsilon_{kl}^* - \epsilon_{kl}^{\mathrm{aux}} \right) = \tag{3.2.24}$$

$$\left(C_{ijkl}^\beta - \theta \left[C_{ijkl}^\beta - C_{ijkl}^\alpha \right] \right) \left(Y^{-1} \left[\hat{A}_{klop}^{\mathrm{aux}} \hat{\epsilon}_{op}^{\mathrm{aux}} \right] + Y^{-1} \left[\hat{A}_{klop}^{\mathrm{aux}} \hat{\epsilon}_{op}^* \right] + \epsilon_{kl}^0 - \epsilon_{kl}^* \right),$$

where we have made use of the representation shown in Eqn. (3.2.4)$_2$ when applied to $\boldsymbol{C}$. This becomes a functional equation for $\boldsymbol{\epsilon}^{\mathrm{aux}}$ that can be solved iteratively, provided we specify the auxiliary stiffness suitably, so that convergence can be reached. Various choices are possible and the details are explained in [7]. Here it may suffice to say that in our case the softer, lead or copper rich α-phase will start growing in an initially uniform, stiffer β phase rich in tin or silver. Then the choice $\boldsymbol{C}^{\mathrm{aux}} \equiv \boldsymbol{C}^\beta$ will lead to convergence, and Eqn. (3.2.24) simplifies as follows:

$$C_{ijkl}^\beta \overset{(n+1)}{\epsilon}{}_{kl}^{\mathrm{aux}} = \theta \left[C_{ijkl}^\beta - C_{ijkl}^\alpha \right] \left(Y^{-1} \left[\hat{A}_{klop}^\beta \overset{(n)}{\hat{\epsilon}}{}_{op}^{\mathrm{aux}} \right] + \tag{3.2.25}$$

$$Y^{-1} \left[\hat{A}_{klop}^\beta \hat{\epsilon}_{op}^* \right] + \epsilon_{kl}^0 - \epsilon_{kl}^* \right).$$

The last equation already indicates that it is solved by a Neumann iteration: The n-th iteration is inserted on the right side in order to obtain the $n+1$th iteration. As a starting value one may use $\overset{(0)}{\epsilon}{}_{kl}^\beta = 0$. Note that A_{klop}^{aux} has been replaced by A_{klop}^β. The latter can be calculated from Eqn. (3.2.16) and (3.2.16) after replacing C_{ijkl}^{aux} by C_{klop}^β.

3.2.4 The thermodynamics part of the model - Basic relations

Once the local stresses and strains are known at a certain time, t, they will be used to compute the evolution of the distribution of concentrations, c, during the next time-step, dt. In order to do this a diffusion equation is needed. It reads:

$$\rho_0 \frac{\partial c}{\partial t} + \frac{\partial J_i}{\partial x_i} = 0 \qquad (3.2.26)$$

with the *extended* diffusion flux being:

$$J_i = -\rho_0 M_{ij} \frac{\partial}{\partial x_j} \left(\frac{\partial \psi}{\partial c} - a_{kl} \frac{\partial^2 c}{\partial x_k \partial x_l} + \frac{\partial}{\partial c} \frac{1}{2} \sigma_{kl} (\epsilon_{kl} - \epsilon_{kl}^*) \right) , \qquad (3.2.27)$$

where ρ_0 is the total mass density of the alloy with respect to the reference configuration, *i.e.*, a constant, M_{ij} denotes the mobility matrix, $\psi = \psi(T, c)$ is the configurational part of the free energy density (in kg/m³), and a_{kl} are the higher gradient coefficients. Note that the first term in the diffusion flux leads to the classical diffusion equation as proposed by Fick, whereas the second part contains extensions of the diffusion equation as introduced by Cahn and Hilliard, a_{ij} being a matrix of surface tension related quantities (see [10], [16], or [36], Chapter 3, for a comprehensive summation of the original results), which is related to the surface tension coefficients of the α- and β-phase analogously to Eqn. (3.2.4)$_2$. Note that the diffusional flux also contains a term based on the elastic stored energy, which takes the influence of the mechanical stresses and strains on the diffusion process explicitly into account. The situation is similar to the chemical affinity tensor which also contained the stored energy, Eqn. (2.6.25). However, note that only at the interface this effect became visible, Eqns. (2.6.32) and (2.6.38). It is not part of the diffusion flux in the bulk, Eqns. (2.6.36). Finally note that a "derivation" of this result based on the second law of thermodynamics can be found in [19].

There are various ways to make the configurational part of the free energy density explicit. A phenomenological one is to choose the following non-convex function of the concentrations (see [10], pg. 261 or [91], pg. 150):

$$\psi = \psi_0 \left[\left([c^\alpha - c_0]^2 - [c - c_0]^2 \right)^2 - b [c^\alpha - c_0] \right] , \quad c_0 = \tfrac{1}{2} \left(c^\alpha + c^\beta \right) . \qquad (3.2.28)$$

The non-convex form is required in order to guarantee coexistence of both phases. Alternatively one may turn to data banks, such as MTData [54], and work with a logarithmic *ansatz* of the Redlich-Kistler type, see [20] for details.

3.2.5 The thermodynamics part of the model - Numerical approach

Not only the elastic problem is solved in Fourier space. The diffusion equation is treated analogously, at least as far as the spatial part is concerned. For

example, if we assume for simplicity that $M^\alpha = M^\beta = M'$, we may write instead of Eqn. (2.6.25), (2.6.26):

$$\frac{1}{M}\frac{\mathrm{d}\hat{c}}{\mathrm{d}t} = \xi_{ii}\left[Y\left(\frac{\partial\psi}{\partial c}\right) - Y\left(a_{kl}\frac{\partial^2 c}{\partial x_k \partial x_l}\right) + Y\left(\frac{\partial}{\partial c}\tfrac{1}{2}\sigma_{kl}(\epsilon_{kl} - \epsilon_{kl}^*)\right)\right] \qquad (3.2.29)$$

It should be mentioned that the case with different mobilities in the α and in the β phase was treated in [20]. If we now introduce a dimensionless time as follows:

$$\bar{t} = t\frac{M\psi_0}{L^2} = n\Delta\bar{t} , \quad n \in \mathbb{N}, \qquad (3.2.30)$$

where L is the size of the (square) RVE, we may rewrite the diffusion equation in Fourier space in dimensionless form:

$$\frac{\hat{c}^{n+1} - \hat{c}^n}{\Delta\bar{t}} = \bar{\xi}_{ii}\left[Y\left(\frac{\partial\bar{\psi}}{\partial c}\right)\bigg|_{\hat{c}=\hat{c}^n} - \bar{a}_{kl}^\beta\bar{\xi}_{kl}\hat{c}^{n+1} + \left(\bar{a}_{kl}^\beta - \bar{a}_{kl}^\alpha\right)Y\left(\theta\frac{\partial^2 c}{\partial\bar{x}_k\partial\bar{x}_l}\right)\bigg|_{\hat{c}=\hat{c}^n}\right.$$
$$\left. -Y\left(\bar{\sigma}_{kl}\frac{\epsilon_{kl}^*}{\partial c}\right)\bigg|_{\hat{c}=\hat{c}^n} + Y\left(\frac{\partial}{\partial c}\tfrac{1}{2}\bar{\sigma}_{kl}(\epsilon_{kl} - \epsilon_{kl}^*)\right)\bigg|_{\hat{c}=\hat{c}^n}\right] \qquad (3.2.31)$$

with the following dimensionless quantities:

$$\bar{\psi} = \frac{\psi}{\psi_0} , \quad \bar{a}_{kl} = \frac{a_{kl}}{\psi_0 L^2} , \quad \bar{\sigma}_{kl} = \frac{\sigma_{kl}}{\psi_0} , \quad \bar{x}_l = \frac{x_l}{L} , \qquad (3.2.32)$$

$$\bar{\xi}_{jj}(s_j) = 2\left(\tfrac{N}{2\pi}\right)^2\left[\cos\left(\tfrac{2\pi}{N}s_j\right) - 1\right] , \quad \xi_{ij}(s_i, s_j) = -\left(\tfrac{N}{2\pi}\right)^2\sin\left(\tfrac{2\pi}{N}s_i\right)\sin\left(\tfrac{2\pi}{N}s_j\right).$$

3.2.6 A few words regarding the material parameters

Without proper knowledge of the material coefficients it is impossible to perform numerical simulations based on the system of equations shown in Sections 3.2.3 and 3.2.5. All data that was used here can be found for SnPb in [19], [20], [44], and for AgCu in [3], [2], [4], [5], [6]. It is therefore pointless to repeat all values in here. However, it is certainly fair to comment on the reliability of the data and how easily or difficult they can be obtained. In this context it is also worth while mentioning as to whether they were collected from sources unrelated to the model that was presented here.

Stiffnesses Values for C_{ijkl} of the various phases are relatively easy to obtain. They usually stem from acoustic or tensile test specimen measurements and refer to the main crystallographic axes of a single crystal made of the pure species, *i.e*, Sn, Pb, *etc.* Consequently, they show a high degree of reliability and independence from the model. In order to obtain stiffness data for the phases concentration based rule of mixtures could be used. However, in our simulations we simply chose the data of the pure species of the majority component of the phases since the concentration of the minority species is small and leaves the lattice essentially unchanged.

It should be mentioned that in order to bring the model as close as possible to reality the orientation it would be helpful to have EDX data of the lattice orientation of the phases available. Then known rotation matrices could be used to transform the stiffnesses from the original crystal lattice frame to the one pertinent in a given micrograph. Such a detailed analysis has not been done yet. However, we sometimes changed the orientations of the phase lattices w.r.t. the frame of the RVE in order to explore how this would affect microstructural evolution. There is some influence, but it is small and a statistically relevant analysis has not been performed.

Thermal expansion coefficients The situation is similar to that of stiffness data: Values for the pure species (anisotropic) are not too difficult to obtain. They seem reliable and are independent of the model presented here. Sometimes the differences between the expansion in the various directions and, of course, between phases can be large. Hence, rumor has it that no coherent interface is formed, or dislocations start moving, so that residual stresses hardly develop and might be discarded in the model analysis.

Note that in our simulations we assumed coherency and explored how such residual stresses on top of externally applied ones affect the coarsening behavior. This might be unphysical but, on the other hand, shows that tendencies can be explored relatively easily on the computer that are otherwise hard to realize. If these tendencies prove beneficial from the standpoint of guaranteeing a fine microstructure for a longer time it might be worth exploring how this could be done in practice, by addition of interface stabilizers (say).

Higher gradient coefficients Values for a_{kl}, in particular such for the individual phases, are almost impossible to find in the literature and extremely hard to come by. One way of getting quantitative information is from atomistic considerations (see [3]) where interatomic potentials are used for their prediction. However, the reliability of the result depends very much on the interatomic model that is used. It may result in artifacts, such as the Cauchy paradox encountered in the same context when predicting stiffness data from interatomic potentials. For our simulations we tried very hard to provide information as accurately as possible. It seems that cubic lattices (such as Pb, Cu, Ag) can bee treated with sufficient accuracy. The results for higher forms of anisotropy (Sn, tetragonal) seem less reliable at least under the assumption of purely radially dependent potentials.

Diffusion and mobility coefficients The situation is almost as desperate as in the case of higher gradient coefficients. There is some information on the migration of tracer elements of the minority species of the phases in the pure lattice of the majority species. Very often there is also information reg. grain boundary diffusion coefficients available, which generally lead to a faster migration. However, grain boundaries are not part of our continuum model. Here it does not come as close to reality as it should. Hence one might be tempted to use artificially high data and to "adjust" the model to reality. This,

however, is against our belief of how modeling should be. Hence we run into problems with the reliability of our temporal prediction (see the normalization of time, which includes the mobility, in Eqn. (3.2.30)).

Thermal parts of the free energy density There are two possibilities to obtains these parameters. First, an empirical ansatz as shown in Eqn. (3.2.28) can be made. However, this opens up the question which value to choose for the constant ψ_0. Since it is part of the normalization factor shown in Eqn. (3.2.30), it is tempting to adjust it to actual observations. However, this is strictly against our belief of what modeling should be.

Alternatively one can turn to data banks such as Thermocalc [89] or MTData [54]. Based on calorimetric measurements expressions for pure substances and of the solder alloy systems of interest the corresponding Gibbs free energy densities can be found in there. They are provided either as long, temperature dependent lists of numbers or in terms of coefficients to be inserted into *ansatzes* for the Gibbs free energy densities (see [20] for an example of the latter). Note that for solids the difference in Gibbs free energy densities and free energy densities is absolutely negligible. Hence, this data is reliable provided that the corresponding calorimetric measurements were made at all. In fact, for new solder materials these might not yet be available and one might have to wait until new updates for the data banks become available. However, for the solders studied by us this data was available.

3.3   Simulations

In what follows we shall a selection of simulations together with a brief discussions. We will concentrate on SnPb37. Further details and various other simulations are presented in [19], [20], [44] (for SnPb), and in [3], [2], [4], [5] (for AgCu).

3.3.1   Initial conditions

In order to solve Eqns. (3.2.2), (3.2.3), (3.2.26), (3.2.27) an initial condition is required. This initial condition is a homogeneous distribution of the eutectic mixture. However, if we start with a perfectly homogeneous distribution nothing would happen. The decomposition has to be triggered. Fig. 3.6 shows how this is achieved: Some very slight inhomogeneities in concentration are introduced at randomly chosen positions of the RVE.

3.3.2   Aging at high and low temperatures

Fig. 3.7 shows the predicted aging at room temperature (top) and at 125℃(bottom). The degree of coarsening in the last pictures of each row seems to be about the
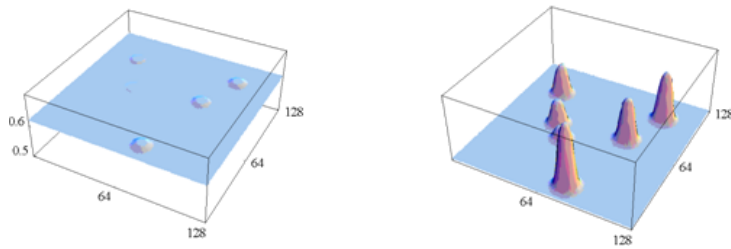
Figure 3.6: Initial condition for spinodal decomposition, (magnified view on the right).

same. However, note that the first row corresponds to 90 h and the second one to 5 min of exposure to temperature.
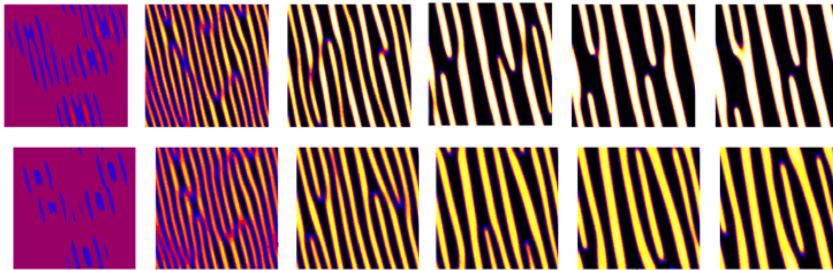

Figure 3.7: Aging at RT (top) and 125℃(bottom).

3.3.3 Simulation of temperature cycling

The sequence of pictures shown in Fig. 3.8 shows what happens to tin-lead solder during temperature cycling, which is frequently performed while testing microelectronic components. The first row shows the aging process at room temperature, which has already been shown before. Then we use the last picture as initial condition to further simulations of the coarsening process at 125℃. Obviously this results in visible further coarsening and, what is more, at a much smaller time than the first row of pictures represents, 90 h *vs.* 5 min.
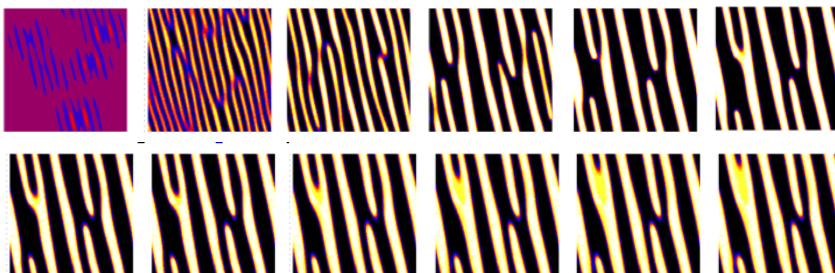

Figure 3.8: Effect of temperature cycling (see text).

3.3.4 Influence of surface tensions

So far, an anisotropic behavior has been assumed as far as the higher gradient coefficients are concerned: a_{kl}^{α} for tin is not a spherical tensor, due to its tetragonal crystal structure (see [19] and [20] for details). The sequence of pictures shown in Fig. 3.9 shows what happens if we switch to $a_{kl} = a\delta_{kl}$: the developing substructures have a circular instead of an elongated structure. In fact, this is what we observe in the case of AgCu29 (see Fig. 3.3).
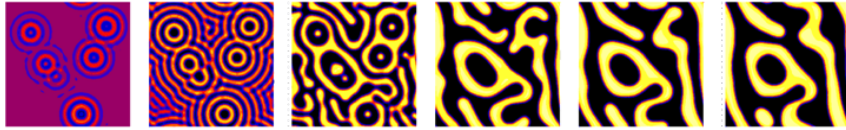
Figure 3.9: Coarsening for the case of isotropic surface tensions.

3.3.5 Influence of external stress and potential healing

The first row of pictures in Fig. 3.10 shows aging at 125℃ with thermal mismatch and at a different angle of crystal lattices than before. This is then followed by application of *ca.* 5 MPa compressive stress in horizontal direction[2]. Intensification of the coarsening is clearly visible. If we now take the stress away and switch to room temperature (third row) we realize that healing sets in as a consequence to the diffusion process.
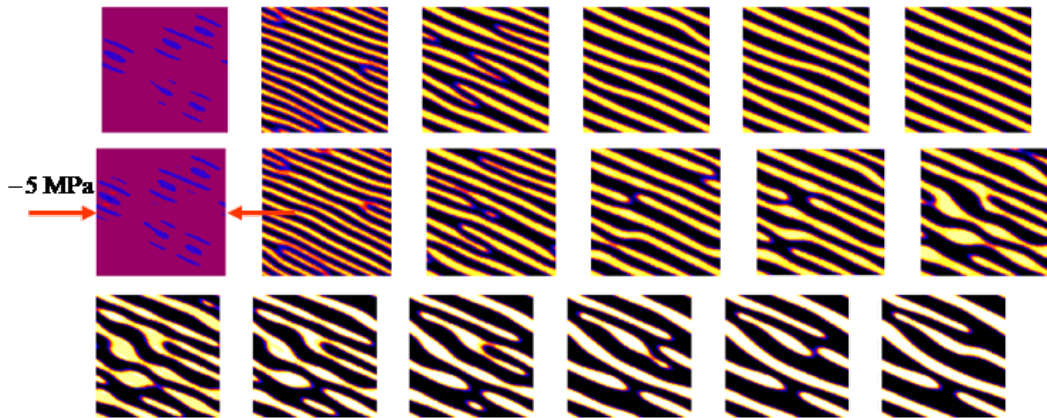

Figure 3.10: Aging at 125℃(top), application of a compressive external stress (middle), healing at low temperature (bottom).

---

[2]In fact a compressive strain ϵ_{11} was prescribed and the stress value followed by multiplying with Young's modulus of the alloy.

4 Growth of intermetallic compounds

4.1 Phenomenology

The term "intermetallic," a.k.a. an InterMetallic Compound (IMC), inter-metallic alloy, ordered intermetallic alloy, or long-range-ordered alloy, is a solid-state compound exhibiting metallic bonding, defined stoichiometry and ordered crystal structure. In context with the advent of lead-free low melting point microelectronic solders, IMCs have become more and more an object of interest and concern. As examples we consider the eutectic binary solder SnAg3.5 and the ternary eutectic SnAg3.8Cu0.7, which solidify at ca. 221℃ and 217℃, respectively, *i.e.* at a slightly higher temperature than eutectic SnPb. In contrast to the latter they show no spinodal decomposition, the mass percentage of the minority species is much too small and intermetallic compounds form instead in form of very small precipitates in a tin matrix.

Fig. 4.1 shows several scenarios of IMC formation. The first picture presents a solder ball made of SnAg3.8Cu0.7. Needles and platelets made of Ag_3Sn and Cu_6Sn_5 have formed within the tin matrix. The second picture shows what can happen at the interface of an SnAg3.5 solder ball attached to a copper pad: Again we see IMC needles consisting of Ag_3Sn. However, in addition to that a wawy, "scallop-shaped" interface of Cu_6Sn_5 has formed right at the interface where an ample supply of copper is present.
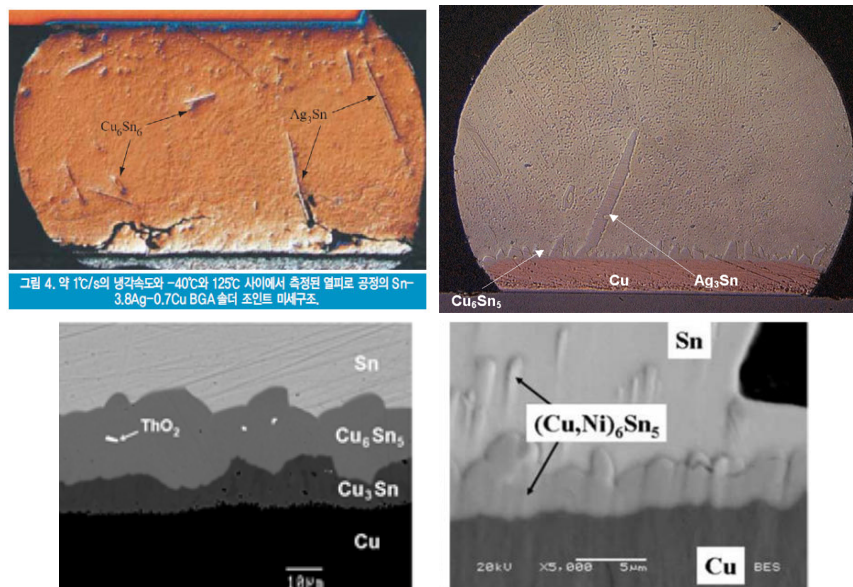

Figure 4.1: Formation of intermetallics in microlectronic solder connections, [82], [24], [66], [88].

The third micrograph shows what can happen if the SnAg3.5/Cu contact is aged at (elevated) temperatures: A second, less curvy intermetallic layer

made of Cu_3Sn has formed in between the copper substrate and the Cu_6Sn_5. Finally note that the copper substrate is usually passivated in order to avoid its oxidation. Frequently nickel is used for that purpose. This in turn can lead to the generation of "pure" nickel-tin IMCs, Ni_4Sn_3, or mixed compounds, such as $(Cu,Ni)_6Sn_5$ (last micrograph).

In summary we may conclude that were are facing a "combination" of the two effects presented in the last two sections. There are chemical reactions present, for example:

$$6Cu + 5Sn \rightleftharpoons Cu_6Sn_5. \tag{4.1.1}$$

Moreover, the lattice constants of the participating products and reactants are different, which will give rise to internal stress generation. Then, the atoms have to diffuse to the place where the reaction takes place. In fact, we are facing a multi-component diffusion process, since, for example, the diffusion coefficients of Sn in Cu and of Cu in Sn are very different, giving rise to the formation of vacancies. We proceed to discuss this issue.

4.2 Reliability issues

One of the main issues in context with the formation of IMCs in lead-free solders is their uncontrolled growth. For example, if Cu_6Sn_5 or Ag_3Sn platelets and needles form in the bulk of tin it might even be beneficial in the sense of particle toughening, as long as these structures do *not* become to large and pointy.

Moreover, if a microelectronic joint is "used," *i.e.*, an electric current goes through, this may increase the local temperature due to Joule heating. Besides that the electric current may trigger electromigrating effects.
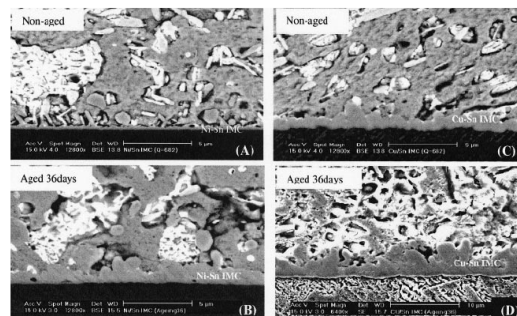

Figure 4.2: Thermally activated growth of Ni_4Sn_3 (left) and Cu_6Sn_5 (right) [93].

The effect of exposure to heat is shown in Fig. 4.2. The effect is clearly visible. Fig. 4.3 illustrates the process of deterioration for the case of electromigration.

A thin, uniform and continuous layer of intermetallic compounds is an important requirement for a high-quality contact, because it provides a metal-
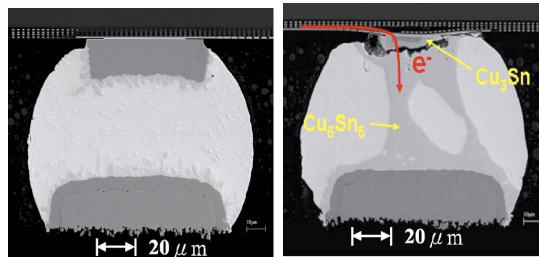
Figure 4.3: Cu_6Sn_5 growing by electromigration; left inset w/o electric current [14].

lurgical contact that is critical for electronic assemblies. At the same time, a thickly layered intermetallic layer reduces solder joint reliability because of its inherent brittleness and tendency to generate structural defects caused by the mismatch of physical properties.

In fact, large structural defects, such as interface cracks (see the right inset in Fig. 4.3), may be preceded by the formation of voids. Such voids can form in metals under suitable conditions of multiaxial stress. However, they can also result from different diffusion coefficients of the migrating species. The latter effect is known as *Kirkendall void formation.*

Early diffusion models postulated that atomic motion in substitutional alloys occurs via a direct exchange mechanism, in which atoms migrate by switching positions with atoms on adjacent lattice sites. Such a mechanism implies that the atomic fluxes of two different materials across an interface must be equal, as each atom moving across the interface causes another atom to move across in the other direction.

Another possible diffusion mechanism involves lattice vacancies. An atom can move into a vacant lattice site, effectively causing the atom and the vacancy to switch places. If large-scale diffusion takes place in a material, there will be a flux of atoms in one direction and a flux of vacancies in the other.

The Kirkendall effect arises when two distinct materials are placed next to each other and diffusion is allowed to take place between them. In general, the diffusion coefficients of the two materials in each other are not the same. This is only possible if diffusion occurs by a vacancy mechanism; with an exchange mechanism, atoms will cross the interface in pairs, so the diffusion rates will be identical. The material with the higher diffusion coefficient will have a larger associated vacancy flux into it, so the net movement of vacancies will be from the material with the lower diffusion coefficient into the material with the higher diffusion coefficient. For the present case (to be precise for 95Pb-5Sn) it is reported [85] that the diffusivity of Cu is about twice that of Sn at 170^0C, which confirms the experimental evidence in [66].

Fig. 4.5 illustrates, from an experimental materials science point-of-view [66], the currently accepted view of the various diffusion fluxes relevant for
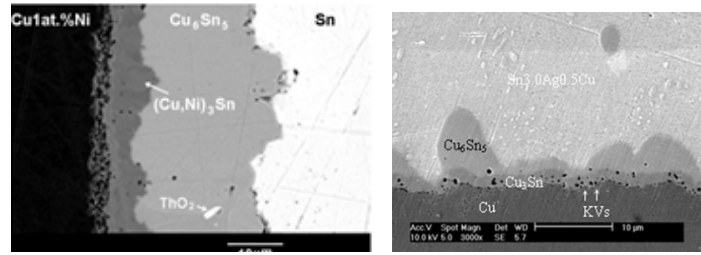
Figure 4.4: Kirkendall voiding at Cu/Sn interfaces [66], [99].

Cu_3Sn and Cu_6Sn_5 formation. Note that there is definitely more than one singular interface involved. The parameters p and q are the total amount of moles of Cu- and Sn-atoms, respectively, transferred per unit area through the product layer of Cu_3Sn during total diffusion time, t. Analogously, r and s are the number of moles of Cu- and Sn-atoms transported during interaction across unit area through the Cu_6Sn_5-phase layer. The transport of vacancies is not even shown but indirectly understood because of the different diffusion coefficients of the two species involved.

Moreover, note that experiments by Yu and Kim [100] that Kirkendall voiding in copper tin solder interconnects is strongly affected by mechanical stress. They say: "Once nucleated, voids can grow by local tensile stress, originating from residual stress in the film and/or the Kirkendall effect. Vacancy annihilation at the Cu/Cu_3Sn interface can induce tensile stress which drives the Kirkendall void growth."
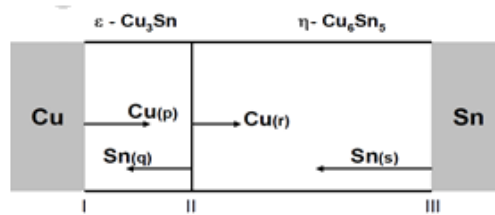

Figure 4.5: Elementary diffusion processes inherent to Cu_3Sn and Cu_6Sn_5 IMC formation from [66].

4.3   The modeling-state-of-the-art

During the last few years various attempts from the continuum theory perspective have been made to model IMC formation in microelectronic soldering. However, it should be mentioned that, for technological reasons, these efforts did not only include the modeling of the mechano-chemical part but also electromigrational effects based on diffusion theory in the bulk. Examples of this are the papers of [45], [1], [92], [15], [101] where we find expressions of an

extended diffusion flux, q, for the vacancies, such as:

$$\boldsymbol{q} = -D_{\mathrm{v}}C_{\mathrm{v0}}\left(\nabla c + \frac{Z^{*}e}{kT}(-\rho\boldsymbol{j})c + \frac{cf\Omega}{kT}\nabla\sigma_{\mathrm{spherical}} + \frac{c}{kT^{2}}Q^{*}\nabla T\right) \qquad (4.3.1)$$

where D_{v} is the effective vacancy diffusivity, C_{v0} is the equilibrium vacancy concentration in the absence of a stress field, c is normalized vacancy concentration, Z^{*} is the effective charge number of a vacancy, e is the electronic charge of an electron, k is Boltzmann's constant, T is absolute temperature, ρ is metal resistivity, $\boldsymbol{j}$ is the current density vector, f is the ratio of the volume of an atom to the volume of an atomic vacancy, Ω is the atomic volume, $\sigma_{\mathrm{spherical}}$ is the spherical part of stress tensor, and Q^{*} is the heat of transport.

In this context it must be noted that the interaction between mechanics and chemistry (and electric current) is more or less introduced as a *deus ex machina* than in a rational manner. However, it is fair to say that the aforementioned papers work with explicit field equations and provide valuable hints of how to treat them numerically. Their preferred method is finite elements, specifically ABAQUS, augmented by user-defined subroutines.

In the paper by Park and Arróyave [65] the multiphase-field formalism originally developed by Steinbach and Pezzolla [84] was used to model the development of both IMCs, Cu_3Sn and Cu_6Sn_5, within the framework of standard nucleation and multicomponent diffusion theory based on CALPHAD thermodynamic models and related data banks. The influence of coupling between diffusion, local mechanical stresses and strains, and the chemical reaction was not included. Moreover, since critical parameters for the simulation, such as interfacial energies and mobilities, are notoriously hard to come by, they were used as varying simulation parameters in order to gain insight into the dominant mechanisms controlling the evolution of the IMC layers. Moreover, only the early stages of aging were simulated.

As a true alternative to the standard multi-component diffusion equations Sadasiva *et al.* [79] have proposed to use phase field theories to tackle the problem. Their approach is based on such formulae as shown in Eqn. (4.3.1), where mechano-electro-chemical interaction is acknowledged, even in a somewhat empirical way. Loosely speaking, they also introduce a phase field function, ϕ, in order to smooth out the transition between regions of strong field fluctuations, just like one of the authors of this article did in [19] or [20].

Most recently Sadasiva *et al.* [80] have demonstrated that their custom-made code is currently capable of handling the migration of one species (Cu) and voids. Experimental verification of the results as well as detailed quantification is still pending.

In summary, we conclude that currently there is no truly multi-component diffusion theory available for describing IMC formation and growth in general, and of Ag_3Sn, Ni_3Sn_4, Cu_3Sn, Cu_6Sn_5, and $(Cu,Ni)_6Sn_5$ in particular, that connects mechanics, mass transport, and multi-component reactions. Moreover,

the chemical reaction process leading to these IMCs has not been addressed at all not to mention this being done in a thermodynamically proper manner. In particular, the use of modern concepts of chemical affinity written in terms of Eshelby's energy momentum tensor has not been realized. It is an open question as to whether a sharp interface theory might suffice or whether it has to be complemented or to be replaced by a phase field formulation. The future will tell.

References

[1]   C. Basaran and M. Lin. Damage mechanics of electromigration induced failure. *Mechanics of Materials*, 40(1):66–79, 2008.

[2]   T. Böhme and W. H. Müller. On the simulation of the spinodal decomposition process and phase growth in a leadfree brazing material. *Computational materials science*, 39(1):166–171, 2007.

[3]   T. Böhme, W. Dreyer, and W. H. Müller. Determination of stiffness and higher gradient coefficients by means of the embedded-atom method. *Continuum Mechanics and Thermodynamics*, 18(7–8):411–441, 2007.

[4]   T. Böhme, W. Dreyer, and W. H. Müller. Theoretical and experimental investigations of microstructural changes in lead-free solders. *Computational Materials Science*, 43(1):221–228, 2008.

[5]   T. Böhme, W. H. Müller, and K. Weinberg. Numerical modeling of diffusion induced phase transformations in mechanically stressed lead-free alloys. *Computational Materials Science*, 45(3):837–844, 2009.

[6]   A. Brandmair, T. Böhme, and W. H. Müller. Changes in the microstructure of materials and their impact on reliability: Experiments and modeling. *Microsystem Technologies*, 15(1):201–215, 2009.

[7]   C. M. Brown, W. Dreyer, and W. H. Müller. Discrete Fourier transforms and their application to stress-strain problems in composite mechanics: a convergence study. *Proceedings of the Royal Society of London A: Mathematical, Physical and Engineering Sciences*, 458(2024):1967–1987, 2002.

[8]   B. Budiansky and J. R. Rice. Conservation laws and energy-release rates. *Journal of applied mechanics*, 40(1):201–203, 1973.

[9]   G. Buratti, Y. Huo, and I. Müller. Eshelby tensor as a tensor of free enthalpy. In C.-S. Man and R. L. Fosdick, editors, *The Rational Spirit in Modern Continuum Mechanics*, pages 101–112. Kluwer Academic Publishers, 2004.

[10]   J. W. Cahn and J. E. Hilliard. Free energy of a non-uniform system. Part I: Interfacial free energy. *The Journal of Chemical Physics*, 28(1):258–267, 1958.

[11] C. Canuto, M. Y. Hussaini, A. Quateroni, and T. A. Zang. *Spectral methods in fluid dynamics, Springer Series in Computational Physics*. Springer, New York, Berlin, Heidelberg, 1988.

[12] Y. A. Çengel and A. J. Ghajar. *Heat and mass transfer: Fundamentals and applications*. McGraw-Hill, 2011.

[13] P. Cermelli and M. E. Gurtin. The dynamics of solid-solid phase transitions 2. Incoherent interfaces. *Archive for Rational Mechanics and Analysis*, 127(1): 41–99, 1994.

[14] B. Chao, S. H. Chae, X. Zhang, K. H. Lu, M. Ding, J. Im, and P. S. Ho. Electromigration enhanced intermetallic growth and void formation in Pb-free solder joints. *Journal of applied physics*, 100(8):084909, 2006.

[15] C. Chen, H. M. Tong, and K. N. Tu. Electromigration and thermomigration in Pb-free flip-chip solder joints. *Annual Review of Materials Research*, 40: 531–555, 2010.

[16] D. de Fontaine. Clustering effect in solid solutions. In N. Hannah, editor, *Treatise on Solid State Chemistry*, pages 129–178. Plenum Press, New York, London, 1975.

[17] B. E. Deal and A. S. Grove. General relationship for the thermal oxidation of silicon. *Journal of Applied Physics*, 36(12):3770–3778, 1965.

[18] D. B. Dingwell and S. L. Webb. Structural relaxation in silicate melts and non-newtonian melt rheology in geologic processes. *Physics and Chemistry of Minerals*, 16(5):508–516, 1989.

[19] W. Dreyer and W. H. Müller. A study of the coarsening in tin/lead solders. *International Journal of Solids and Structures*, 37:3841–3871, 2000.

[20] W. Dreyer and W. H. Müller. Modeling diffusional coarsening in eutectic tin/lead solders: a quantitative approach. *International Journal of Solids and Structures*, 38:1433–1458, 2001.

[21] W. Dreyer, W. Müller, and J. Olschewski. An approximate analytical 2D-solution for the stresses and strains in eigenstrained cubic materials. *Acta Mechanica*, 136(3–4):171–192, 1998.

[22] J. D. Eshelby. The force on an elastic singularity. *Philosophical Transactions of the Royal Society of London A: Mathematical, Physical and Engineering Sciences*, 244(877):87–112, 1951.

[23] J. D. Eshelby. The elastic energy-momentum tensor. *Journal of Elasticity*, 5 (3–4):321–335, 1975.

[24] D. R. Frear, J. W. Jang, Lin, J. K., and C. Zhang. Pb-free solders for flip-chip interconnects. *JOM*, 53(6):28–33, 2001.

[25] A. Freidin. Chemical affinity tensor and stress-assist chemical reactions front propagation in solids. In V. J. Kapoor and K. T. Hankins, editors, *ASME 2013 international mechanical engineering congress and exposition*, volume IMECE2013-64957, pages 1–10. American Society of Mechanical Engineers, 2013.

[26] A. B. Freidin. On the chemical affinity tensor for chemical reactions in deformable materials. *Mechanics of Solids*, 50(3):260–285, 2015.

[27] A. B. Freidin and E. N. Vilchevskaya. On kinetics of chemical reaction fronts in elastic solids. In H. Altenbach and N. F. Morozov, editors, *Surface Effects in Solid Mechanics*, pages 101–112. Kluwer Academic Publishers, 2014.

[28] A. B. Freidin, E. N. Vilchevskaya, and I. K. Korelev. Stress-assist chemical reactions front propagation in deformable solids. *International Journal of Engineering Science*, 83:57–75, 2014.

[29] Georgia Institute of Technology. *Silicon Dioxide.* http://www.ece.gatech.edu/research/labs/vc/theory/ oxide.html, 2015.

[30] P. Grigoreva. *Stress-assisted chemical reaction front propagation in deformable solids.* Bachelor thesis, Peter the Great St. Petersburg Politechnical University, 2015.

[31] M. E. Gurtin. The dynamics of solid-solid phase transitions 1. Coherent interfaces. *Archive for Rational Mechanics and Analysis*, 123(4):305–335, 1993.

[32] M. E. Gurtin. *Configurational forces as basic concepts of continuum physics.* Springer, New York, Berlin, Heidelberg, 2000.

[33] X.-L. Han, G. Larrieu, and C. Krzeminski. Modelling and engineering of stress based controlled oxidation effects for silicon nanostructure patterning. *Nanotechnology*, 24:1–14, 2013.

[34] P. Harris, K. Chaggar, and M. Whitmore. The effect of ageing on the microstructure of 60:40 tin-lead solders. *Soldering and Surface Mount Technology*, 7:20–23, 1991.

[35] P. Haupt. *Continuum mechanics and theory of materials.* Springer-Verlag, Berlin, Heidelberg, New York, 2002.

[36] K. Hawick. *Domain growth in alloys.* Ph.D. thesis, Edinburgh University, 1991.

[37] W. Heidug and F. K. Lehner. Thermodynamics of coherent phase transformations in nonhydrostatically stressed solids. *pure and applied geophysics*, 123(1): 91–98, 1985.

[38] C. Hollauer. *Modeling of thermal oxidation and stress effects.* Dissertation, Technische Universität Wien, 2007.

[39] C.-K. Huang, R. J. Jaccodine, and S. R. Butler. Stress effect on the oxidation of silicon. In V. J. Kapoor and K. T. Hankins, editors, *Silicon nitride and dioxide thin insulating films*, volume 87-10, pages 343–349. The Electrochemical Society, 1987.

[40] IUPAC. *IUPAC compendium of chemical terminology - the gold book.* http://goldbook.iupac.org/, 2015.

[41] D.-B. Kao, J. P. McVittie, W. D. Nix, and K. Sarawat. Two-dimensional thermal oxidation of silicon-i. experiments. *IEEE Transactions on Electron Devices*, ED-34(5):1008–1017, 1987.

[42] D.-B. Kao, J. P. McVittie, W. D. Nix, and K. Sarawat. Two-dimensional thermal oxidation of silicon-II. Modeling stress effects in wet oxides. *IEEE Transactions on Electron Devices*, ED-35(1):25–37, 1988.

[43] V. I. Levitas and H. Attariani. Anisotropic compositional expansion and chemical potential for amorphous lithiated silicon under stress tensor. *Scientific reports*, 3(1615):1–5, 2013.

[44] L. Li and W. H. Müller. Computer modeling of the coarsening process in tin–lead solders. *Computational materials science*, 21(2):159–184, 2001.

[45] M. Lin and C. Basaran. Electromigration induced stress analysis using fully coupled mechanical–diffusion equations with nonlinear material properties. *Computational Materials Science*, 34(1):82–98, 2005.

[46] M.-T. Lin. *Stress effects and oxidant diffusion in the planar oxidation.* Ph.D. thesis, Lehigh University, 1999.

[47] I.-S. Liu. On interface equilibrium and inclusion problems. *Continuum Mech. Thermodyn.*, 4:177–188, 1992.

[48] X. H. Liu, H. Zheng, L. Zhong, S. Huang, K. Karki, L. Q. Zhang, Y. Liu, A. Kushima, W. T. Liang, J. W. Wang, J.-H. Cho, E. Epstein, S. A. Dayeh, S. T. Picraux, T. Zhu, J. Li, O. J. P. Sullivan, J. Cumings, C. Wang, S. X. Mao, Z. Z. Ye, S. Zhang, and J. Y. Huang. Anisotropic swelling and fracture of silicon nanowires during lithiation. *Nano letters*, 11(8):3312–3318, 2011.

[49] R. B. Marcus and T. T. Sheng. The oxidation of shaped silicon surfaces. *J. Electrochemical Society*, 129(6):1278–1282, 1982.

[50] W. Merz and N. Strecker. The oxidation process of silicon: Modelling and mathematical treatment. *Mathematical Methods in the Applied Sciences*, 117: 1165–1191, 1994.

[51] P. J. Mohr, B. N. Taylor, and D. B. Newell. CODATA recommended values of the fundamental physical constants: 2006. *Reviews of Modern Physics*, 80: 633–729, 2008.

[52] H. Moulinec and P. Suquet. A fast numerical method for computing the linear and nonlinear mechanical properties of composites. *C. R. Acad. Sci. Paris*, 318(2):1417–1423, 1994.

[53] H. Moulinec and P. Suquet. A numerical method for computing the overall response of nonlinear composites with complex microstructure. *Comp. Meth. Appl. Mech. Engng.*, 157(1):69–94, 1997.

[54] MTData. *NPL Databank for Materials Thermochemistry.* National Physical Laboratory, Teddington, Middlesex, 1998.

[55] I. Müller. Eshelby tensor and phase equilibrium. *Theor. Appl. Mech.*, 25(1): 77–89, 1999.

[56] I. Müller and W. H. Müller. *Fundamentals of thermodynamics and applications with historical annotations and many citations from Avogadro to Zermelo.* Springer Verlag, Berlin, Heidelberg, 2009.

[57] W. H. Müller. Mathematical vs. experimental stress analysis of inhomogeneities in solids. *Journal de Physique IV. Colloque C1, suppleÂment au Journal de Physique III*, 6:C1–139–C1–148, 1996.

[58] W. H. Müller. Fourier transforms and their application to the formation of textures and changes of morphology in solids. *Proc. IUTAM Symp. on Transformation Problems in Composite and Active Materials, Cairo*, pages 61–72, 1998a.

[59] W. H. Müller. The possibilities of Fourier transforms for the calculation of damage evolution in metals. *ZAMM*, 78(52):5637–5640, 1998b.

[60] W. H. Müller. *An expedition to continuum theory.* Springer, Dordrecht, Heidelberg, New York, London, 2014.

[61] W. H. Müller and S. Neumann. An approximate analytical 3d-solution for the stresses and strains in eigenstrained cubic materials. *Int. J. Sol. Struct.*, 35 (22):2931–2958, 1998.

[62] T. Mura. *Micromechanics of Defects in Solids.* Martinus Nijhoff Dordrecht, The Netherlands, 2 edition, 1987.

[63] NIST. *Phase diagram AgCu.* http://www.metallurgy.nist.gov/phase/solder/agcu-w.jpg, 2015a.

[64] NIST. *Phase diagram SnPb.* http://www.metallurgy.nist.gov/phase/solder/pbsn-w.jpg, 2015b.

[65] M. S. Park and R. Arróyave. Concurrent nucleation, formation and growth of two intermetallic compounds (Cu_6Sn_5 and Cu_3Sn) during the early stages of lead-free soldering. *Acta Materialia*, 60(3):923–934, 2012.

[66] A. Paul. *The Kirkendall Effect in Solid State Diffusion.* Dissertation, Technische Universiteit Eindhoven, 2004.

[67] M. Pekař. Affinity and reaction rates: Reconsideration of theoretical background and modelling results. *Zeitschrift für Naturforschung A*, 4(5–6):289–299, 2009.

[68] I. Prigogine and R. Defay. *Chemical thermodynamics*. London: Longmans, Green, 1954.

[69] Process Specialties Inc. *Thermal oxide*. processspecialties.com, 2012.

[70] A. M. Pyzyna. *Thermal oxidation-induced strain in silicon nanobeams*. Dissertation, University of California Santa Barbara, 2005.

[71] A. M. Pyzyna, D. R. Clarke, and N. C. MacDonald. Fabrication and STEM/EELS measurements of nanometer-scale silicon tips and filaments. *Proc. Micro Electro Mechanical Systems, 2004, 17th IEEE International Conference on MEMS*, pages 189–192, 2004.

[72] V. S. Rao and T. J. R. Hughes. On modelling thermal oxidation of silicon I: Theory. *Int. J. Numer. Meth. Engng.*, 47:341–358, 2000.

[73] V. S. Rao, T. J. R. Hughes, and K. Garikipati. On modelling thermal oxidation of silicon II: Numerical aspects. *Int. J. Numer. Meth. Engng.*, 47:359–377, 2000.

[74] B. W. Reed. *STEM measurements and MEMS integration of nanometer-scale lateral silicon tips and filaments*. Dissertation, Cornell University, 2007.

[75] B. W. Reed, J. M. Chen, N. C. MacDonald, J. Silcox, and G. Bertsch. Fabrication and stem/eels measurements of nanometer-scale silicon tips and filaments. *Proc. Micro Electro Mechanical Systems, 2004, 17th IEEE International Conference on MEMS*, 60(8):5641–5652, 2004.

[76] O. Renner and J. Zemek. Density of amorphous silicon films. *Czechoslovak Journal of Physics*, 23(11):1273–1276, 1973.

[77] ResearchGate. *Why is the density of Si less than that of SiO2?* http://www.researchgate.net/post/ Why_is_the_density_of_Si_less_than_that _of_SiO2, 2015.

[78] J. R. Rice. A path independent integral and the approximate analysis of strain concentration by notches and cracks. *Journal of applied mechanics*, 35(2): 379–386, 1968.

[79] S. Sadasiva, G. Subbarayan, L. Jiang, and D. Pantuso. Numerical simulations of electromigration and stressmigration driven void evolution in solder interconnects. *Journal of Electronic Packaging*, 134(2):020907, 2012.

[80] S. Sadasiva, A. Udupa, G. Subbarayan, and B. Sammakia. Diffcode: A system for the simulation of diffusion driven phase evolution in solids. Research Triangle Park, NC, United States, 2015.

[81] V. Senez, D. Collard, B. Baccus, M. Brault, and J. Lebailly. Analysis and application of a viscoelastic model for silicon oxidation. *Journal of applied physics*, 76(6):3285–3296, 1994.

[82] SMT. *Pb-Free.* http://smtfocus.co.kr/Photo/1103sr2-4.jpg, 2015.

[83] J. K. Srivastava, M. Prasad, and J. B. Wagner. Electrical conductivity of silicon dioxide thermally grown on silicon. *Journal of The Electrochemical Society*, 132(4):955–963, 1985.

[84] I. Steinbach and F. Pezzolla. A generalized field method for multiphase transformations using interface fields. *Physica D: Nonlinear Phenomena*, 134 (4):385–393, 1999.

[85] A. J. Sunwoo, J. W. Morris, and G. K. Lucey. The growth of Cu-Sn intermetallics at a pretinned copper-solder interface. *Metallurgical Transactions A*, 23(4):1323–1332, 1992.

[86] P. Suquet. Une méthode simplifée pour le calcul de propriétés élastiques de matériaux hétérogènes á structure périodique. *C. R. Acad. Sci. Paris*, 311(2): 769–774, 1990.

[87] P. Sutardja and W. Oldham. Modeling of stress effects in silicon oxidation. *IEEE Transactions on Electron Devices*, 36(11):2415–2421, 1989.

[88] K. Sweatman, T. Nishimura, and K. McDonald, S. D. Nogita. Effect of cooling rate on the intermetallic layer in solder joints. In *IPC APEX Expo 2012: Proceedings*, 2012.

[89] Thermo-Calc. *Software TCFE7 Steels/Fe-alloys database version 7.* Thermo-Calc Software AB, Stockholm, 2015.

[90] L. M. Truskinovskii. Dynamics of non-equilibrium phase boundaries in a heat conducting non-linearly elastic medium. *Journal of Applied Mathematics and Mechanics*, 51(6):777–784, 1987.

[91] T. Tsakalakos. On certain phase transition related problems in metallurgy. pages 149–184, 1985.

[92] K. N. Tu, A. Huang, and F. Y. Ouvaug. Electromigration and thermomigration in flip chip solder joints. In *International Conference on Electronic Materials and Packaging*, pages 1–25. IEEE, 2006.

[93] P. L. Tu, Y. C. Chan, K. C. Hung, and J. K. L. Lai. Growth kinetics of intermetallic compounds in chip scale package solder joint. *Scripta materialia*, 44(2):317–323, 2001.

[94] Wikipedia. *Electrical resistivity and conductivity.* http://en.wikipedia.org/wiki/Electrical_resistivity_ and_conductivity, 2015a.

[95] Wikipedia. *LOCOS.* http://en.wikipedia.org/wiki/LOCOS, 2015b.

[96] Wikipedia. *Molar mass.* https://en.wikipedia.org/wiki/Molar_mass, 2015c.

[97] Wikipedia. *Silicon dioxide.* http://en.wikipedia.org/wiki/Silicon_dioxide, 2015d.

[98] Wikipedia. *Silicon.* http://en.wikipedia.org/wiki/Silicon, 2015e.

[99] C. Yu, Y. Yang, K. Wang, J. Xu, J. Chen, and H. Lu. Relation between Kirkendall voids and intermetallic compound layers in the SnAg/Cu solder joints. *Journal of Materials Science: Materials in Electronics*, 23(1):124–129, 2012.

[100] J. Yu and J. Y. Kim. Effects of residual S on Kirkendall void formation at Cu/Sn–3.5 Ag solder joints. *Acta Materialia*, 56(19):5514–5523, 2008.

[101] Y. Zhang. Electromigration failure prediction and reliability evaluation of solder bumps for FCBGA package. *Engineering Transactions*, 63(2):215–232, 2015.

Previous Issues

1. **W.-L. Schulze**. *Pseudo-differential Calculus and Applications to Non-smooth Configurations.* Volume 1, 2000, 136 p.

2. **S. Camiz.** *Exploratory 2- and 3-way Data Analisys and Applications.* Volume 2, 2001, 44 p.

3. **G. Jaiani**. *Theory of Cusped Euler-Bernoulli Beams and Kirchhoff-Love Plates*. Volume 3, 2002, 129 p.

4. **G. Jaiani, S. Kharibegashvili, D. Natroshvili, W.L. Wendland**. *Hierarchical Models for Cusped Plates and Beams.* Volume 4, 2003, 121 p.

5. **A. Bernardini, G. Bretti, P.E. Ricci.** *Laguerre-type Exponentials, Multidimensional Special Polynomials and Applications.* Volume 5, 2004, 28 p.

6. **Ts. Gabeskiria, G. Jaiani, J. Antidze, G. Datashvili.** *English-Georgian-Russian-German-French-Italian Glossary of Mathematical Terms.* Volume 6, 2005, 228 p.

7. **J. Rogava, M. Tsiklauri**. *High Order Accuracy Decomposition Schemes for Evolution Problem.* Volume 7, 2006, 164 p.

8. Volume 8, 2007 **was dedicated to the Centenary of Ilia Vekua.**

   It contains the following articles:

   - **R.P. Gilbert, G.V. Jaiani.** *Ilia Vekua's Centenary*
   - **H. Begehr, T. Vaitekhovich.** *Complex Partial Differential Equations in a Manner of I.N. Vekua.* pp. 15-26
   - **B.-W. Schulze.** *Operators on Configurations with Singular Geometry.* pp. 27-42
   - **V. Kokilashvili, V. Paatashvili.** *On the Riemann-Hilbert Problem in Weighted Classes of Cauchy Type Integrals with Density from $L^{P(\cdot)}(\Gamma)$.* pp. 43-52
   - **Tavkhelidze.** *Classification of a Wide Set of Geometric Figures.* pp. 53-61

9. **N. Chinchaladze**. *On Some Nonclassical Problems for Differential Equations and Their Applications to the Theory of Cusped Prismatic Shells*. Volume 9, 2008, 92 p.

10. **D. Caratelli, B. Germano, J. Gielis, M.X. He, P. Natalini, P.E. Ricci**. *Fourier Solution of the Dirichlet Problem for the Laplace and Helmholtz Equations in Starlike Domains*. Volume 10, 2009, 64 p.

11. **A. Cialdea.** *The L^P–Dissipativity of Partial Defferential Operators.* Volume 11, 2010, 94 p.

12. **D. Natroshvili.** *Mathematical Problems of Thermo-Electro-Magneto-Elasticity.* Volume 12, 2011, 128 p.

13. **G. Akhalaia, G. Giorgadze, V. Jikia, N. Kaldani, G. Makatsaria, N. Manjavidze.** *Elliptic Systems on Riemann Surface.* Volume 13, 2012, 155 p.

14. **I. Vekua.** *On Metaharmonic Functions.* Volume 14, 2013, 62 p.

15. **W. H. Müller, P. Lofink.** *The Movement of the Earth: Modelling the Flattening Parameter*. Volume 15, 2014, 42 p.

Information for the Authors

1. Papers written in English should be submitted as tex and PDF files via email to the managing editor

Dr. Natalia Chinchaladze
I.Vekua Institute of Applied Mathematics
of Tbilisi State University,
2, University st.
Tbilisi 0186
Georgia
e-mail: chinchaladze@gmail.com

2. Papers should be prepared in any standard version of TeX (i.e. plain, LaTeX, AMS-(La)Tex)

3. Letter's size and intervals between lines should be 12 pt, with a printed text area of 140mm x 225mm on a page.

4. Manuscripts should be compiled in the following order: title page; abstract; keywords; main text; acknowledgments; appendices (as appropriate); references; table(s) with caption(s) (on individual pages); figure caption(s) (as a list).

5. Abstracts of 100-150 words are required for all papers submitted.

6. Each paper should have 3-6 keywords. In addition to keywords, authors are encouraged to provide 2-6 AMS 2010 Mathematics Subject Classification codes.

7. Section headings should be concise and numbered sequentially, using a decimal system for subsections.

8. All the authors of a paper should include their full names, affiliations, postal addresses, telephone and fax numbers and email addresses on the cover page of the manuscript. One author should be identified as the Corresponding Author.

9. The decision on the acceptance is taken after a peer-reviewing procedure.

10. Authors submit their papers on the condition that they have not been published previously and are not under consideration for publication elsewhere.